DTU

Technical
University of
Denmark

Numerical Prediction of Green Water Loads on Ships

Kristian Bendix Nielsen
PhD thesis
June 2003

Department of
Mechanical
Engineering

MEK

Maritime
Engineering

Numerical Prediction of Green Water Loads on Ships

Kristian Bendix Nielsen

TECHNICAL UNIVERSITY OF DENMARK
DEPARTMENT OF MECHANICAL ENGINEERING
MARITIME ENGINEERING
JUNE 2003

Published in Denmark by
Technical University of Denmark

Maritime Engineering
Department of Mechanical Engineering
Technical University of Denmark
Studentertorvet, Building 101E, DK-2800 Kgs. Lyngby, Denmark
Phone +45 4525 1360, Telefax +45 4588 4325
E-mail: maritime.engineering@mek.dtu.dk
WWW: http://www.mek.dtu.dk/

Publication Reference Data
, K. B. Nielsen
Numerical Prediction of
Green Water Loads on Ships
PhD Thesis
Technical University of Denmark, Maritime Engineering.
June, 2003
ISBN 87-89502-76-0
Keywords: CFD, Numerical Simulation, Green Water, FPSO, Offshore

Preface

This thesis is submitted as a partial fulfillment of the requirements for the Danish PhD defence. The work was performed at the Section of Maritime Engineering (MT), Department of Mechanical Engineering (MEK), Technical University of Denmark (DTU), during the period of June 1999 to June 2003. The project was supervised by Associate Professor Stefan Mayer and Professor Jørgen Juncher Jensen whose help during the project is greatly appreciated.

The work was done as part of the Computational Hydrodynamics research frame program under the Danish Technical Research Council (STVF). Computing resources have been obtained partly due to the Danish Center for Scientific Computing, DCSC grant CPU-1101-20. The financial support is greatly acknowledged.

During my six months stay at the National Maritime Research Institute of Japan great hospitality was shown by all the staff. I would especially like to thank Dr. Takafumi Kawamura, Dr. Yoshiaki Kodama and Dr. Munehiko Hinatsu.

Finally, many thanks to colleagues at MT, friends and family for encouragement and support.

Kristian Bendix Nielsen

Lyngby, June 1, 2003

Executive Summary

The main objective of the present study has been to investigate problems related to shipping green water on deck of a floating vessel by use of numerical methods. A Navier-Stokes solver with a free surface capturing scheme, similar to the VOF method (Hirt and Nichols, 1981) has been applied.

The green water problem occurs when the relative free surface motion exceeds the freeboard of a floating vessel and the deck of the vessel is wetted. In the present context only FPSO type vessels, with zero forward velocity have been investigated. Apart from an introduction to the numerical method and simple tests of the free surface capturing scheme, the study can be devided into two parts: First, a number of simplified test cases have been investigated, which are all related to green water loads. These cases only include elements of the full green water problem and are primarily used as verification of the numerical model. These cases include dam break, cylinder impact, tank sloshing and wave crest impact on horizontal structures. Second, three test cases closely related to green water problems have been investigated. These include wave run-up on a wall, a green water problem with a fixed vessel and a full green water problem with relative ship motion included. Great effort has been made to validate and verify the numerical method and all computations have been verified by use of several computational grids with increasing resolution and validated by comparison to experimental data.

Results from the dam break and cylinder impact cases document that the numerical model accurately can predict complicated free surface problems and both water height and pressures/loads compares well with experimental data. The last stage of the dam break problem, where the water returns from impact with the wall on the opposite side of the tank is very sensitive to initial conditions, making this part of the problem difficult to reproduce exactly. This is also documented by comparison to results obtained by use of other numerical methods.

In addition to these cases, tank sloshing and wave crest impact on horizontal structures have been used for validation of more complicated free surface interaction problems. In the sloshing case both free surface contours and pressure time history of the water inside the tank shows good agreement with experimental data. Loads on horizontal rectangular beams exposed to wave crest impact are also well predicted numerically, as seen by comparison to experimental data.

Altogether the validation cases shows good agreement with experimental data and the model is considered to be applicable for many problems involving complex free surface flows and wave impact load modelling.

Modelling green water loads has been conducted on both a simplified setup and on a full green water problem. Visualisations of the free surface contours from a wave run-up and a simplified 2-D green water case showed good agreement with experimental measurements of the free surface. In the simplified 2-D green water case, where vessel motions were excluded, the numerical model was able to predict both water height on deck and pressure loads on a deck mounted structure very accurately, compared to experimental data. This investigation also visualised how a small plunging wave encounters the fore part of the FPSO deck and forms a small void cavity at the corner of the deck, in the initial stage of green water shipping. This flow behaviour was also reported in the experiments, which further validates the numerical method.

A full green water problem, including relative ship motion has been investigated in both 2-D and 3-D. In the computations, the relative ship motion has been included by adjusting the mean free surface level, coupled with the incoming wave, whereby the vertical motion at the bow of the FPSO is modelled. This model does not include rotational contribution from the pitch motion, but only includes the vertical component of the pitch motion at the bow of the FPSO. However, a comparison between computational and experimental water height on deck showed very favorable agreement. Furthermore, the numerical investigation showed that the 2-D and 3-D simulations gives almost identical results, illustrating that 3-D contributions to the deck flow are not so important in the very fore part of the deck. If the present method proves valid in general, this type of numerical simulation of green water loads can become an important tool in design for an effective bow shape to reduce green water loads.

Synopsis

Hovedformålet med dette studium har været at undersøge problemer relateret til dæksoverskylninger ved brug af numeriske metoder. En Navier-Stokes løser, med en VOF metode (Hirt and Nichols, 1981) til bestemmelse af den frie overflade, er blevet anvendt.

Dæksoverskylninger forekommer når bølgeelevationen af vandoverfladen overstiger fribordet på et flydende fartøj. I dette studium bliver der kun betragtet dæksoverskyldinger på forankrede FPSO fartøjer. Ud over en introduktion til de numeriske metoder og simple tests af forskellige fri overflade algoritmer, kan dette studium inddeles i to afsnit: Først er et antal simple testeksempler blevet undersøgt, som alle er relateret til grønt vand på dæk. Disse eksempler inkludere dæmnings brud, cylinder kollision, tank sloshing (voldsomme væskebevægelser) og bølgetop kollision med horisontelle strukturer. Dernæst er tre eksempler blevet undersøgt som alle er tæt forbundet med dæksoverskyldninger. Disse inkludere bølgeoverskylning af en fastholdt struktur (væg), simplificeret dæksoverskyldning med fastholdt skib og en fuld dæksoverskyldning, inklusiv relativ skibsbevægelse. Studiet har fokuseret meget på verifikation og validering af den numeriske model, alle beregninger er blevet verificeret med brug af adskillige beregningsnet med forskellig opløsning og resultaterne er blevet valideret med eksperimentelle resultater.

Resultaterne fra dæmningsbrud og cylinder kollision med vand dokumenterer at den numeriske model er i stand til nøjagtigt at beregne komplicerede frie overflade strømninger og både vandhøjde og tryk/belastninger stemmer godt overens med eksperimentelle resultater. Den sidste del af dæmnings bruddet, hvor vandet returnerer efter kollision med den modstående væg er meget følsom overfor begyndelsesbetingelser, hvilket gør denne del vanskelig at reproducere nøjagtigt. Dette er også dokumenteret ved sammenligning med andre numeriske metoder.

Ud over disse eksempler er tank sloshing og bølgetop kollision med horisontale strukturer blevet anvendt til validering af mere komplicerede fri overflade problemer. I tank sloshing analysen viser både visualiseringer af den frie overflade samt tryk tidsserier god overensstemmelse mellem numeriske og eksperimentelle resultater. I analysen af bølgetop kollision med horisontelle rektangulære bjælker er der også god overensstemmelse mellen beregnede belastninger og eksperimentelle resultater.

Alt i alt viser validerings eksemplerne god overenstemmelse mellem numeriske resultater og eksperimenter, og konklusionen er at modellen er anvendelig og valideret indenfor mange

strømningsproblemer der involverer komplekse strømninger med fri overflade og bølge belastninger på strukturer.

Modellering af dæksoverskylninger er blevet udført både på en simplificeret opsætning uden skibsbevægelser og på et fuldt dæksoverskylnings problem. Visualiseringer af beregnede frie overflade konturer fra bølgeoverskylning af en fastholdt struktur og af en simplificeret 2-D dæksoverskylning viste god overensstemmelse med eksperimentelle resultater. I den simplificerede 2-D dæksoverskylning, hvor skibsbevægelser var ekskluderet, var den numeriske model istand til at beregne både vandhøjde på dæk og trykbelastning på en dæksstruktur meget nøjagtigt, sammenlignet med med eksperimentelle resultater. Denne analyse viste også at et lille tomrum bliver dannet ved det forreste hjørne af dækket i den indledende del af dæksoverskylningen. Dette blev også rapporteret i forbindelse med eksperimenterne, hvilket yderligere validerer de numeriske beregninger.

Et fuldt dæksoverskylnings problem, hvor den relative skibsbevægelse er inkluderet, er blevet undersøgt i både 2-D og 3-D. I beregningerne er den relative bevægelse blevet inkluderet ved at justere den frie overflade, hvorved den relative bevægelse ved forskibet på FPSOen er blevet modelleret. Denne model inkludere ikke det rotative bidrag fra duvning men kun den vertikale komposant af duvningsbevægelsen ved forskibet at FPSOen. Sammenligningerne mellem beregnede og eksperimentelle vandhøjder på dæk viser alligevel god overensstemmelse på trods af denne simplifikation. Sammenligninger af beregnede 2-D og 3-D resultater viser at disse næsten er identiske, hvilket illustrerer at strømningen på den forreste del af dækket ikke er domineret af 3-D bidrag. Hvis den aktuelle metode til bestemmelse af dæksoverskylninger viser sig at være anvendelig generelt kan den blive et vigtigt værktøj til design af effektive bovformer til reduktion af dæksoverskylninger.

Contents

Symbols

The symbols used in this thesis are generally explained when they are first introduced. The following list contains the main symbols used.

Roman Symbols

A_{hyd}	Sectional hydrodynamic damping
$\boldsymbol{A}$	Discretised face normal
B	Breadth of vessel
C_D	Cell CFL number
D	Draught of vessel
E	Free surface extrapolation operator
F_T	Forcing function
$\boldsymbol{G}$	Discretised gradient operator
G_T	Forcing function
H	Wave height
I	Discretised linear interpolation operator
L	Length
Q	QUICK operator
R	Radius
Re	Reynolds number
S	Level of submergence
T	Wave period
T_{res}	Resonance period
U	Characteristic velocity
V_c	Cell volume
a	Wave amplitude
c_g	Group velocity
f	Transfer function variable
g	Gravitational acceleration
h	Mean water level

i, j	Cell indices
k	Wave number
l	Face leg
$\boldsymbol{n}$	Cell normal vector
$\boldsymbol{n}_{fs}$	Cell normal vector at free surface
p	Pressure
$\tilde{p}$	Static pressure
t	Time
$\boldsymbol{u}$	Velocity vector
w	Heave motion
$x_{1,2,3}$	Cartesian coordinates
z_s	Vertical ship motion

Greek symbols

α	Cell filling degree
$\tilde{\alpha}$	Normalised α
β	Inundation of beam element
Γ	Cell boundary
γ_f	Switching function
ζ	Wave elevation
η	Transfer function variable
θ	Pitch angle
θ_f	Angle between cell face and free surface
κ	Smith correction factor
λ	Wave length
ν	Kinematic viscosity
ξ	Phase
ρ	Mass density of water
σ	Stress
Φ_w	Transfer function heave
Φ_θ	Transfer function pitch
φ	Gerenic variable
Ω	Cell volume
∇	Gradient operator

Abbreviations

BEM	Boundary Element Method
BC	Boundary Condition
CBC	Convective Boundedness Criteria
CFD	Computational Fluid Dynamics
CFL	Courant-Friederich-Lewy
CICSAM	Compressive Interface Capturing Scheme for Arbitrary Meshes
HRIC	High Resolution Interface Capturing
LSM	Level Set Method
MAC	Marker and Cell
NVD	Normalized Variable Diagram
SPH	Smooth Partical Hydrodynamics
UQ	UltimateQuickest
VOF	Volume of Fluid

Chapter 1

Introduction to Green Water Problems

The green water problem has been known in the maritime world for a long time. The problem arises when a ship, usually in harsh weather conditions, encounters waves that exceed the freeboard and wet the deck. The term 'green water' refers to the shipped water not only consisting of spray from wave crests encountering the ship's bow or side, but it also means a solid bulk of sea water (which is usually more green than blue), exceeding the freeboard and running over the forecastle or side of the ship. In Fig. 1.1 a photo from offshore Newfoundland illustrates a green water incident on a small supply vessel where the forecastle is clearly covered with a solid bulk of water. In most green water incidents the

Figure 1.1: *Example of green water load on a small vessel.*

shipped water will not have any detrimental effect and run off the deck once the shipdeck exceeds the wave crest. However, in some cases the amount of shipped water can be so large

that it causes damage to deck equipment, plating, structures or cargo being transported on the deck. For normal merchant vessels, green water incidents are avoided by imposing operation restrictions, such as minimising the operation speed or altering the course, as reported by Tan (1969), and by having passive protection on deck, such as breakwaters or other protective structures.

With the introduction of floating production storage and offloading units (FPSO's) and Floating Storage Units (FSU's) in the offshore industry, the problem of green water loads has been given increasing attention. And the effort to install FPSO's in yet harsher environments have increased the problems related to green water incidents, e.g. Ersdal and Kvitrud (2000). The FPSO vessels are normally new- or rebuilt tankers, which are moored to an offshore location and remain in the same location for a period of up to 7-8 years. The vessels are equipped with sensitive production and piping equipment on deck, and damage to this equipment, as a result from green water loads, can be very costly in repairs and downtime of the unit. Some of these vessels are equipped with a turret, which allows for weather-vaning. The placement of the turret at the bow requires that sensitive production equipment is also placed at the bow, which increases the risk of damage.

In this chapter the physics of the green water incidents will be introduced, and the major contributing factors will be analysed. Previous and current studies in the field of green water loads will be presented, and the scope of the present thesis will be outlined.

1.1 Physics of Green Water Loads

The chain of events leading to shipping water and green water loads has been investigated for many years. The amount of shipped water is an important parameter, but the dynamics of this water is equally important, as well as the loads imposed by the water on deck and deck structures. Many factors play a role in the occurrence and severity of the green water incidents, and the list includes

- Relative wave motion
- Freeboard height
- Ship motion and forward speed
- Ship's flare

Some items are closely linked to others, but will here be treated separately to give an overview of the physics behind green water loading

1.1.1 Relative Wave Motion and Freeboard Height

The basic parameter to be determined in green water cases is the relative wave motion. In linear analysis, the water height on deck that causes the load can be found from the relative wave motion:

$$r_{wave}(t) = \zeta(t) - z(t) \tag{1.1}$$

where $\zeta(t)$ is the incident wave elevation and $z(t)$ is the vertical ship motion. These are defined as

$$\zeta(t) = \frac{H}{2}\cos(\omega t - kx) \tag{1.2}$$

$$z(t) = A_z \cos(\omega t + \xi) \tag{1.3}$$

where ω is the wave frequency, k is the wave number, A_z is the vertical ship motion amplitude (heave and pitch), and ξ is the vertical ship motion phase angle.

In linear analysis, any exceeding of the freeboard height by the relative wave height (Eq. (1.1)) will lead to an equivalent amount of water on deck. This estimation is the basis of the green water prediction methods by Ochi (1964) and Fukuda *et al.* (1973). However, as shown experimentally by both Buchner (1995a) and Ogawa *et al.* (1998), exceeding the freeboard do not necessarily lead to an identical water height on deck.

1.1.2 Ship Motion and Forward Speed

Although ship motion and forward speed are included in the computation of relative motion, the effects of motion and forward speed have additional influence on the green water incidents. This is through dynamic amplification of the load that the shipped water imposes on the deck structure. Ochi (1964) states that the pressure on the deck associated with a green water incident corresponds to the static water pressure of the water on deck, while experiments by Buchner (1994) show that for a frigate, with a large forward speed, a very significant dynamic amplification may occur where the pressure measured at the deck exceeds the static water pressure by a factor of 15. This proves that in some cases the dynamic amplification may be almost neglected, while in others the dynamic amplification may significantly increase the deck pressure load.

1.1.3 Ship's Flare

The presence of flare in the bow region of the ship affects both the relative motion and the diffraction of the incoming wave. This influences the resulting water height on deck and the dynamics of the shipped water on the deck. Most methods for determining the relative motions are based on linear diffraction analysis, where exciting forces on the ship due to the (undisturbed) waves and the reflected (diffracted) waves are determined. This method only takes into account the ship's geometry up to the still water line, and the geometry above the still water line is not included. It also neglects the effect of dynamic swell, which is the increase of the water level near the ship as a result of the presence of the hull in the wave. Buchner (1995a) and Buchner (1996) also showed experimentally that for a moored FPSO, a change in the bow geometry when more flare is added to the bow above the still water line may increase the relative motion.

Regarding the resulting water height on deck, Buchner and Voogt (2000) showed, also for a moored FPSO, that an approximate linear relation exists between the relative exceeding of the freeboard and the resulting water height on deck and that the factor between them depends on the flare of the ship's bow. The experiments clearly showed that the actual water height on deck, resulting from the relative exceeding of the freeboard, is significantly reduced with increasing bow flare.

In a previous work O'Dea and Walden (1984) investigated the effect of flare on green water loads, by applying significant flare to traditional ship types, and the conclusion was that the deck wetness was reduced as a result of the increased flare. In another study by Lloyd *et al.* (1985), the effect of flare was also investigated by applying different bow configurations to a frigate type ship, and they concluded that a heavily flared bow increases the deck wetness. Though these two conclusions contradict each other, they may still both be true. Since it is known that flaring of the bow will alter the response of the ship for a given wave, this can in some cases where the ship motion at the bow comes out of phase with the relative motion, decrease the relative motion and thus reduce the amount of shipped water, whereas in other cases, the increased relative motion will increase the relative wave at the bow and thus increase the amount of shipped water.

To illustrate the disagreement in the maritime community regarding the effect of bow flare on deck wetness Lloyd *et al.* (1985) give a list of previous works, and it is clear that there are many different opinions on this topic, which illustrates the complexity.

1.2 Prediction Methods for Green Water Loads

A number of methods for predicting green water loads have been proposed. This section gives an overview of the methods. For further literature, Buchner (2002) and Greco (2001) give good introductions to the field.

For ordinary ships Ochi (1964) made a probability analysis, estimating the probability of deck wetness from the freeboard height and the variance of the relative wave motion between wave and ship's bow. The method gives a probability distribution for the pressure on deck, based on the assumption that the pressure on deck corresponds to the static water pressure of the shipped water.

Hamoudi and Varyani (1998) presented extensive experimental studies to determine probability levels of deck wetness, for various Froude numbers and wave heights. The number of incidents was recorded and compared to previous experimental work. The study showed number of occurrences and loads on a structure placed in the bow region. The experiments used the S175 container ship model.

Mizoguchi (1989) presented a method for evaluating the water height and the pressure on deck, based on a combination of experiments and numerical simulation. The water height of the shipping green water is measured experimentally and used as input for a numerical simulation of the water flow on the deck. It is assumed that the dynamics of the ship, once the water has entered the deck area, does not affect the following flow, and the flow on deck is described by shallow water theory, where the water has a constant velocity over the depth. The method shows some similarities between computed water heights on deck and experimentally measured results. The method employs an empirical relation between the initial water height and the initial pressure, which is needed as an initial condition for the numerical model.

Using a combination of experimental results and empirical methods, Ogawa *et al.* (1998) presented a method for evaluating the water heights on deck, the pressure on deck and the pressure on structures located on the deck. The experiments were used to evaluate the relative wave height in front of the ship, and a model for determining flood waves, which were corrected to include the bow geometry and the pitch angle, was employed to determine the water height on deck. Pressures on deck were estimated by a method presented by Buchner (1995b) and load on deck structures by a Wagner based method.

By application of a boundary element method Maruo and Song (1994) made numerical simulations of ship-wave interaction in the bow region and early stage green water shipping. The method was designed for highspeed vessels and investigated the effect of the wave steepness (ratio of wave height to wavelength) on the water shipping. The numerical model was two-dimensional, and the variation along the ship's hull was obtained by applying the model to various cross sections.

Wan and Wu (1999) used a Navier-Stokes solver, with an artificial compressibility scheme, combined with a volume-of-fluid (VOF) method (Hirt and Nichols, 1981) for free surface capturing, to model a green water incident. The scheme is simplified to 2-D modelling, and the (relative) motion of the vessel is not modelled. A single wave is set up in the computational domain, and the resulting water height and pressure on deck are registered. No comparison with experimental results is presented.

Also in the category of Navier-Stokes solvers Fekken *et al.* (1999) presented a method for simulating green water incidents where the free surface modelling was based on a VOF type approach. The interaction between ship and incoming wave was not modelled but instead a dam break type flow, where the ship motion was neglected, was used to model the water flow on deck. Thus a water front with zero initial velocity was set up in front of the ship's bow where the flow could freely flow onto the deck. The paper presented comparisons to experiments and concluded that overall physical behaviour of the flow could be predicted, but that the lack of modelling ship-wave interaction and ship motion limited the applicability of the method.

In the most extensive experimental work conducted in the field of green water loads, Buchner (2002) presented experimental investigations of nonlinear relative wave motion, the physics of water flow onto deck and impact loading on structures located on deck. The work was aimed at FPSO's, using moored vessels with tankerlike structures. For the relative motion, Buchner (2002) documented the importance of including the above waterline bow geometry in the response of the ship. For the water flow on deck, the effect of bow geometry and flare was investigated analysing the flow pattern on deck for different bow types and flare angles. The resulting pressure on deck was also investigated, where the different static and dynamic effects for deck pressure were isolated and evaluated. Finally, the investigation included the impact pressure on various deck structures. Numerical simulation of green water loads was also presented, based on a method presented in Fekken *et al.* (1999).

Greco (2001) also conducted both experimental and numerical investigations of green water loads on an FPSO. The experiments included both early stage green water impact, using wave run-up on a solid wall, and the following impact on a structure. The whole study was two-dimensional (in the $x - z$ plane) and the dynamic effects from the relative ship-wave motion were neglected. For the numerical simulation, a fully nonlinear boundary element method was applied and the results were compared to experimental data.

In Stansberg and Karlsen (2001) an experimental study of green water loads on FPSO's was presented, measuring relative wave motion, water level on deck and impact pressures. These results were in Hellan *et al.* (2001) compared to numerical simulations, where a 3-D linear diffraction program was used to analyse the relative wave motion and a dam break model was used to predict the water flow on deck. The comparison showed some resemblance between numerical and experimental results. It was concluded that further investigation was needed to describe the ship-wave interaction and the green water dynamics.

1.3 The Present Work

In this thesis a numerical model with extensive free surface capabilities will be applied to a number of problems related to green water loads. The model, which is a Navier-Stokes solver with a free surface capturing scheme implemented to model the free surface, has been extended by a number of transport schemes. In the first part of the study, the numerical

model is described and the free surface schemes are evaluated. In the second part, the Navier-Stokes solver is applied to a number of problems including

- Dam break flow
- Wave impact on cylinder
- Tank sloshing
- Wave loads on horizontal profiles
- Simplified 2-D run-up and green water shipping
- 3-D green water load on an FPSO

All cases are compared to relevant experimental data for validation. The applicability of the current numerical methods to problems related to green water loads will be discussed and evaluated.

The general strategy which is used for the numerical simulations consists of three steps. First, the numerical problems are investigated with several computational grids in order to investigate the convergence properties of the numerical problems. The obtained results are discussed and evaluated. Second, since all problems involve free surface flows, visualisations of the free surface contours are used to investigate the flow properties in order to understand the flow physics pertaining to the problem. To the extent it is possible, the visualisations will be compared to available experimental visualisations. Third and last, the main flow quantities, such as the resulting wave height or water level will be compared to experimental values. This step is the final validation of the computed results, which should help to document the applicability of the numerical method to the present problem. From this it will be possible to comment on the future perspective of the applied model and give guidelines to future research.

1.3.1 Outline of the Thesis

Apart from the present introduction, the thesis have two main sections, the first is a description of the currently used numerical model, and in the second part the previously mentioned model problems will be investigated. The overview of the chapters is as follows:

In the first part of the thesis, two chapters describe the applied numerical model. Chapter 2 contains a description of the governing mass and momentum conservation equations. The general solution procedure is presented, along with a description of the applied spatial and time discretisation. In Chapter 3 the free surface modelling scheme is delt with, in this case the volume-of-fluid (VOF) method. Various VOF transport schemes are implemented in the

numerical model, and a specially constructed test evaluates the performance of the different schemes.

The following chapters are all concerned with the investigated problems, which are in some way related to green water loads. In Chapter 4 two problems are presented. First the dam break problem is investigated, where one side of an initially retained container of water is removed, allowing the water to flow into an empty region, and second a cylinder impact with water at rest is investigated. Chapter 5 contains a description of the sloshing problem with partially filled tanks. Both the free surface contours and the time histories of the pressure measured inside the tank will be compared between computations and physical experiments. Wave-in-deck problems where a wave crest encounters horizontal plate structures are investigated in Chapter 6. This problem is part of a push-over analysis of offshore platforms and is not directly related to green water loads. However, the ability of the numerical model to predict impact loads is an important aspect in green water analysis, so in this way the problems are related. The first actual green water investigation is presented in Chapter 7. First a wave run-up problem, which can be seen as an initial stage of the green water problem, is presented. Next, a simplified green water incident with a steady 2-D FPSOlike structure is investigated. In this investigation the visualised free surface contours, the resulting water height on deck, and the resulting pressure of an impact with a deck mounted structure are compared between computations and experiments. The final green water investigation is carried out in Chapter 8 where a full green water investigation is conducted. This means the inclusion of relative ship motions as well as 3-D investigation of green water on an FPSO. The numerical problem is restricted to only including vertical translating motion of the FPSO, thus neglecting the influence of rotation. In Chapter 9 some general remarks on the present study will be made, along with suggestions for further investigation.

Chapter 2

Governing Equations and Solution Procedure

For modelling the different fluid flow problems in this thesis, a robust and versatile Navier-Stokes solver with the ability to model complex free surface flows is required. Although many commercial codes, such as COMET, Fluent and STAR-CD, are available for solving the Navier-Stokes equations, and also offer various schemes for modelling free surface flows, the in-house NS3 code has been modified and applied to fluid flow modelling in the problems regarded in the present context. Although it is not as mature as some of the commercial codes, the NS3 code offers a lot of flexibility, since the availability of the source code and the close contact with the main developers offer a freedom in choice of scheme and the possibility of investigating the efficiency of new models.

The NS3 code was originally developed at the International Research Center for Computational Hydrodynamics (ICCH Hørsholm, Denmark), and different versions of it have previously been presented by Mayer *et al.* (1998), Sørensen *et al.* (1997) and Kawamura (1998). In this chapter the governing equations and the solution procedure will be briefly presented.

2.1 Mathematical Model

The modelling of fluid flow can be described by conservation principles, i.e. mass and momentum conservation. In the following only incompressible Newtonian fluids are used, since these are sufficient for the type of engineering applications considered here. Incompressibility implies that the density of the fluid is not dependent on the pressure, and for this type of fluid, the mass and momentum conservation can, in integral form, be written as

$$\oint_{\Gamma} \boldsymbol{u} \cdot \boldsymbol{n} \, d\Gamma = 0 \tag{2.1}$$

and

$$\frac{\partial}{\partial t}\int_{\Omega} \boldsymbol{u}\, d\Omega = -\oint_{\Gamma} (\boldsymbol{u}\otimes\boldsymbol{u})\cdot\boldsymbol{n}\, d\Gamma - \oint_{\Gamma} p\boldsymbol{n}\, d\Gamma + \frac{1}{Re}\oint_{\Gamma} \nabla\boldsymbol{u}\cdot\boldsymbol{n}\, d\Gamma, \tag{2.2}$$

where $\boldsymbol{n}$ is the outward pointing normal vector at the boundary Γ of a volume element Ω, t is time, Re is the Reynolds number, $\boldsymbol{u}$ is the Cartesian velocity vector, and $\otimes$ is the outer vector product operator. The Reynolds number Re is defined as

$$Re = \frac{UL}{\nu} \tag{2.3}$$

with U and L as characteristic velocity and length parameters, and ν is the kinematic viscosity. The pressure variable p is defined as the deviation from hydrostatic pressure given by

$$p = \tilde{p} + gx_3, \tag{2.4}$$

where $\tilde{p}$ is static pressure, g is gravitational acceleration and x_3 is the Cartesian coordinate in the direction of gravitation.

Eqs. (2.2) - (2.1) are given for an Eulerian grid (e.g. fixed in time) but can be extended to arbitrary Eulerian-Lagrangian by including grid velocity in the convective term, which is the first on the right hand side of Eq. (2.2). Various turbulence models have also been implemented in the code, but since turbulent effects are considered negligible for the applications regarded in this thesis, turbulence modelling is omitted.

2.1.1 Boundary Conditions

In order to render a unique solution of the conservation equations, the problem requires information about the solution at the domain boundaries. Generally, two types of boundary condition are applied: Dirichlet and Neumann type condition. The Dirichlet condition states that

$$\varphi_b = r \tag{2.5}$$

and the Neumann condition that

$$\frac{\partial\varphi_b}{\partial\boldsymbol{n}} = r, \tag{2.6}$$

where φ_b is the value at the boundary for the variable φ and r is a constant. For pressure and velocity, the boundary conditions for the different types of outer boundary are given in Table 2.1.

Table 2.1: *General boundary conditions for pressure and velocity*

	p_b	$\boldsymbol{u}_b$
inflow ($x_1 = \ inflow$)	$\frac{\partial p_b}{\partial n} = 0$	$\boldsymbol{u}_{i,b} = \{u_{\text{inflow}}, 0\}$
outflow	$p_b = 0$	$\frac{\partial u_{i,b}}{\partial n} = 0$
body surface	$\frac{\partial p_b}{\partial n} = 0$	$u_{i,b} = 0$
symmetry plane ($x_1 = \ symm$)	$\frac{\partial p_b}{\partial n} = 0$	$\frac{\partial u_{i,1}}{\partial n} = 0$, $u_{i,2} = 0$
free surface (see Section 2.3)	$\tilde{p}_b = 0$	$\frac{\partial \boldsymbol{u}}{\partial n_{fs}} = 0$

2.2 Spatial Discretisation

To solve the governing equations a domain is introduced in which the equations are solved. This domain can be divided into a number of blocks forming a multiblock domain but, for simplicity, the discretisation procedure will here be derived for a single block. The discretisation scheme and the solution routine follow Zang *et al.* (1994).

When the classic finite volume method is applied, the domain is discretised by subdivision into smaller non-overlapping control volumes Ω_c, also denoted cells. The whole domain containing all cells is termed the grid or the computational grid. Cartesianbased structured grids are used in the present method, containing quadrilateral and hexahedral cells for two and three dimensions respectively. A cell-centered variable arrangement is used for the discretisation scheme, and the governing equations are solved by use of the primitive variables of pressure and velocity.

For a cell Ω_c with the cell boundary Γ_c the surface integrals can be discretised as a sum over the cell faces Γ_f, and in discrete form the governing equations (Eqs. (2.1) - (2.2)) can be rewritten as

$$\sum_f \oint_{\Gamma_f} \boldsymbol{u} \cdot \boldsymbol{n} \, d\Gamma = 0 \tag{2.7}$$

and

$$\frac{\partial}{\partial t} \int_{\Omega_c} \boldsymbol{u} \, d\Omega = -\sum_f \oint_{\Gamma_f} (\boldsymbol{u} \otimes \boldsymbol{u}) \cdot \boldsymbol{n} \, d\Gamma - \sum_f \oint_{\Gamma_f} p\boldsymbol{n} \, d\Gamma + \frac{1}{Re} \sum_f \oint_{\Gamma_f} \nabla \boldsymbol{u} \cdot \boldsymbol{n} \, d\Gamma, \tag{2.8}$$

where $\sum_f \Gamma_f = \Gamma_c$ and $\sum_c \Omega_c = \Omega_c$. A collocated arrangement is used where the dependent variables of velocity and pressure are located at cell centres. Fig. 2.1 illustrates the curvilinear discretised domain for a two-dimensional case. The cell faces $east, west, south$ and $north$ will in the following be denoted e, w, s and n.

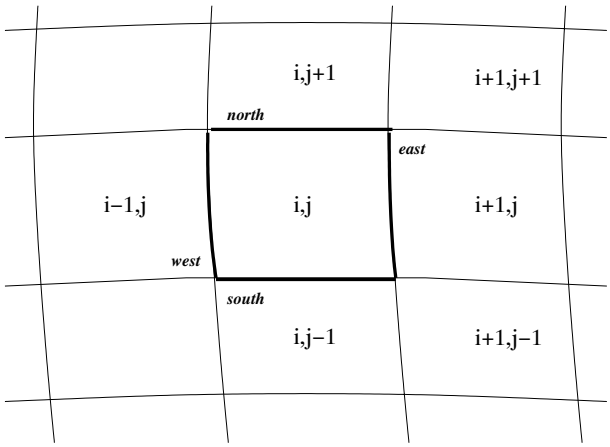

Figure 2.1: *Cell layout for 2D structured grid. Cell Ω_c shown in bold.*

The integrals over control volumes and surfaces for the various terms in Eqs. (2.7) - (2.8) are evaluated in the following using single-point quadrature.

Divergence Term

The mass equation (Eq. (2.7)) states that the velocity field must be divergence free, and the face integral can be reduced as

$$\sum_f \oint_{\Gamma_f} \boldsymbol{u} \cdot \boldsymbol{n} \, d\Gamma = \sum_f \boldsymbol{u}_f \cdot \boldsymbol{A}_f, \tag{2.9}$$

where $\boldsymbol{A}_f$ is the area weighted face normal vector and $\boldsymbol{u}_f$ is the velocity vector at the cell face f. The interpolation of velocity, from cell centre to cell face, for the mass equation is discussed in Section 2.4.

Transient Term

For the transient term, i.e. the time derivation term in Eq. (2.8), the cell integral can be reduced to

$$\frac{\partial}{\partial t} \int_{\Omega_c} \boldsymbol{u} \, d\Omega = \frac{\partial}{\partial t} V_c \boldsymbol{u}_c, \tag{2.10}$$

in which V_c is the cell volume and $\boldsymbol{u}_c$ is the velocity vector at the cell centre.

Convective Term

The fluid transport (convection) term can be reduced to

$$\begin{aligned}\sum_f \oint_{\Gamma_f} (\boldsymbol{u} \otimes \boldsymbol{u}) \cdot \boldsymbol{n} \, d\Gamma &= \sum_f \oint_{\Gamma_f} \boldsymbol{u}(\boldsymbol{u} \cdot \boldsymbol{n}) \, d\Gamma \\ &= \sum_f Q_f(\boldsymbol{u}_c) F_i.\end{aligned} \tag{2.11}$$

Here $\boldsymbol{u}_f$ is the face value of the velocity, F_i is the face flux defined as

$$F_i = \boldsymbol{u}_i \cdot \boldsymbol{A}_i, \tag{2.12}$$

and Q_f represents an interpolation scheme for determining the velocity at the face from the cell centre values. The QUICK scheme (Leonard, 1991) is applied in the present model, and for the *east* face (e) of cell i, j (see Fig. 2.1) it gives

$$Q_e(\boldsymbol{u}_{i,j}) = \frac{1}{2}(\boldsymbol{u}_{i,j} + \boldsymbol{u}_{i+1,j}) - \frac{1}{8}(\boldsymbol{u}_{i-1,j} - 2\boldsymbol{u}_{i,j} + \boldsymbol{u}_{i+1,j}). \tag{2.13}$$

Pressure Term

For the pressure, the face integral can be reduced to

$$\sum_f \oint_{\Gamma_f} p\boldsymbol{n} \, d\Gamma = \sum_f I_f(p_c) \boldsymbol{A}_f, \tag{2.14}$$

where the linear interpolation operator I_f is applied to the pressure to find the values at the cell faces. I_f gives the value at the *east* face of the i, j cell by

$$I_e(p_{i,j}) = \frac{1}{2}(p_{i+1,j} + p_{i,j}). \tag{2.15}$$

Diffusion Term

The final term in the momentum equation is the diffusion term, which is numerically integrated from

$$\frac{1}{Re} \sum_f \oint_{\Gamma_f} \nabla \boldsymbol{u} \cdot \boldsymbol{n} \, d\Gamma = \frac{1}{Re} \sum_f \boldsymbol{G}_f(\boldsymbol{u}_c) \cdot \boldsymbol{A}_f, \tag{2.16}$$

where $\boldsymbol{G}_f$ is an operator which evaluates the gradient of $\boldsymbol{u}_c$, including cross derivative terms, at the cell face f. In the 2-D case for the *east* face e of cell i, j, the operator $\boldsymbol{G}_f$ gives

$$\begin{aligned}\boldsymbol{G}_e(\boldsymbol{u}_{i,j}) = &\frac{\boldsymbol{A}_{i,j,e}}{\frac{1}{2}(V_{i,j}+V_{i+1,j})}(\boldsymbol{u}_{i+1,j}-\boldsymbol{u}_{i,j}) \\ &+\frac{\frac{1}{4}(\boldsymbol{A}_{i,j,s}+\boldsymbol{A}_{i,j,n}+\boldsymbol{A}_{i+1,j,s}+\boldsymbol{A}_{i+1,j,n})}{\frac{1}{2}(V_{i,j}+V_{i+1,j})} \\ &\cdot\frac{1}{4}(\boldsymbol{u}_{i,j+1}-\boldsymbol{u}_{i,j-1}+\boldsymbol{u}_{i+1,j+1}-\boldsymbol{u}_{i+1,j-1}).\end{aligned} \tag{2.17}$$

2.2.1 Discretisation of Boundary Conditions

For the general variable φ the linear interpolation scheme $I(\varphi)$ and the QUICK scheme $Q(\varphi)$ are, for a Dirichlet type boundary condition where the boundary condition φ_b is implicitly known, given by

$$I_b(\varphi) = Q_b(\varphi) = \varphi_b, \tag{2.18}$$

which means that the Dirichlet condition is given directly from Eq. (2.5) and Eq. (2.18).

The gradient operator determines the boundary cell value based on second order one-sided differences, and is for the *east* face of cell i, j, for the same Dirichlet condition, given by

$$\begin{aligned}\boldsymbol{G}_b(\varphi)_{i,j,e} = &\frac{\boldsymbol{A}_{i,j,e}}{\frac{3}{2}V_{i,j}-\frac{1}{2}V_{i-1,j}}\left(\frac{8}{3}\varphi_b-\frac{9}{3}\varphi_{i,j}+\frac{1}{3}\varphi_{i-1,j}\right) \\ &+\frac{\frac{3}{4}(\boldsymbol{A}_{i,j,s}+\boldsymbol{A}_{i,j,n})-\frac{1}{4}(\boldsymbol{A}_{i+1,j,s}+\boldsymbol{A}_{i+1,j,n})}{\frac{3}{2}V_{i,j}-\frac{1}{2}V_{i-1,j}}\left(\frac{3}{4}(\varphi_{i,j+1}-\varphi_{i,j-1})\right. \\ &\left.-\frac{1}{4}(\varphi_{i-1,j+1}-\varphi_{i-1,j-1})\right).\end{aligned} \tag{2.19}$$

Moreover, the value at the boundary φ_b for the Neumann condition can be found by solving

$$\boldsymbol{G}_b(\varphi)\cdot\boldsymbol{A}_b = r. \tag{2.20}$$

2.3 Free Surface Modelling

The free surface is described by a volume-of-fluid (VOF) method. A further description of VOF methods and the associated transport schemes used for the solution of the VOF equation is given in Chapter 3.

In this type of free surface modelling, the computational grid is extended above the free surface in order to be able to capture the free surface at all time steps. For the free surface, a special scheme has been implemented to enforce the free surface boundary conditions. For general free surface flows, the dynamic free surface boundary condition states equilibrium of stresses across the interface

$$\sigma_{ij}^{\text{liq}} n_j = \sigma_{ij}^{\text{gas}} n_j + \gamma \kappa n_i, \tag{2.21}$$

where the superscript $^{\text{liq}}$ and superscript $^{\text{gas}}$ indicate quantities for liquid and gas, respectively, n_j is the outward pointing normal vector for the free surface, γ is the surface tension coefficient and κ is the surface curvature. σ_{ij} is the stress tensor defined as

$$\sigma_{ij} = \nu \left(\frac{\partial u_i}{\partial x_j} + \frac{\partial u_j}{\partial x_i} \right) - \tilde{p} \delta_{ij}, \tag{2.22}$$

where δ_{ij} is Kronecker's delta. However, in the applications considered in the present work, the viscous boundary layer on the free surface and the effect of surface tension can be considered negligible, which gives the following condition for pressure:

$$\tilde{p} = 0. \tag{2.23}$$

Since the pressure variable which is solved for includes gravitational acceleration, the following boundary condition is imposed:

$$p_{fs}^{n+1} = -g(x_{fs}^{n+1} - x_{fs,0}), \tag{2.24}$$

where p_{fs}^{n+1} is the pressure on the free surface at the new time step, x_{fs}^{n+1} is the free surface location at the new time step $n+1$, and $x_{fs,0}$ is the initial free surface location.

For the velocity, the general kinematic boundary condition (Eq. (2.21)) imposes a Dirichlet type condition on the free surface. However, since near surface boundary layers are considered negligible, no boundary condition is present for velocity. In order to find values at the cell face for the velocity field near the free surface, an extrapolation scheme is applied which satisfies the homogeneous Neumann condition on the free surface, i.e.

$$\frac{\partial \boldsymbol{u}}{\partial n_{fs}} = 0, \tag{2.25}$$

where n_{fs} is the normal vector to the free surface.

2.3.1 Discretised Free Surface Boundary Conditions

The discretisation of the free surface is shown in Fig. 2.2. When the Laplace operator is constructed for solving the pressure Poisson equation or the Poisson equation for the velocity correction (see Section 2.4), the values of a variable φ at the *north* cell face for cell i, j are

found by second order one-sided extrapolation, i.e. by forcing a second order polynomial through the values at i, j and $i, j-1$ along with the value in the free surface location. The operator which satisfies the inhomogeneous Dirichlet condition (Eq. (2.5)) gives the following value at the *north* cell face:

$$E_{VD,n}(\varphi_c) = \frac{1}{3+8l+4l^2}\left((9l+6l^2)\varphi_{i,j}\boldsymbol{A}_{i,j,n} + (-1-2l^2)\varphi_{i,j-1}\boldsymbol{A}_{i,j,s} + 3r)\right), \tag{2.26}$$

where E_V is the operator for the value at the face nearest to the free surface, and l is the distance from the face to the discretised free surface (see Fig. 2.2). The derivative operator, which satisfies the same inhomogeneous Dirichlet condition on the discretised free surface location, gives the following in the face normal direction:

$$E_{DD,n}(\varphi_c) = \frac{1}{3+8l+4l^2}\left((-9+4l)\varphi_{i,j}\boldsymbol{A}_{i,j,n} + (1-4l^2)\varphi_{i,j-1}\boldsymbol{A}_{i,j,s} + 8r)\right), \tag{2.27}$$

Similarly, the operator, leading to the value at the face that satisfies the homogeneous Neumann condition (Eq. (2.6) with $r = 0$) on the free surface is given by

$$E_{VN,n}(\varphi_c) = \frac{1}{8+8l}\left((9+12l)\varphi_{i,j}\boldsymbol{A}_{i,j,n} + (-1-4l)\varphi_{i,j-1}\boldsymbol{A}_{i,j,s})\right), \tag{2.28}$$

Finally, the operator leading to the derivative of the value in the face normal direction that satisfies the homogeneous Neumann condition at the free surface is given by

$$E_{DN,n}(\varphi_c) = \frac{1}{8+8l}\left((9+12l)\varphi_{i,j}\boldsymbol{A}_{i,j,n} + (-1-4l)\varphi_{i,j-1}\boldsymbol{A}_{i,j,s})\right), \tag{2.29}$$

These operators (E_{VD}, E_{DD}, E_{VN} and E_{DN}) are all used implicitly in the solution of the Poisson equations. In cases where the cell opposite to the face (in this case $i, j-1$) is not a fluid cell, a first order extrapolation scheme is applied.

2.4 Time Discretisation

For the time integration a semi-implicit scheme, similar to that of Zang *et al.* (1994), is employed. The scheme uses both implicit and explicit terms for discretisation of the dependent variables, where an Adams-Bashforth method is applied to the explicit terms, and a Crank-Nicholson method is applied to the implicit terms. The general solution procedure follows a fractional step approach where an intermediate velocity field is first found by solving the discretised momentum equation. Next step is solution of a corrector equation in order to obtain a divergence free velocity field which satisfies the mass conservation equation. Finally, the pressure is found by solving a Laplace equation, formulated by taking the divergence of the momentum equation.

Although a number of methods of implicit and explicit discretisations of the convective and the diffusive terms have been implemented in the code, the present study uses only the

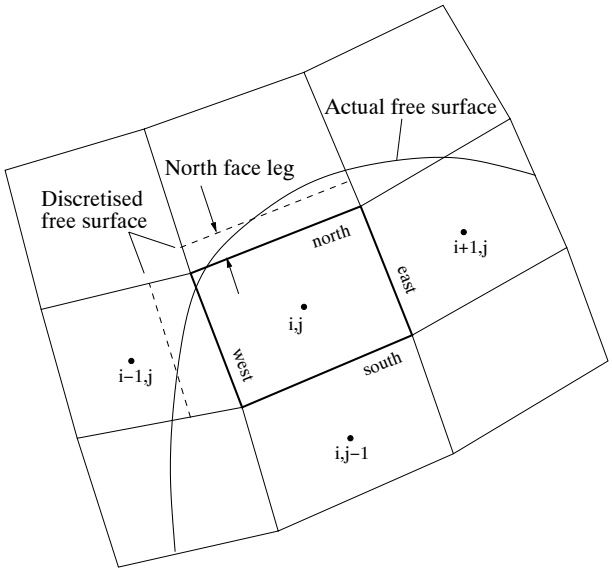

Figure 2.2: *Discretisation of the free surface.*

following formulation for the discretised momentum equation:

$$\begin{aligned}\frac{V_c}{\Delta t}(\boldsymbol{u}_c^* - \boldsymbol{u}_c^n) = &-\left(\frac{3}{2}Q_f(\boldsymbol{u}_c^n)I_f(\boldsymbol{u}_c^n) - \frac{1}{2}Q_f(\boldsymbol{u}_c^{n-1})I_f(\boldsymbol{u}_c^{n-1})\right)\cdot\boldsymbol{A}_f \\ &-\left(\frac{3}{2}I_f(p_c^n) - \frac{3}{2}I_f(p_c^{n-1})\right)\boldsymbol{A}_f + \frac{1}{2Re}\left(\boldsymbol{G}_f(\boldsymbol{u}_c^*) + \boldsymbol{G}_f(\boldsymbol{u}_c^n)\right)\cdot\boldsymbol{A}_f\end{aligned} \tag{2.30}$$

where superscript ^{n} and $^{n-1}$ indicate values at time levels n and $n-1$, respectively. Superscript * denotes the first prediction of values at the new time level. For simplicity summation over cell faces ($\sum_f$) is omitted from all terms on the right hand side.

The terms containing values at the new time level can be isolated on the left hand side of Eq. (2.30), which gives

$$\begin{aligned}\frac{V_c}{\Delta t}\boldsymbol{u}_c^* - \frac{1}{2Re}\boldsymbol{G}_f(\boldsymbol{u}_c^*)\cdot\boldsymbol{A}_f = &\frac{V_c}{\Delta t}\boldsymbol{u}_c^n - \left(\frac{3}{2}Q_f(\boldsymbol{u}_c^n)I_f(\boldsymbol{u}_c^n) - \frac{1}{2}Q_f(\boldsymbol{u}_c^{n-1})I_f(\boldsymbol{u}_c^{n-1})\right)\cdot\boldsymbol{A}_f \\ &-\left(\frac{3}{2}I_f(p_c^n) - \frac{3}{2}I_f(p_c^{n-1})\right)\boldsymbol{A}_f + \frac{1}{2Re}\boldsymbol{G}_f(\boldsymbol{u}_c^n)\cdot\boldsymbol{A}_f.\end{aligned} \tag{2.31}$$

When Eq. (2.31) is solved intermediate values for velocities are obtained, which does not satisfy the mass conservation equation. Therefore the velocity field is corrected by the field ϕ, which is found by solving the following Poisson equation:

$$\sum_f \boldsymbol{G}_f(\boldsymbol{G}_c(\phi))\cdot\boldsymbol{A}_f = -\sum_f I_f(\boldsymbol{u}_c^*)\cdot\boldsymbol{A}_f, \tag{2.32}$$

where $\boldsymbol{G}_c$ is the gradient operator that determines the gradient of the field at the (i, j) cell centre by

$$\begin{aligned}\boldsymbol{G}_c = \frac{1}{2V_c}\left[(\boldsymbol{u}_{i+1,j} + \boldsymbol{u}_{i,j})\boldsymbol{A}_{i,j,w} - (\boldsymbol{u}_{i-1,j} + \boldsymbol{u}_{i,j})\boldsymbol{A}_{i,j,e}\right. \\ \left.+(\boldsymbol{u}_{i,j+1} + \boldsymbol{u}_{i,j})\boldsymbol{A}_{i,j,n} - (\boldsymbol{u}_{i,j-1} + \boldsymbol{u}_{i,j})\boldsymbol{A}_{i,j,s}\right].\end{aligned} \tag{2.33}$$

When ϕ has been found the velocity field can be corrected at the new time step by

$$\boldsymbol{u}_c^{n+1} = \boldsymbol{u}_c^* - \boldsymbol{G}_c(\phi). \tag{2.34}$$

Finally, the pressure field must be computed at the new time level. This is done by taking the divergence of the momentum equation, which gives the following Poisson equation for pressure:

$$\begin{aligned}\sum_f \boldsymbol{G}_f(\boldsymbol{G}_c(p^{n+1})) \cdot \boldsymbol{A}_f = -\sum_f \boldsymbol{G}_f(\sum_f [Q_f(\boldsymbol{u}_c^{n+1}) I_f(\boldsymbol{u}^{n+1}c) \cdot \boldsymbol{A}_f]) \cdot \boldsymbol{A}_f \\ + \sum_f \boldsymbol{G}_f(\sum_f [\frac{1}{Re}\boldsymbol{G}_f(\boldsymbol{u}_c^{n+1}) \cdot \boldsymbol{A}_f]) \cdot \boldsymbol{A}_f.\end{aligned} \tag{2.35}$$

2.4.1 Equation Solvers

The first estimate of velocities at the new time step (the predictor step), found from Eq. (2.31), result in a linear equation system, which is solved by applying an iterative solver, using Gauss-Seidel line relaxation. The Poisson equations for the velocity corrector ϕ and for the pressure p are solved by using the plane-ILLU (Incomplete Line Lower Upper decomposition) solver applied on a V-cycle multigrid method.

Overall Solution Procedure

The overall solution procedure for the Navier-Stokes solver can be described by the following steps:

- **Predictor step**
  Solve the discretised momentum equation (Eq. (2.31)) using the iterative Gauss-Seidel solver to obtain estimates of velocities $\boldsymbol{u}_c^*$ at the new time step.
- **Corrector step 1**
  Solve the Poisson equation (Eq. (2.32)) for the velocity corrector ϕ.
- **Corrector step 2**
  Correct the intermediate velocity field $\boldsymbol{u}_c^*$ by ϕ using Eq. (2.34), so that $\boldsymbol{u}_c^{n+1}$ is divergence free.

- **Compute pressure**
  Solve the Poisson equation for pressure (Eq. (2.35)) at the new time step using the multigrid Poisson solver.

Before the solution method is applied to some benchmark tests, the free surface modelling scheme and different VOF transport algorithms are investigated in the following chapter.

Chapter 3

Free Surface Modelling

When free surface flows are modelled, a number of techniques are available to compute the interface. This chapter briefly outlines the various options with regard to free surface handling and describes the methods implemented in NS3.

In general, the existing methods for handling free surfaces and fluid interfaces in CFD can be divided into two groups (Ferziger and Perić, 1997):

- Surface tracking
- Surface capturing

The surface tracking methods are characterised by an explicit representation of the surface. This is normally done by adapting the grid to the free surface and updating the grid at each time step to track the new location of the free surface by use of a height function to describe the vertical height of the free surface location. The drawback of the surface tracking methods is the inability to handle complex surface geometries and overturning waves. This makes the surface tracking methods unable to model the wave pattern of for instance high-speed crafts, in which case overturning waves are expected or breaking waves in general. Surface tracking is still widely used in ship CFD when effects of overturning or breaking waves are considered negligible.

The surface capturing methods use a different approach. A number of schemes are available, and all use an implicit representation of the interface which is then captured as part of the solution algorithm. This requires that the computational grid extends above the region containing fluid in order to be able to capture the surface throughout the computation. In cases of moving structures or boundaries, the surface capturing methods can also be coupled with Lagrangian grids, forming a type of arbitrary Lagrangian Eulerian (ALE) method, by which a structure is tracked by the grid (Lagrangian) and the grid in the remaining domain is moved along.

The most common schemes for surface capturing are the marker-and-cell method (MAC) (Harlow and Welch, 1965), the level-set method (LSM) (Osher and Sethian, 1988) and the volume-of-fluid method (VOF) (Hirt and Nichols, 1981). In the MAC scheme, massless particles are introduced in the liquid filled part of the domain, and the particles are tracked as part of the solution procedure. The level-set method introduces a scalar which defines the minimum distance in the domain to the fluid interface. The scalar is integrated in time by solving a transport equation. The VOF method introduces a scalar which defines the filling degree of each cell. This field is also integrated in time by solving a transport equation. The main advantage of the surface capturing methods is their ability to capture complex surface geometries with overturning or breaking waves and splashing, but the drawback is the possibility of numerical instability, diffusivity (with blurred interface) or grid alignment. However, these issues have been dealt with in many recent implementations using VOF schemes (Repetto, 2001; Muzaferija *et al.*, 1998; Ubbink, 1997), and in general the surface capturing methods show promising results.

In the present study surface capturing, by application of the VOF method is used. The NS3 code also has a surface tracking scheme implemented, as reported in Mayer *et al.* (1998), but since all problems in the present thesis involve complex free surface geometries, surface tracking methods are not applied and will not be further described here.

3.1 The Volume-of-Fluid Method

The basis of the volume-of-fluid method is that to each cell an additional scalar is assigned which is the VOF (or volume fraction) value giving the degree of filling for the cell. A cell with a volume fraction value of 0 is void, and a volume fraction value of 1 equals a full cell. If the value is between 0 and 1 the cell contains a free surface, i.e.

$$\alpha = \frac{\text{Volume of fluid in cell}}{\text{Total cell volume}} \tag{3.1}$$

where α is the volume fraction and 1-α is the volume fraction of the void or the air in the cell. Initially, all cells are given a volume fraction value, and at each time step a transport equation is solved to find the distribution of fluid at the new time step:

$$\frac{\partial \alpha}{\partial t} + \nabla \cdot \alpha \boldsymbol{u} = 0 \tag{3.2}$$

where t is time and $\boldsymbol{u}$ is the velocity vector.

Within the VOF methods two different approaches are possible: one is to neglect the effect of air in surface and void cells and only solve the RANS equations in the cells with a volume fraction value different from 0 (one-fluid approach), and the other is to solve the RANS equations in all cells, treating the interface as a shift in fluid properties (two-fluid approach). The present study is based on a one-fluid approach, but the equations and derivations can easily be extended to a two-fluid approach, for a further description see Ubbink (1997). The boundary conditions for the free surface are described in Chapter 2. Moving grids can be applied in combination with the VOF method but are not used in this study.

3.1.1 Discretised Equations

In integral form over the control volume and with time step δt, Eq. (3.2) is written as

$$\int_t^{t+\delta t} \left(\int_\Omega \frac{\partial \alpha}{\partial t} d\Omega \right) dt + \int_t^{t+\delta t} \left(\int_\Omega \nabla \cdot \alpha \boldsymbol{u} \, d\Omega \right) dt = 0 \tag{3.3}$$

In a constant volume cell (labelled c) where Ω_c is the volume, the first term of Eq. (3.3) can be reduced to

$$\begin{aligned} \int_t^{t+\delta t} \left(\int_\Omega \frac{\partial \alpha}{\partial t} d\Omega \right) dt &= \int_t^{t+\delta t} \left(\frac{\partial \alpha}{\partial t} \Omega_c \right) dt \\ &= \left(\alpha_c^{t+\delta t} - \alpha_c^t \right) \Omega_c \end{aligned} \tag{3.4}$$

Gauss' theorem can be applied to the volume integral in the second term (convection term) of Eq. (3.3):

$$\int_\Omega \nabla \cdot \alpha \boldsymbol{u} \, d\Omega = \oint_{\partial\Gamma} \alpha \, d\Gamma \cdot \boldsymbol{u} \approx \sum_{f=1}^{n} \alpha_f A_f \cdot \boldsymbol{u}_f = \sum_{f=1}^{n} \alpha_f F_f \tag{3.5}$$

where dS is the surface area vector, f indicates the face value, A_f is the discretised face area vector and n is the number of faces. F_f is the volumetric flux defined as

$$F_f = A_f \cdot \boldsymbol{u}_f \tag{3.6}$$

To calculate the time integral of Eq. (3.5) the formulation of Versteeg and Malalasekera (1995) is introduced:

$$\int_t^{t+\delta t} \left(\sum_{f=1}^{n} \alpha_f F_f \right) dt = \sum_{f=1}^{n} \left((1-\eta) \left[\alpha_f F_f \right]^t + \eta \left[\alpha_f F_f \right]^{t+\delta t} \right) \delta t \tag{3.7}$$

where η is a weighting factor for time integration. The following are most commonly used: $\eta = 0$ for explicit calculations, $\eta = 1$ for implicit calculations and $\eta = \frac{1}{2}$ for a Crank-Nicholson type scheme. Here the Crank-Nicholson scheme is used.

The second term on the right hand side of Eq. (3.7) shows that a velocity field at the new time step is needed as part of the solution to the implicit VOF equation. In the present implementation, the new α field is found before the normal solution algorithm is started, where velocity and pressure are integrated to the new time step. This means that $F_f^{t+\delta t}$ is not available at the time when Eq. (3.7) is solved. Since the variation in F can be considered negligible compared to the variation of α, the volumetric flux of the previous time step can be used. An Adams-Bashforth scheme is applied, which is used to give an estimate of the flux field at $t + \delta t$ as

$$F_{f,AB}^{t+\delta t} = \left(\frac{3}{2} \boldsymbol{u}^t - \frac{1}{2} \boldsymbol{u}^{t-\delta t} \right) \cdot \boldsymbol{A}_f, \tag{3.8}$$

where $F_{f,AB}^{t+\delta t}$ is the flux field at the new time step predicted by the Adams-Bashforth scheme. In the following this flux field will just be denoted F_f. This gives the following formulation of Eq. (3.7):

$$\left(\alpha_c^{t+\delta t} - \alpha_c^t\right) \Omega_c = \sum_{f=1}^{n} \frac{1}{2} \left(\alpha_f^t + \alpha_f^{t+\delta t}\right) F_f \delta t \tag{3.9}$$

Hence, the final formulation for the volume fraction at time step $t + \delta t$ becomes:

$$\alpha_c^{t+\delta t} = \alpha_c^t - \frac{1}{\Omega_c} \sum_{f=1}^{n} \frac{1}{2} \left(\alpha_f^t + \alpha_f^{t+\delta t}\right) F_f \delta t \tag{3.10}$$

In the following section, the different schemes for calculating the volume fraction at the cell faces (α_f) are described.

3.2 Volume Fraction Differencing Schemes

To have a common reference throughout the computational domain, the definition of the cell arrangement is shown in Fig. 3.1. Here α_D is the volume fraction of the donor cell, α_A is the volume fraction of the acceptor cell and α_U is the volume fraction of the upwind cell. α_f is the volume fraction at the face between the donor and acceptor cells. The figure only shows the cell arrangement in one dimension, but can be extended to two and three dimensions.

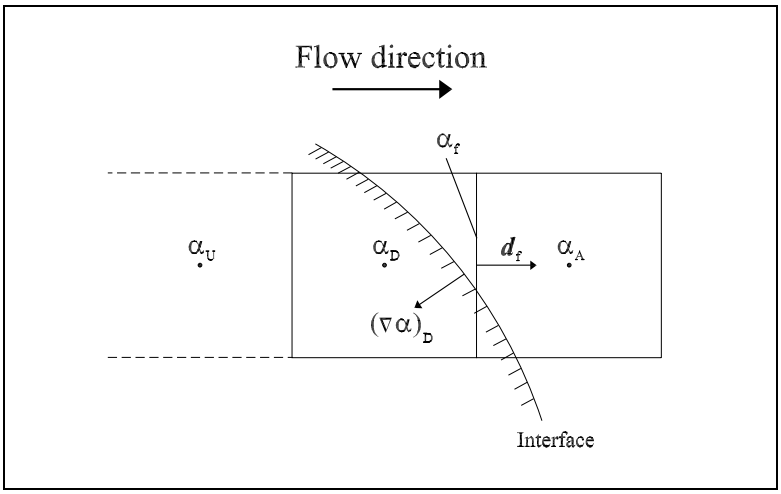

Figure 3.1: *Cell arrangement definition.*

The schemes considered here are based on normalised variables (NV) (Leonard, 1991). The definition of a normalised variable is:

$$\tilde{\alpha} = \frac{\alpha - \alpha_U}{\alpha_A - \alpha_U} \tag{3.11}$$

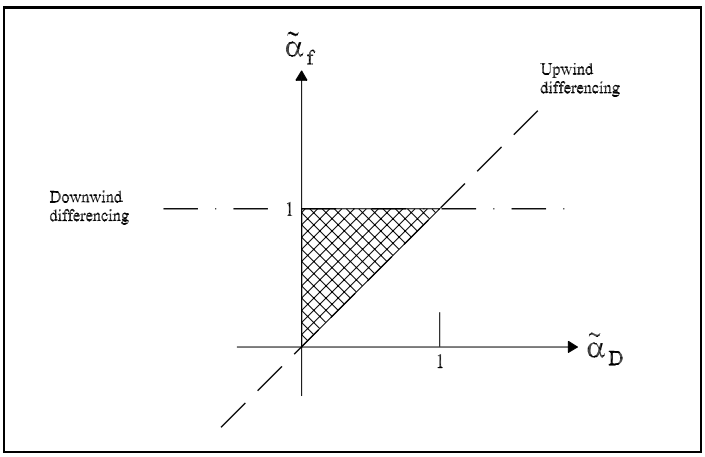

Figure 3.2: *Normalised variable diagram (NVD) with CBC.*

The normalized donor cell centre value is given from Eq. (3.11):

$$\tilde{\alpha}_D = \frac{\alpha_D - \alpha_U}{\alpha_A - \alpha_U} \tag{3.12}$$

where α_D is the donor cell volume fraction and $\tilde{\alpha}_D$ is the normalised value of the donor cell volume fraction. A normalised variable diagram is a graphical way of showing how the normalised volume fraction at the cell face ($\tilde{\alpha}_f$) is calculated from the normalised donor cell centre value ($\tilde{\alpha}_D$). Fig. 3.2 presents a sketch of a normalised variable diagram with the boundaries for upwind and downwind differencing. These boundaries constitute the Convection Boundedness Criteria (CBC) (Gaskell and Lau, 1988) for implicit calculations assuring local boundedness, and they are shown in the shaded region.

The mathematical formulation of the CBC for implicit calculations is

$$\begin{aligned} \tilde{\alpha}_f &= \tilde{\alpha}_D \qquad \text{For} \quad \tilde{\alpha}_D < 0 \quad \text{or} \quad \tilde{\alpha}_D > 1 \\ \tilde{\alpha}_D \leq \tilde{\alpha}_f &\leq 1 \qquad \text{For} \quad 0 \leq \tilde{\alpha}_D \leq 1 \end{aligned} \tag{3.13}$$

This only preserves local boundedness for implicit flow calculations, and in Leonard (1991) it was shown that the CBC for explicit flow calculations can be derived. The explicit CBC are based on the cell Courant-Friederich-Lewy (CFL) number, which is defined as

$$C_D = \frac{\Delta t \; F_{cell}}{\Omega_D} \tag{3.14}$$

where Δt is the time increment, F_{cell} is the total flux out of the cell (considered positive) and Ω_D is the total volume of the donor cell. C_D is the cell CFL number. The CBC for explicit flow calculations, for multidimensional flow, are then defined as

$$\begin{aligned} \tilde{\alpha}_f &= \tilde{\alpha}_D \qquad\qquad\qquad \text{For} \quad \tilde{\alpha}_D < 0 \quad \text{or} \quad \tilde{\alpha}_D > 1 \\ \tilde{\alpha}_D \leq \tilde{\alpha}_f &\leq \min\left\{1, \frac{\tilde{\alpha}_D}{C_D}\right\} \qquad \text{For} \quad 0 \leq \tilde{\alpha}_D \leq 1 \end{aligned} \tag{3.15}$$

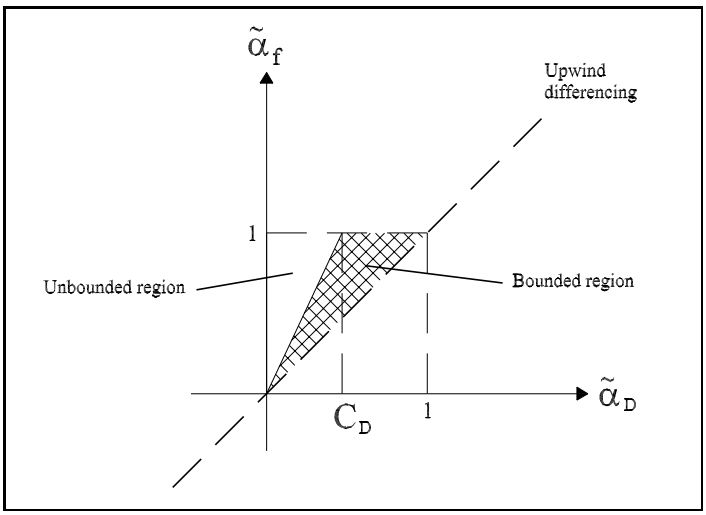

Figure 3.3: *NVD for explicit calculations with CBC*

This boundedness criterion in shown in Fig 3.3, and it is valid for both 1-D, 2-D and 3-D calculations. For 1-D, C_D reduces to C_f, which is the face CFL number. The upper limit for this new CBC corresponds to the Hyper-C differencing scheme (Leonard, 1991).

All schemes based on normalised variables use the upwind value when $\tilde{\alpha}_D < 0$ or $\tilde{\alpha}_D > 1$. For values $0 \leq \tilde{\alpha}_D \leq 1$, the resulting normalised face volume fraction ($\tilde{\alpha}_f$) with the schemes is shown in Table 3.1.

Scheme	$\tilde{\alpha}_f$
Hyper-C	$\text{Min}\left\{1, \frac{\tilde{\alpha}_D}{C_D}\right\}$
UltimateQuickest	$\text{Min}\left\{\frac{8C_D\tilde{\alpha}_D+(1-C_D)(6\tilde{\alpha}_D+3)}{8}, \tilde{\alpha}_{f,\text{Hyper-C}}\right\}$
CICSAM	$\gamma_f\tilde{\alpha}_{f,\text{Hyper-C}} + (1-\gamma_f)\tilde{\alpha}_{f,\text{UQ}}$
HRIC	$\begin{cases} 2\tilde{\alpha}_f & \text{for} \quad \tilde{\alpha}_D \leq 0.5 \\ 1 & \text{for} \quad \tilde{\alpha}_D > 0.5 \end{cases}$

Table 3.1: *Volume fraction schemes ($0 \leq \tilde{\alpha}_D \leq 1$)*

The Hyper-C scheme is identical to the downwind boundary of the CBC for explicit calculations and thus very compressive, which means that the scheme will always keep the interface very sharp. The UltimateQuickest scheme is derived from the QUICK upwind scheme, which is diffusive, and thus makes the interface extend over many cells. The CICSAM consists of a blend of the Hyper-C scheme and the UltimateQuickest scheme, using a weighting factor

(γ_f) which depends on the orientation of the interface with respect to the cell face and is defined as

$$\gamma_f = \frac{\cos(2\theta_f) + 1}{2} \tag{3.16}$$

where

$$\theta_f = \arccos \left| \frac{(\nabla\alpha)_D \cdot \boldsymbol{d}_f}{|(\nabla\alpha)_D|\,|\boldsymbol{d}_f|} \right| \tag{3.17}$$

In Fig. 3.4 the switching function is shown as a function of the angle between the interface and the face normal (θ). $(\nabla\alpha)_D$ is the gradient of the volume fraction field and $\boldsymbol{d}_f$ is the face normal (see Fig. 3.1).

In the HRIC scheme, a correction for the interface orientation and for the CFL number is also made. The interface correction, like for the CICSAM scheme, is according to the angle between the interface and the face normal θ and interpolates between the upwind and downwind values (Fig. 3.4):

$$\tilde{\alpha}_f^* = \sqrt{\cos\theta}\;\tilde{\alpha}_f + \left(1 - \sqrt{\cos\theta}\right)\;\tilde{\alpha}_D \tag{3.18}$$

where the upwind value is $\tilde{\alpha}_D$, the downwind value is given in Table 3.1 and the switching function is $f_{switch} = \sqrt{\cos\theta}$. The HRIC scheme takes the CFL number into account according to

$$\tilde{\alpha}_f^{**} = \begin{cases} \tilde{\alpha}_f^* & \text{if } C_D < 0.3 \\ \tilde{\alpha}_D & \text{if } C_D > 0.7 \\ \tilde{\alpha}_D + \left(\tilde{\alpha}_f^* - \tilde{\alpha}_D\right)\frac{0.7 - C_D}{0.7 - 0.3} & \text{otherwise} \end{cases} \tag{3.19}$$

and the resulting value is $\tilde{\alpha}_f^{**}$.

The normalised variable diagrams of all four schemes are shown in Fig. 3.5.

The result from the interface capturing schemes is the normalised face volume fraction, from which the actual face volume fraction can be calculated:

$$\alpha_f = \tilde{\alpha}_f \alpha_A + (1 - \tilde{\alpha}_f)\alpha_U \tag{3.20}$$

This can be rewritten as

$$\alpha_f = \beta_f \alpha_A + (1 - \beta_f)\alpha_D \tag{3.21}$$

where

$$\beta_f = \frac{\tilde{\alpha}_f - \tilde{\alpha}_D}{1 - \tilde{\alpha}_D} \tag{3.22}$$

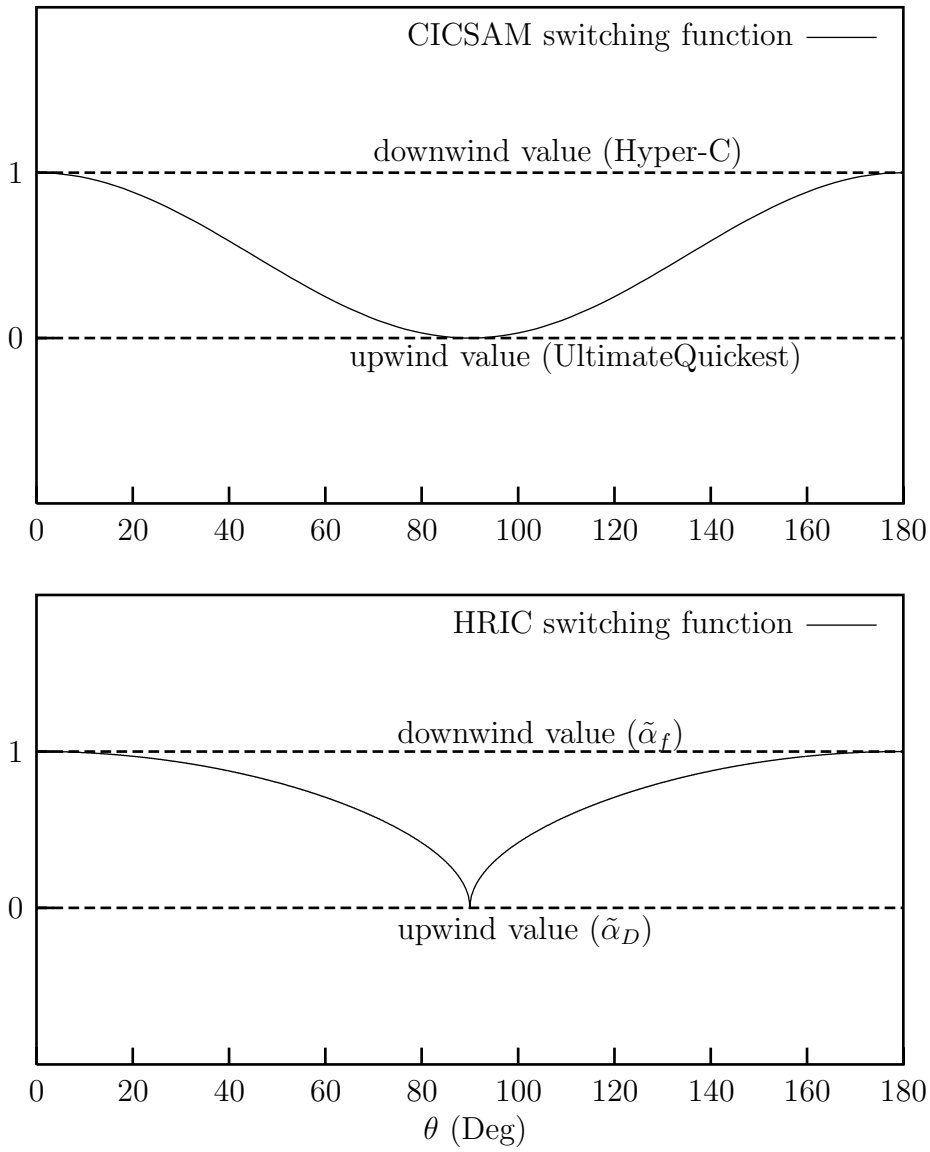

Figure 3.4: *Switching functions for CICSAM (top) and HRIC.*

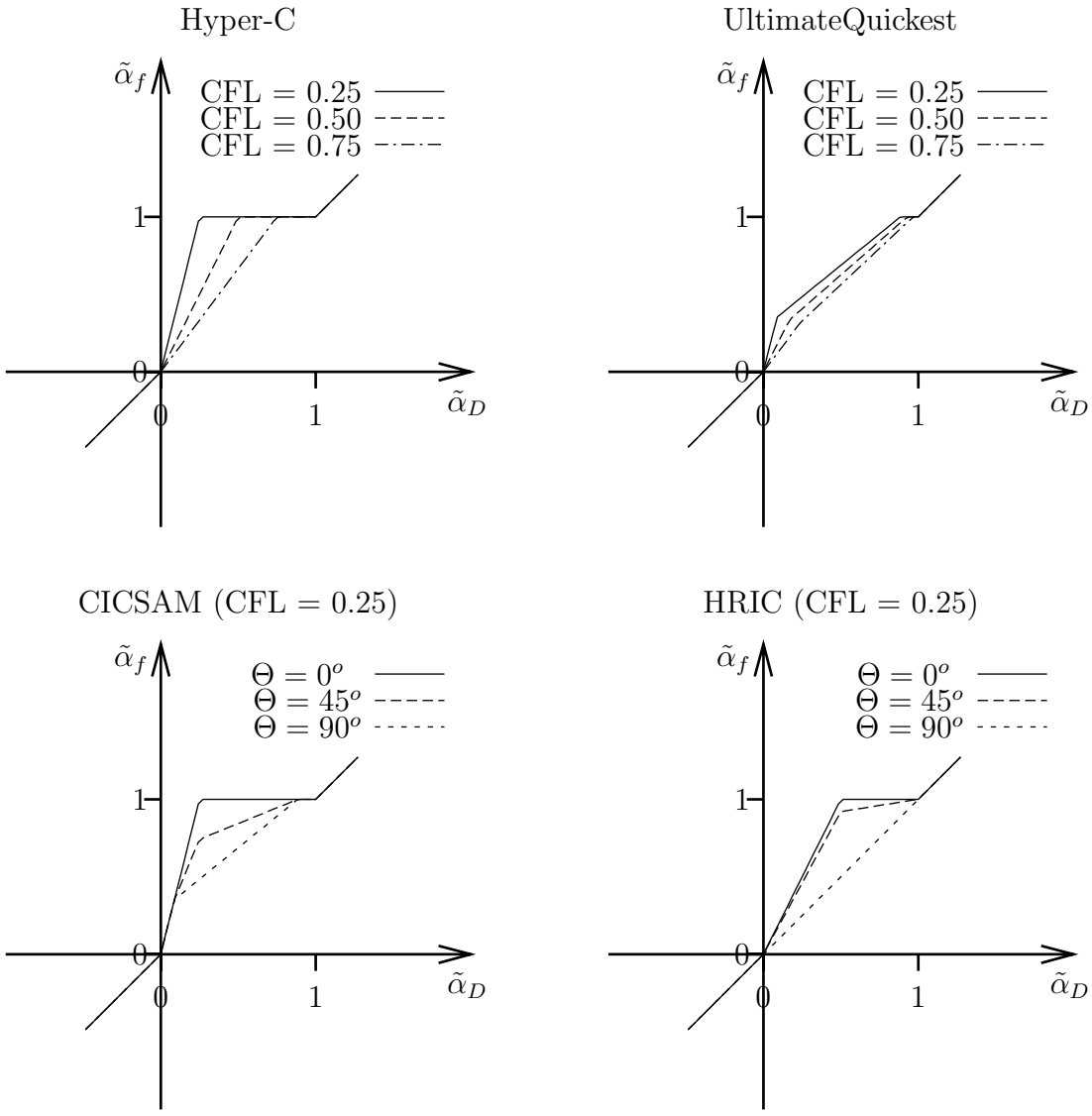

Figure 3.5: *NVD's for Hyper-C, UQ, CICSAM and HRIC*

The schemes described here are not fully bounded, meaning that the resulting α values might yield $\alpha^{t+\delta t} < 0$ or $\alpha^{t+\delta t} > 1$. The original VOF method (Hirt and Nichols, 1981) use a filtering technique where the unbounded volume fraction values were reset to either 0 or unity after each update. It was assumed that the errors introduced here would cancel out.

The CICSAM scheme adopts a more consistent approach where the magnitude of the unboundedness is used to either upwind or downwind the scheme more, depending on the nature of the unboundedness. If a cell is filled beyond a value of 1 the scheme corrects the predicted inflow, so that the resulting value is bounded (= 1), and similarly for resulting values below 0. This approach is labelled the corrector step and a full description is given in Ubbink (1997).

3.2.1 VOF Cleaning Routine

As described in Chapter 2, the mass and momentum equations are only solved for the fluid (water) phase, and the interaction between gas (air) and fluid is neglected. So velocity and pressure in void cells are reset to zero after each time step. However, in order to be able to find values at cell faces for cells in the free surface region, an extrapolation scheme is applied where velocity and pressure from full cells ($\alpha > 0.5$) are extrapolated to surface cells ($\alpha < 0.5$). This requires a sharp interface where the free surface is located in a single cell in the transition from full to void cells, in order to be able to track cells in the surface region. Therefore, pressure and velocity are not computed for cells outside the first layer of surface cells. If these cells still contain a small α value, even after the boundedness schemes in the corrector step, the value is 'cleaned', i.e. reset to 0. The same step is performed for cells in the fluid region where a cell with $\alpha < 1$ which is not next to a surface cell will be reset to 1. This cleaning routine is performed in order to avoid having cells in the computational domain which have a non-zero α value, but are inactive in the sense that the mass and momentum equations are not solved for the cell. The cleaning routine will only have an insignificant effect on the total conservation of the α field, except in cases where large fluid detachments and overturning waves are very extensive. An example of a problem of conserving the α field is given in Chapter 5, where fluid sloshing in a tank results in fluid detachments and breaking waves in a small confined space.

In the following, various surface capturing schemes are evaluated by use of a simple convection test.

3.3 Convection Test

To aquire a measure of how well the various surface capturing schemes perform, a simple convection test is used. The test consists of convecting an initial circular volume fraction field across a mesh which is a regular, uniform 200×100 grid as shown in Fig. 3.6. An initial volume fraction field is placed in the lower left corner and then convected through the mesh by a time-independent oblique velocity field. The volume fraction field should ideally be convected to the upper right corner with an unchanging profile.

The tests are all made with a CFL number of 0.15. In Fig. 3.7 the resulting volume fraction field, after convection through the 200×100 grid, is shown for CICSAM and Hyper-C together with the initial volume fraction distribution. The figure shows that both schemes do not preserve the interface fully, Hyper-C transforms it into a step profile and CICSAM aligns the interface, to some extent, with the mesh.

In Fig. 3.8 the convection test is shown for HRIC and UltimateQuickest. The HRIC scheme shows a significant smear, which gives the interface at least two cells from void to full cells, and grid alignment is also seen in the figure. The UltimateQuickest scheme is even more

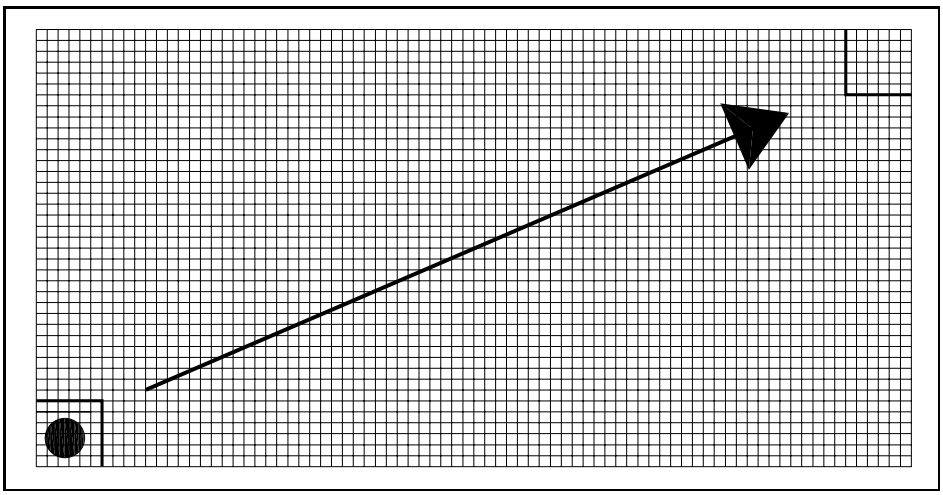

Figure 3.6: *Setup for convection test (*200×100 *grid cells)*

diffusive, due to the high degree of upwinding used in the scheme. However, this is the feature needed in the CICSAM scheme when the field gradient is normal to the flow direction. On its own the scheme does not preserve a sharp interface in multiple dimensions, so neither HRIC or UltimateQuickest are considered to be preferred options for interface capturing.

The original Hirt-Nicholson VOF method was also tested in the oblique velocity field. This produced an unphysical deformation of the volume fraction field and created *flotsam* ('floating wreckage') and *jetsam* ('jettisoned goods') (Noh and Woodward, 1976). In other studies (Rudman (1997), Ubbink (1997)) this has been avoided by either operator splitting or a corrected multidimensional scheme, which has not been implemented here.

From all the tested transport algorithms, the CICSAM and Hyper-C schemes showed the most promising results. All methods have been implemented in the NS3 code, but for general purposes the CICSAM method is considered to be the best option. In the following, all computations utilise the CICSAM scheme.

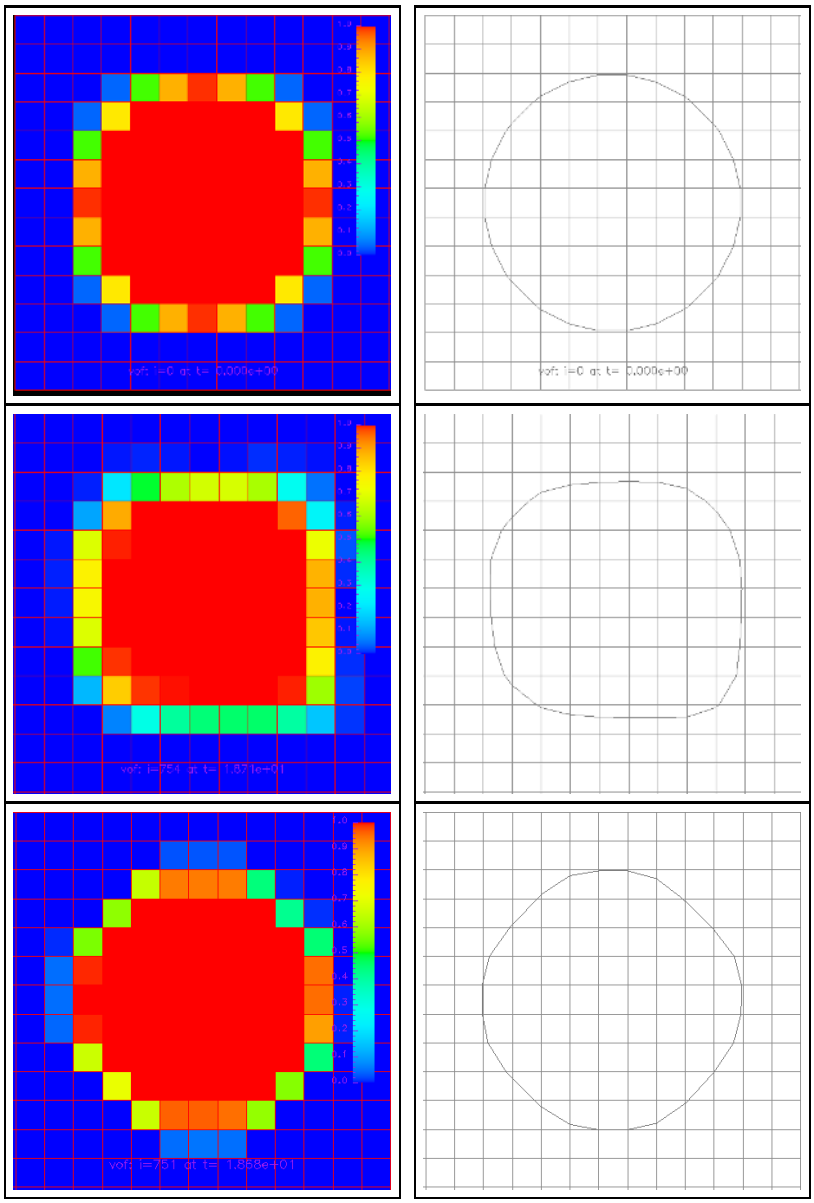

Figure 3.7: *Initial and final volume fraction fields for convection test with CICSAM and Hyper-C schemes. Colour field representation of the volume fraction α shown left, and isoline (with the isoline value $\alpha = 0.5$) shown right.* ($C_D = 0.15$).

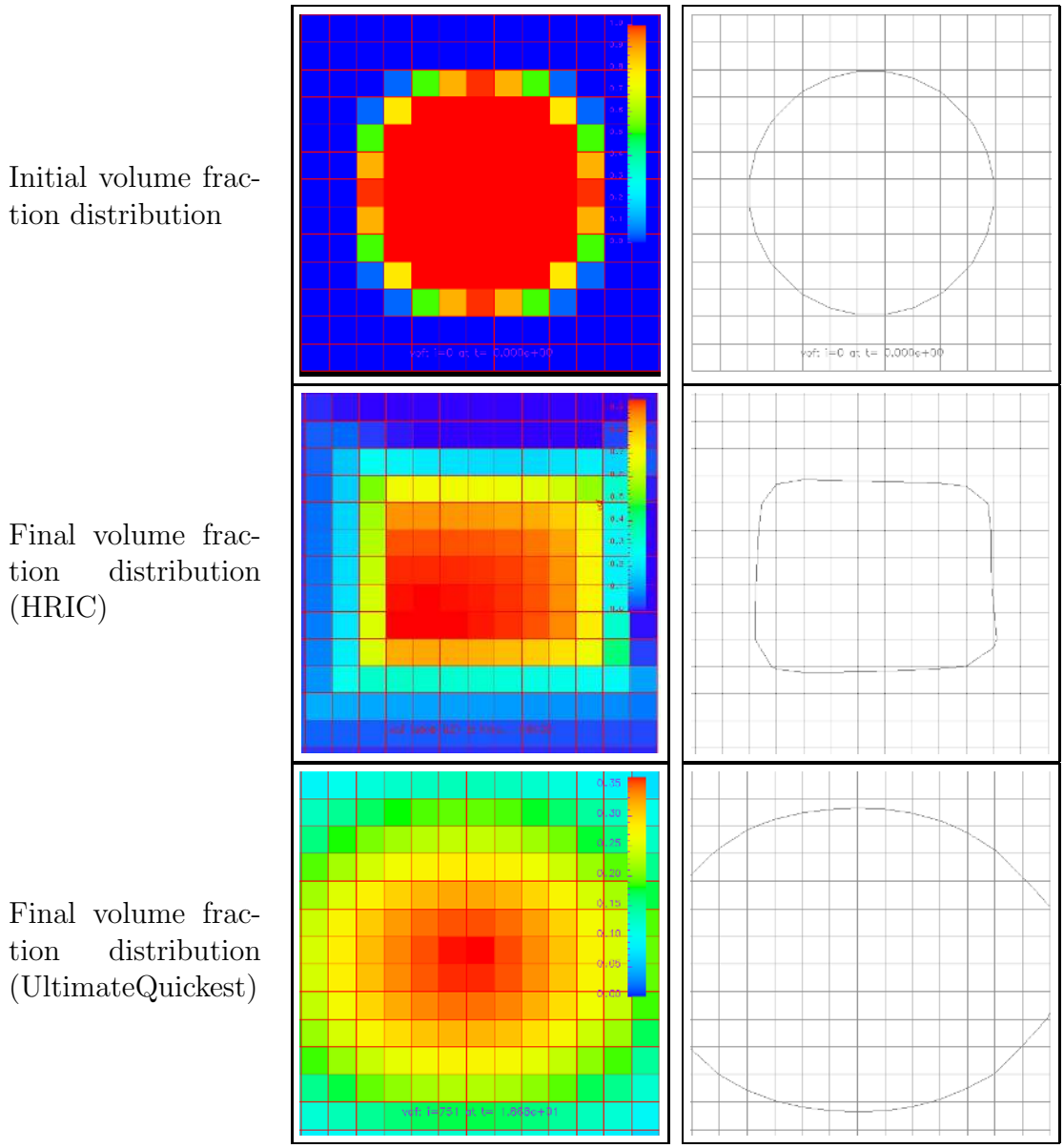

Figure 3.8: *Initial and final volume fraction fields for convection test with HRIC and UltimateQuickest schemes. Colour field representation of the volume fraction α shown left, and isoline (with the isoline value $\alpha = 0.5$) shown right.* ($C_D = 0.15$).

Chapter 4

Initial Numerical Tests

Results from the NS3 code have previously been published, (Mayer *et al.* (1998) and Kawamura (1998)) where a surface tracking scheme, using an adaptive mesh at the free surface boundary, was applied. However, the free surface capturing scheme, on the basis of the CICSAM-VOF method, has not been implemented until recently, and to test the robustness and accuracy of the numerical scheme two simple test cases have been set up. The first test is a dam break problem and the second test is a cylinder impact case. Further, the dam break flow have in some publications (Buchner, 1995a; Mizoguchi, 1989) been used as a description of the deck flow during green water incidents and is therefore also of interest here.

4.1 Dam Break Problem

The dam break problem is a classical mathematical problem, which was first introduced by Stoker (1957). The problem consists of having an enclosed space filled with water. The barrier to one side is then removed and the water can freely flow into the void.

The dam break problem was investigated experimentally by Zhou *et al.* (1999). The experiments setup is shown in Fig. 4.1, with an initial water height (h) behind the flap equal to 600 mm, in a tank 1 m in width. The test was initiated when the flap was lifted, and the water could freely flow into the void, and impact on the wall on the right side of the tank. The flow kinematics were measured during the experiments, by use of two water height probes (H1 and H2), located 2725 mm and 2228 mm from the left end of the tank, respectively, and a pressure gauge (P2) which was mounted on the right wall of the tank, with the centre of the gauge placed 160 mm from the bottom of the tank and with a gauge diameter of 90 mm.

In Colicchio *et al.* (2001) a comparison between the same experimental results and three different numerical methods was presented. The three schemes applied were: A boundary

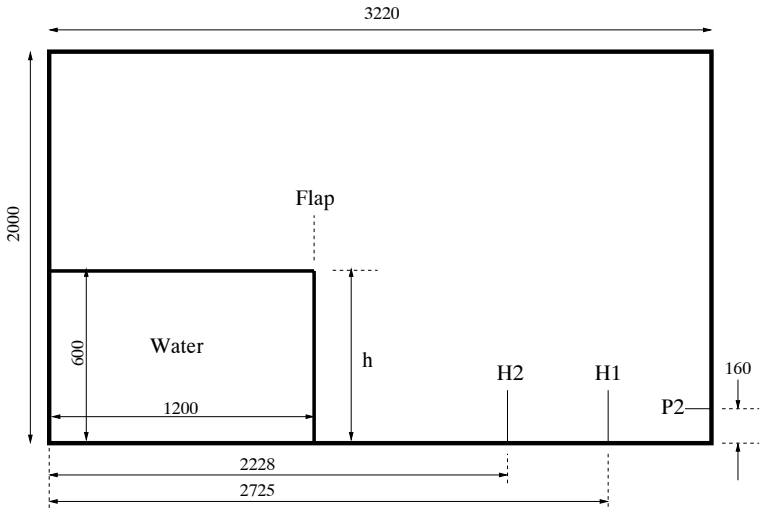

Figure 4.1: *Sketch of dam break problem ([mm]).*

element method, a level set method and the smooth particle hydrodynamics method. These numerical methods showed good agreement with the experiments for the main part of the simulation and the numerical results will also be compared to the present simulation in Section 4.1.3.

4.1.1 Numerical Setup for Dam Break Problem

The present computation of the dam break problem is performed by means of a two-dimensional rectangular grid, 3220 mm long, and 2000 mm high. Although three dimensional effects cannot be fully eliminated the experiment is ideally a two-dimensional problem, and a two-dimensional simulation is a reasonable simplification.

The grid consists of a single block, and in order to investigate the grid sensitivity of the problem three different resolutions are applied, i.e. 128×128, 192×192 and 256×256 grid cells. For the initial conditions the volume fraction field in the fluid domain is given a filled value ($\alpha = 1$) in a region of 1200×600 mm, in the lower left corner of the domain corresponding to the experimental setup. The initial velocity field is set to zero, and wall boundary conditions where pressure gradient and velocities are set equal to zero are applied to all boundaries. The CFL number criterion is equal to 0.2 and viscous computations are performed.

Fig. 4.2 is a visualisation of the dam break problem, using the 256×256 grid. It shows the collapse of the water dam and the impact of the water on the opposite wall, resulting in an overturning wave at the wall. The flow is smooth and with a simple interface until the wave encounters the opposite wall where an overturning wave is formed (step (4)). The last two images where $t\sqrt{g/h} > 6$ shows a more chaotic flow with water separation and overturning waves.

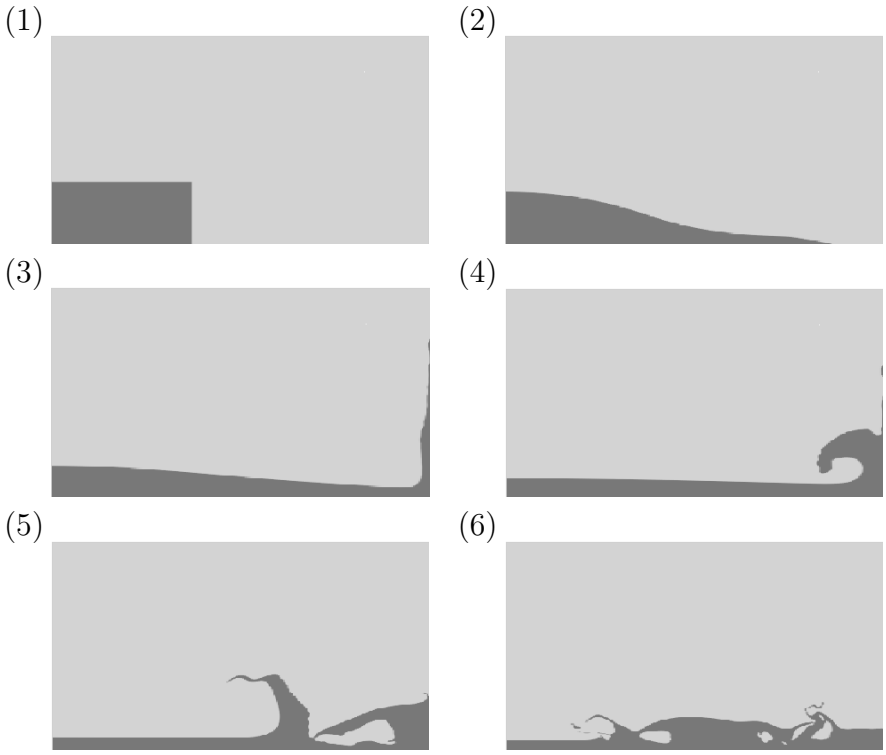

Figure 4.2: *Visualisation of dam break problem computation (*256×256*). The time step between the frames corresponds to* $\Delta\ (t\sqrt{g/h}) = 2$.

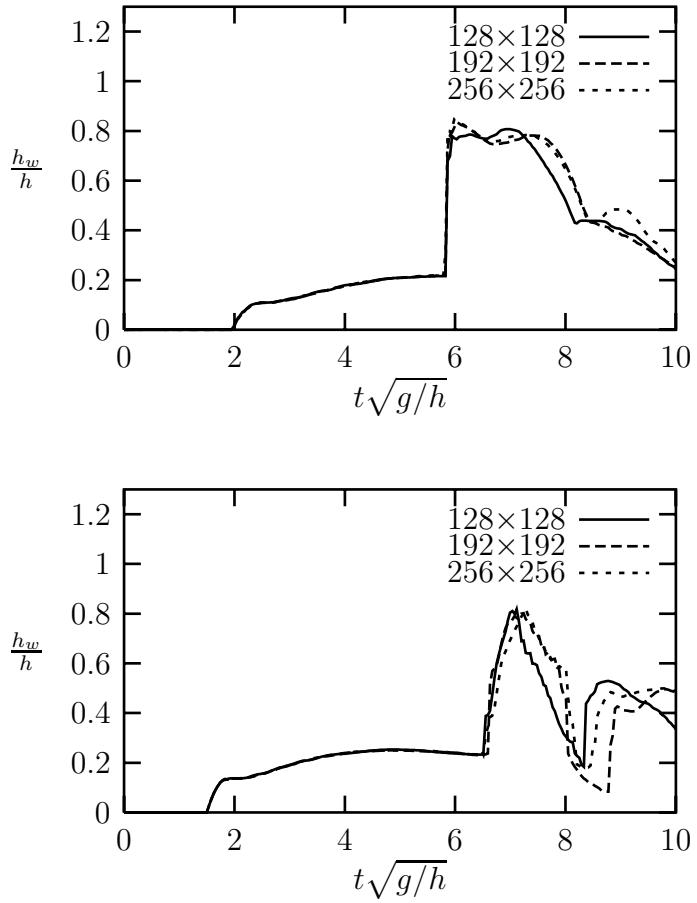

Figure 4.3: *Dam break problem, water height at probes H1 (top) and H2 (below).*

In Fig. 4.3 the time series of the water heights in locations H1 and H2 are shown for the three grids. The water height at the probe rises slowly when the water front first encounters the probe. Then a sudden rise in water height is observed for both probes ($t\sqrt{g/h} \simeq 6$) when the water, which is reflected at the wall, returns and encounters the probe again. The probe H1 registers this second rise first since it is nearest to the wall. The grids give identical results until $t\sqrt{g/h} = 6$, after which the two highest resolution grids still give almost identical results. When $t\sqrt{g/h} > 8$ the two high resolution grids begin to diverge. The divergence between the grids begins when the flow, as shown in the visualisations, begins to show chaotic behaviour. Fig. 4.4 depicts the pressure time history of the pressure probe P2 for the three grids. The pressure probe has a diameter of 90 mm, and the pressure at the centre of the probe (vertical distance from tank bottom equal to 160 mm) and at the bottom of the probe (vertical distance from tank bottom equal to 115 mm) is shown in the figure. The pressure shows a continuous rise in the first phase, starting from the first impact. It then shows a significant first peak, resulting from the water running back down from the tank side, along which it was initially pushed up. A small second peak is also observed, resulting from an overturning wave generated at the tank side. The divergence

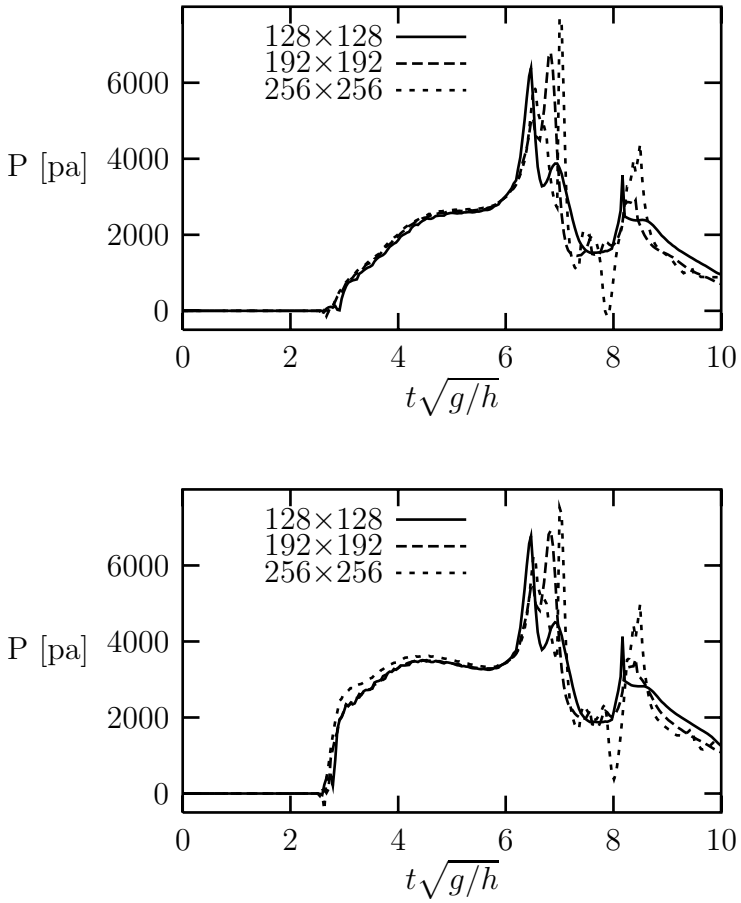

Figure 4.4: *Pressure at the centre of the probe (top) and at the bottom of the probe (below) for the dam break problem. Results obtained with three different grids are compared (number of grid cell are* 128×128*,* 192×192 *and* 256×256*, respectively).*

between the results obtained by use of the different grids begins when $6 < t\sqrt{g/h} < 8$, equal to the period when the flow breaks up and becomes more chaotic. To investigate the sensitivity of the computed results with respect to very small changes in initial conditions a sensitivity test is conducted. In this test a very small velocity component is initially imposed in the computational domain, with magnitude of $\boldsymbol{u}_{\text{init}} = \{0.002, 0.00\}$. The water heights at probes H1 and H2 from this test are shown in Fig. 4.5, where results obtained both with and without the initial perturbation are presented. The figure shows that the initial perturbation has an influence on the resulting water height, but not until after $t\sqrt{g/h} > 6$, which is the time where the water returns from the impact with the wall on the right side of the tank. This part of the flow is very chaotic, and the results here show that the flow in this stage is influenced by a small change in initial conditions. The pressure at probe P2, compared for the cases with and without initial perturbation is shown in Fig. 4.6. This figure also shows a difference in the results obtained with the initial perturbation, compared to the normal results. The difference between the two results is most apparent for the pressure

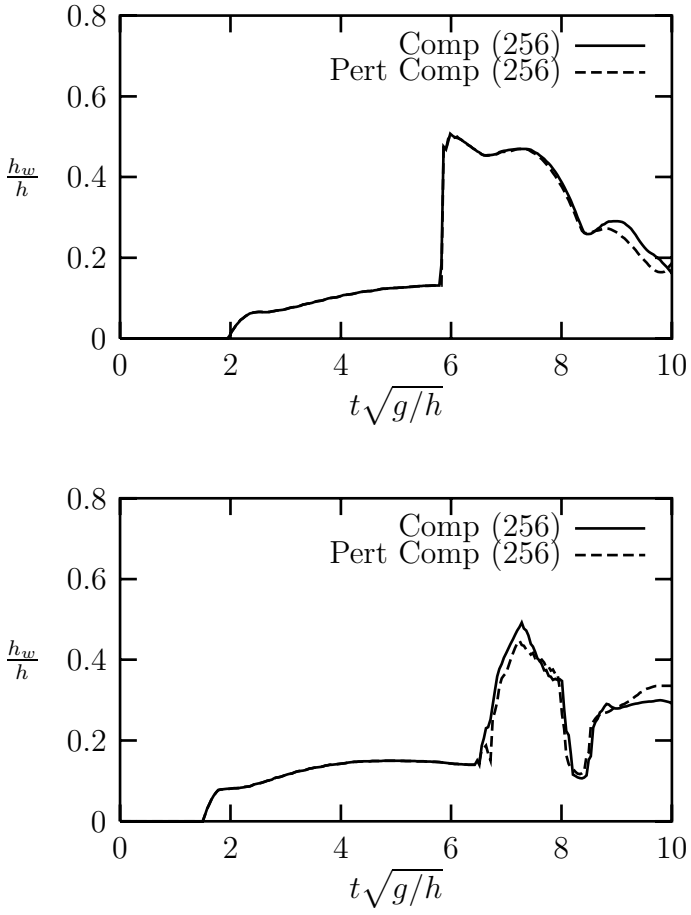

Figure 4.5: *Water height at probes H1 (top) and H2 (bottom), compared for two computations, both by use of the* 256×256 *grid. The full line is from standard computations, the dashed line is from perturbated computations, where a small velocity* $\boldsymbol{u}_{\text{init}} = \{0.002, 0.00\}$ *is added initially in the domain.*

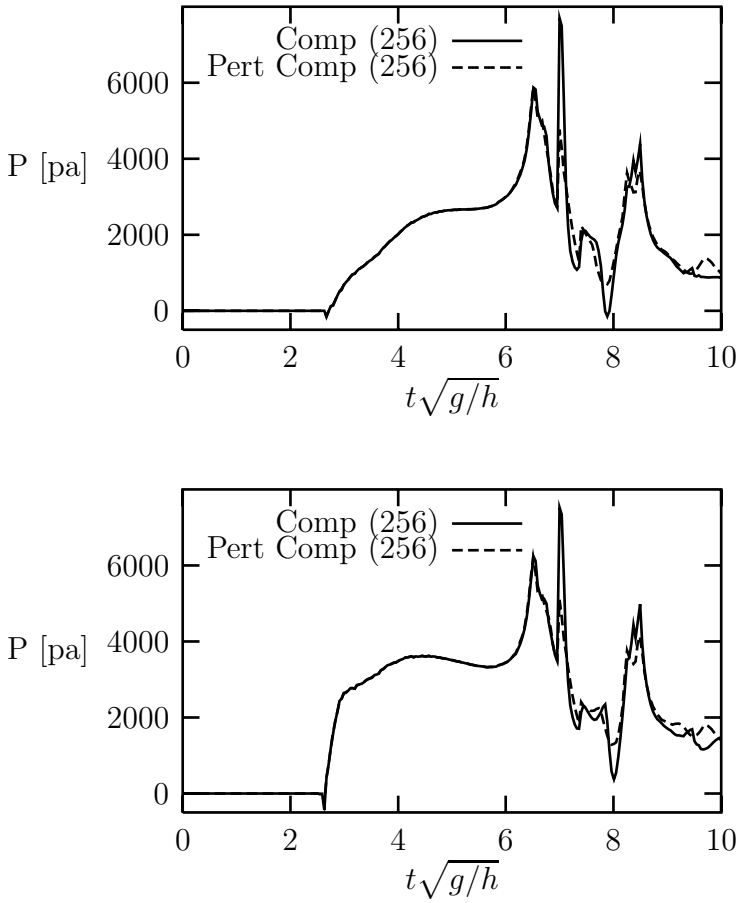

Figure 4.6: *Pressure at centre of probe P2 (top) and at the bottom of probe P2 (bottom), compared for two computations, both by use of the* 256×256 *grid. The full line is from normal computations, the dashed line is from perturbated computations, where a small velocity* $\boldsymbol{u}_{\text{init}} = \{0.002, 0.00\}$ *is added initially in the domain.*

peaks, where the perturbated results gives smaller peaks than the nonperturbated results, but the overall pressure level is similar for the two tests. This documents that the problem is sensitive to the very small initial perturbations in the computational domain. However, compared to the results obatined with the three different grids (see Figs. 4.3 and 4.4) the magnitude of deviation from the perturbated results are smaller than between computations and experiments. This does not necessarily demonstrate that the results obtained with the three different grids are not influenced by changes in initial conditions, but more likely that the perturbations resulting from changing the grid is larger than the perturbations used in the sensitivity test. The change in grid resolution results in a change in truncation errors, which at each timestep is smaller than the perturbation from the sensitivity test, but this truncation error is accumulated throughout the computations, and could result in a larger total perturbation.

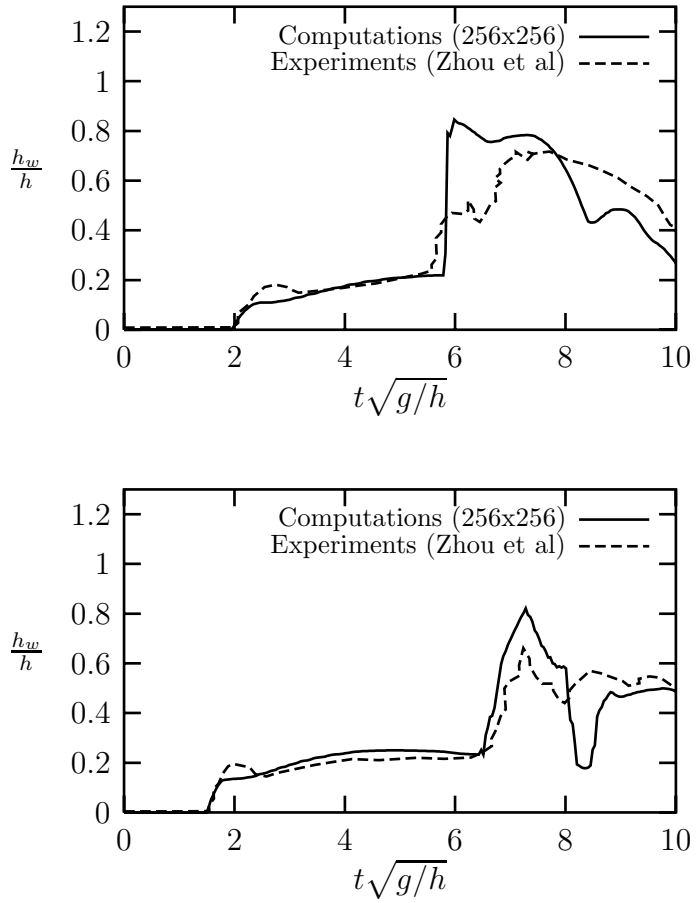

Figure 4.7: *Dam break problem, water height for probes H1 (top) and H2 (below). Comparison between computations and experiments.*

4.1.2 Comparison Between Numerical and Experimental Results

A comparison between numerical and experimental results for the water height probes H1 and H2 is given in Fig. 4.7. In the numerical results the grid with 256×256 grid cells is used. The figure shows good correspondence between numerical and experimental results at the initial stage of the test. However, when the water height increases after the water returns from the impact with the wall, the computed water height is significantly higher than the experimental result, especially for the H1 probe which is the probe nearest to the wall. After a short period the water height in the computations for both probes decreases rapidly and drops to a level below the experimental results.

In Fig. 4.8 a comparison between numerical and experimental results for the pressure probe P2 is given. The top graph shows the pressure time history where the computed pressure is measured at the centre of the probe. The computed pressure rises slower than the experimental one, but the two results approach the same value before a large peak is observed in both computation and experiment. After this peak the computed pressure drops rapidly

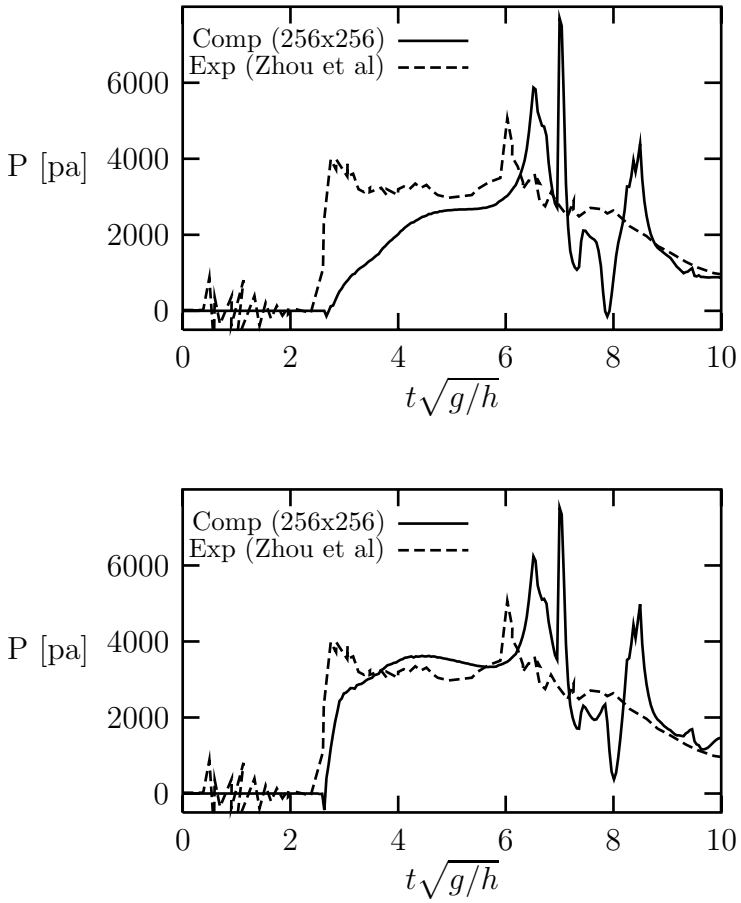

Figure 4.8: *Dam break problem, pressure at the centre of P2 (top) and at the bottom of the probe (below). Comparison between computations and experiments.*

and experiences a second peak, which is not seen in the experiments. In the bottom graph of Fig. 4.8, the computed pressure is taken in the location at the bottom of the pressure transducer. Here the correspondence at the initial stage of the water impact shows better agreement, but after the first peak the results are similar to the results measured at the centre of the probe.

4.1.3 Comparison Between Different Numerical Methods

In Colicchio *et al.* (2001) a comparative study of the dam break problem was presented using three different numerical methods, with the same set-up of the dam break problem as the present simulation. The three methods applied were: a boundary element method (BEM), a level set method (LSM) and a smooth particle hydrodynamics method (SPH). Details of the three methods can be found in Greco (2001), Colicchio *et al.* (2001) and Colagrossi *et al.* (2001), respectively. Comparison of the present results and results obtained by use of the

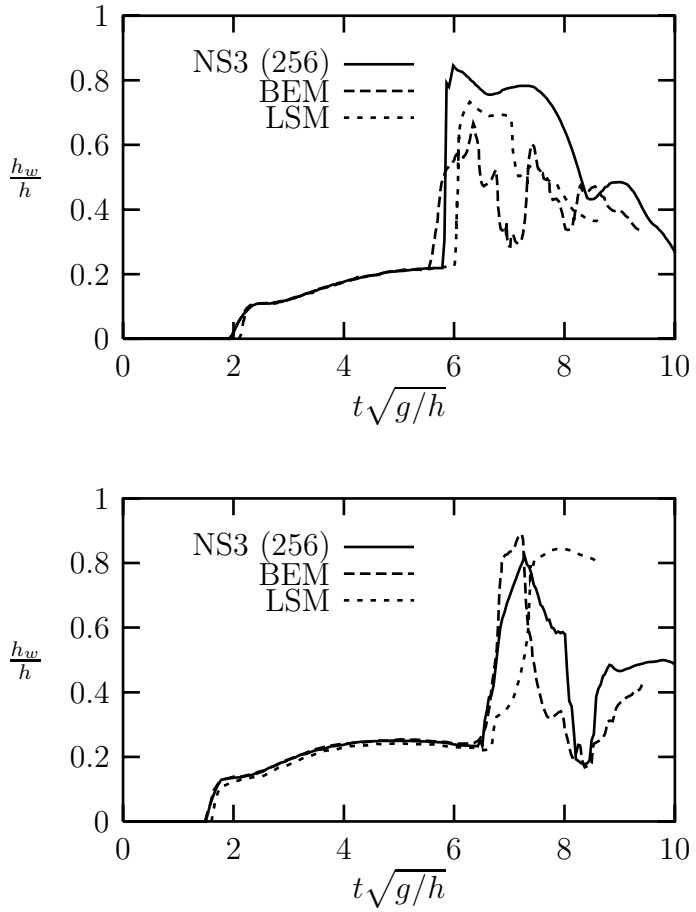

Figure 4.9: *Dam break problem, Water height at probes H1 (top) and H2 (bottom). Comparison between different numerical methods: NS3 (present VOF model,* 256×256 *grid cells), BEM (Boundary Element Method) and LSM (Level Set Method)*

three additional methods are for the water height shown in Fig. 4.9[1] and for pressure shown in Fig. 4.10[2]. From these figures it is clear that the different numerical methods gives very similar results in the initial stage, but in the stage after the water flow returns from the impact with the opposite wall, the different numerical results begins to diverge. This further documents that the dam break problem after the water encounters the opposite wall is very sensitive to initial conditions. Based on the present comparison it is not possible to conclude which method prevails, but it is noteworthy that all the methods gives almost identical result while $t\sqrt{g/h} < 6$.

[1]Waterheight results from the SPH computations not available.

[2]Pressure time series from the BEM computations not available for $t\sqrt{g/h} > 6$.

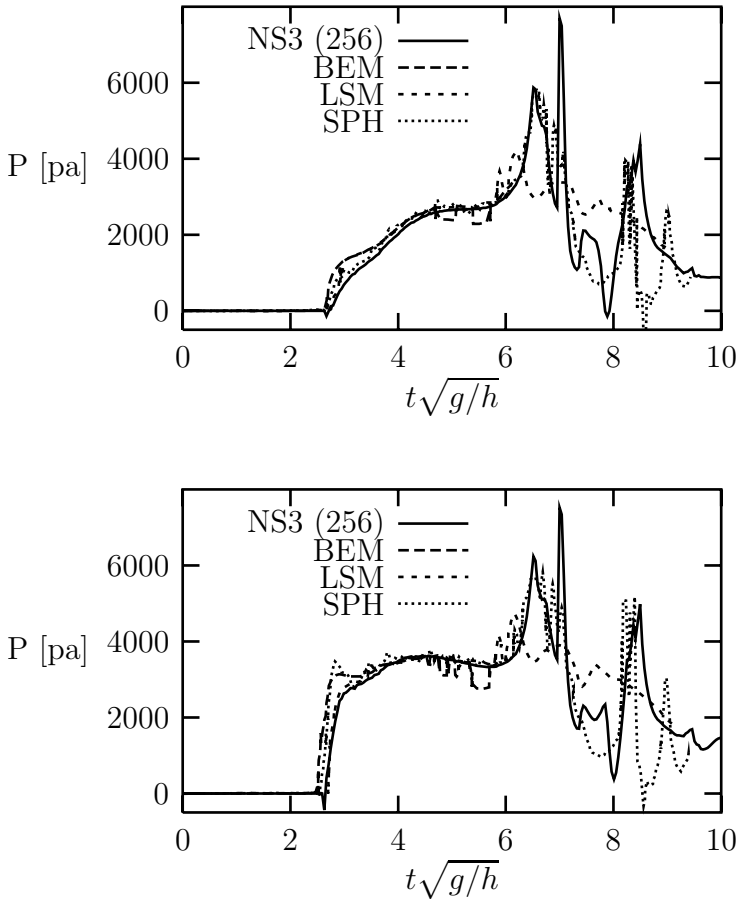

Figure 4.10: *Dam break problem, pressure at the centre of P2 (top) and at the bottom of the probe (below). Comparison between different numerical methods: NS3 (present VOF model,* 256×256 *grid cells), BEM (Boundary Element Method), LSM (Level Set Method) and SPH (Smooth Partical Hydrodynamics).*

4.1.4 Discussion of Dam Break Results

The grid resolution tests showed that although all three grids gave similiar results, the grid convergence was not fully monotonic. This can be due to the discretisation of the free surface. Even though the resolution is high the VOF method is limited in the sense that each grid cell can only contain a single fluid interface. Thus, when the free surface is very distorted, with overturning waves and water spray, a small change in grid resolution may not capture the free surface in the exact same manner.

Although the numerical and experimental results shows similar flow features, the correspondence between them is not exact. However, in the experiments (Zhou *et al.*, 1999) it was reported that they were not fully reproducible and that very small changes in the initial conditions can be clearly seen in the results. This supports that the chaotic behaviour seen after $t\sqrt{g/h} > 6$ makes the flow very sensitive to initial conditions and difficult to reproduce

numerically. Applying only two dimensional simulation can also influence the results, since the flow at some point will break up into three dimensional behaviour.

In Colicchio *et al.* (2001) three different numerical methods are applied to the same problem, and the same magnitude of difference between computational and experimental results is seen as in the current results. The differences also occur after $t\sqrt{g/h} > 6$, and this supports the assumption, that these experiments are difficult to exactly reproduce due to the high sensitivity of initial conditions.

4.2 Cylinder Impact

In design of marine and offshore structures, wave induced loads is a very important factor, especially in harsh environments like the north sea. Elements not constantly in water, like transverse stiffeners on jackup rigs, or offshore platform deck elements, can experience impact of wave crests, and for design purposes an accurate prediction of this wave load is important. The second test case for the NS3 code is a cylinder impact case, where a cylinder is forced with constant velocity into a water surface initially at rest. This test is somewhat similar to a jacket structure stiffener in the free surface zone, coming in and out of the water due to wave motion.

4.2.1 Experimental Setup

Faltinsen *et al.* (1977) performed experimental tests with cylinder impact, using an aluminium cylinder with a diameter $d = 0.35\ m$ and a length $L = 0.40\ m$. The cylinder is with constant velocity (V) forced onto a water surface initially at rest by use of a hydraulic ram. The test series include two different impact velocities: $V = 0.9\ m/s$ and $V = 1.35\ m/s$. The cylinders were equipped with end plates in order to minimise three dimensional effects at the ends of the tube. The test setup is shown in Fig. 4.11 where S indicate level of submergence ad R is cylinder radius, from which the submergence rate $\frac{S}{R}$ can be defined.

4.2.2 Numerical Setup

In the numerical simulation the grid is steady in time and the water is instead given a velocity from an inlet boundary, in order to model the relative motion between cylinder and water. The computational domain is rectangular and consists of four blocks, set up in an H-type grid, each with one face on the cylinder surface. In addition to these, a fifth block is located as a buffer between the input boundary and the domain near the cylinder. Fig. 4.12 shows a sketch of the numerical domain, where N_t and N_r are the number of grid cells in the tangential and the radial direction, respectively. In the computations four different grid

Table 4.1: *Boundary conditions for cylinder impact.*

	$\bar{p}$	$\bar{u}_i$
inflow	$\frac{\partial \bar{p}}{\partial n} = 0$	$\begin{cases} \bar{u}_1 = 0 \\ \bar{u}_2 = u_{\text{inflow}} \end{cases}$
outflow	$\bar{p} = 0$	$\frac{\partial \bar{u}_i}{\partial n} = 0$
body surface	$\frac{\partial \bar{p}}{\partial n} = 0$	$\bar{u}_i = 0$
symmetry plane	$\frac{\partial \bar{p}}{\partial n} = 0$	$\begin{cases} \frac{\partial \bar{u}_2}{\partial n} = 0 \\ \bar{u}_1 = 0 \end{cases}$

resolutions are applied, where the number of grid cells in each of the four blocks equals ($N_t \times N_r$): 64×64, 96×96, 128×128 and 128×256. The three first grids are slightly stretched in the radial direction in order to achieve higher grid density near the cylinder surface. The last grid is highly stretched by use of a stretch factor of 200, which gives a very fine grid near the cylinder. The boundary conditions are listed in Table 4.2.2, and the in- and outflow boundaries are shown in Fig. 4.12, the east and west exterior boundaries are symmetry boundaries and the cylinder surface is a body surface boundary. The viscosity is set to $10^{-6}\ \frac{\text{m}^2}{\text{s}}$ and the CFL number for all computations equals 0.25.

4.2.3 Visualisation of Cylinder Impact

In Fig. 4.13 visualisations of the free surface contours are shown for the impact velocity equal to 0.9 m/s using the VOF field captured during the computations. Results for three different grid resolutions are given, showing how a water jet is forced from below the cylinder and up along the cylinder, then a wave is formed from this jet, which travels away from the cylinder. The figure clearly illustrates how the jet is attached to the cylinder for the two lowest resolution cases (96×96 and 128×128), but that it separates from the cylinder

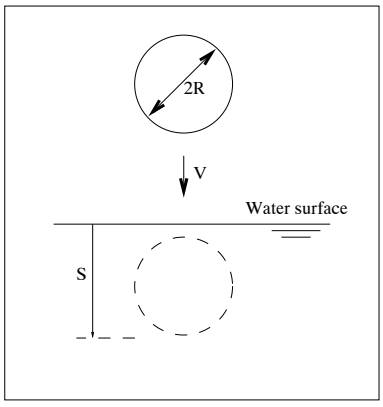

Figure 4.11: *Sketch of cylinder impact problem.*

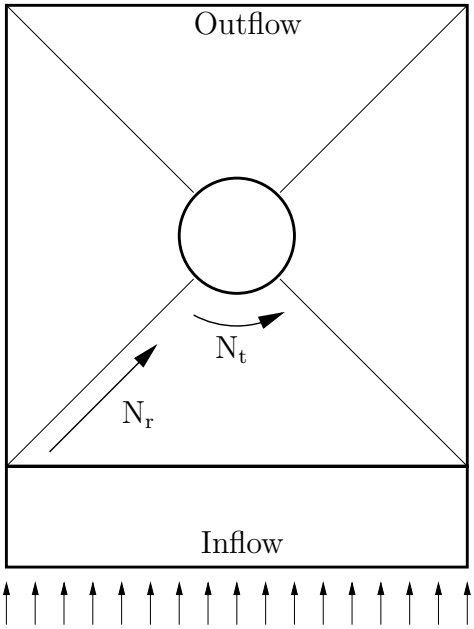

Figure 4.12: *Sketch of numerical domain for cylinder impact.*

when the highest grid resolution is applied. Description of the flow physics during the experiments (Faltinsen *et al.*, 1977) showed that the water did separate from the cylinder, which was expected to occur prior to the computations. The same computations were conducted with an increased diffusion coefficient, in order to investigate its effect on the flow separation problem. These results showed that if the coefficient was increased with at least 10 orders of magnitude, the flow separated in all the cases, even the low resolution cases. The computations were also made for an impact velocity of 1.35 m/s, which gives very similar results, including the water jet separation.

4.2.4 Computed Results of Cylinder Impact

The computed vertical load on the cylinder during submergence is shown in Fig. 4.14. The results are obtained by use of four different grids, with increasing resolution. The figure shows how the impact induces a high load on the cylinder, which initially decays while the cylinder submerges until $S/R \simeq 0.5$, after which the cylinder load starts to increase. The difference between the four computed results is very small, and only at the very early impact stage is it possible to observe any effect of increasing the resolution. Eventhough the flow physics is different, i.e. only for the fineste resolved case the flow separates from the cylinder, the impact load is still very similar for all four grids. This can be contributed to the fact that the vertical composant of the pressure at the cylinder surface in this region is very small. Further, the figure shows some fluctuations in the initial stage of the impact. This is not a physical property, but a result of a small numerical instability, and these fluctuations are not large compared to the total load.

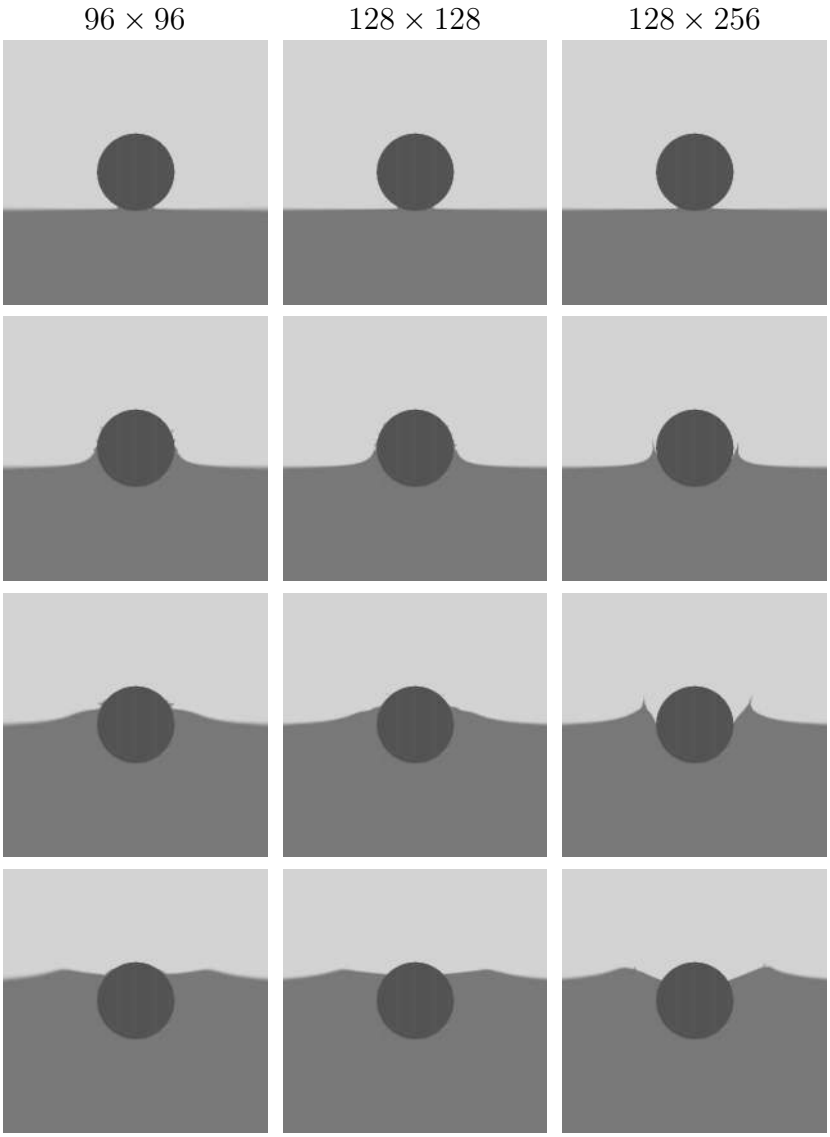

Figure 4.13: *Visualisation of computed cylinder impact (V = 0.9 m/s)*

4.2.5 Comparison of Computational and Experimental Results for Cylinder Impact

The water induced load on the cylinder is shown in Fig. 4.15, comparing computed and experimental results for the impact velocity V = 0.9 m/s. The figure shows both the total vertical load and the dynamic pressure load, where the boyancy contribution is subtracted from the total load. The boyancy contribution is computed from the nominal submergence, even though the actual submergence in some cases differ from the nominal submergence, and

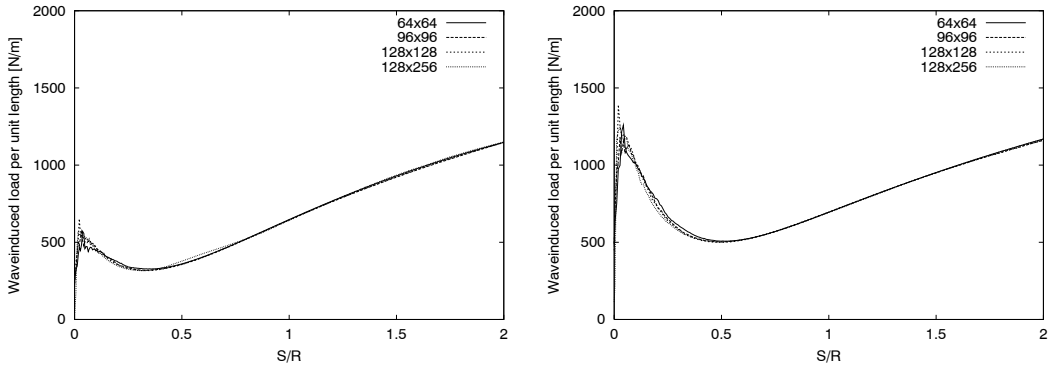

Figure 4.14: *Computed loads on cylinder per unit length as a function of submergence, $V = 0.9$ m/s (left) and $V = 1.35$ m/s (right). Shown using four different grids:* 64×64, 96×96, 128×128 *and* 128×256.

is defined as

$$F_b(S) = \frac{\rho g R^2}{2}\left(2\arccos\left(1-\frac{S}{R}\right) - \sin\left(1-\frac{S}{R}\right)\right), \tag{4.1}$$

where ρ is mass desity of water and g is gravitational acceleration. In the first stage of the impact the water will run up along the cylinder and the actual submergence is larger than the nominal, and in the last stage, a wave is travelling away from the cylinder and the top is not wetted, though the cylinder is nominally fully submerged.

For the total load Fig. 4.15 shows, especially in the initial impact stage, that the computations and experiments agree well. However, when the boyancy contribution is subtracted the experimental results shows a neglible amount of dynamic pressure load, while the computational result show some dynamic pressure load. The cylinder is forced with a constant velocity, with a Reynolds number of $Re \simeq 3.15 \cdot 10^5$, which is expected to at least give some dynamic pressure load contriburion. The lack of dynamic pressure load in the experiments can be caused by either that the boyancy contribution might be overestimated as perviously explained or by measuring inaccuracies during the experiments. In the experiments (Faltinsen *et al.*, 1977) it was reported that at least a $\pm 10\%$ inacurracy on the results must be expected.

The results from the case with velocity V = 1.35 m/s is shown in Fig. 4.16. As in the previous case the results are shown both with total vertical load and with the boyancy contribution subtracted from the total load. The agreement between computed and experimental total load is better in this case, where very little difference is noticed between computations and experiments. The comparison without boyancy contribution also shows a better agreement. Here the experimental results shows some dynamic pressure contribution, opposite of what is seen in the previous case.

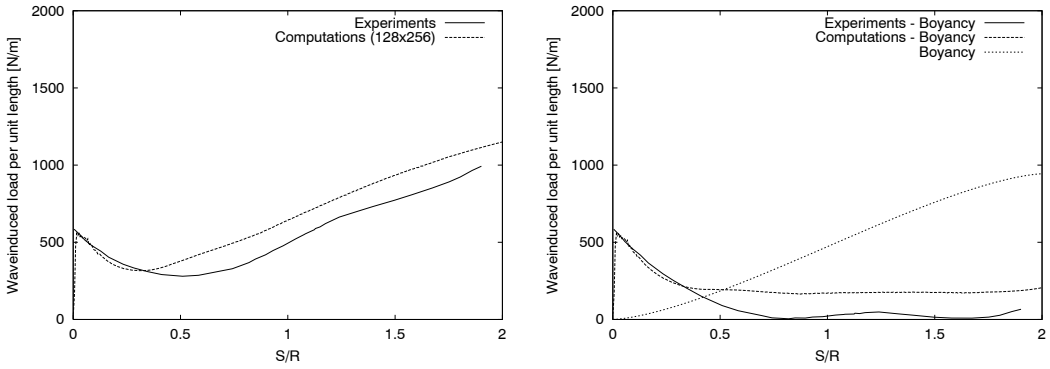

Figure 4.15: *Computed and experimental (from Faltinsen* et al. *(1977)) loads on cylinder per unit length as a function of submergence at $V = 0.9$ m/s. Left figure shows the total loads and in the right figure the boyancy contribution is subtracted from the total load.*

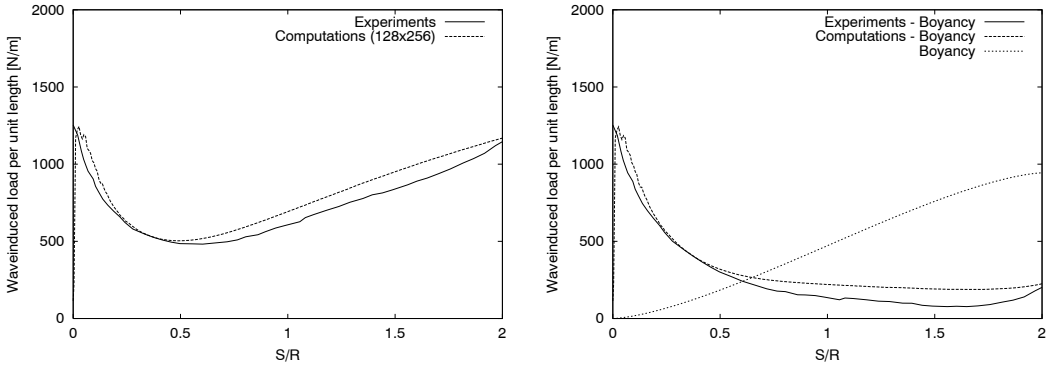

Figure 4.16: *Computed (128×256) and experimental (from Faltinsen* et al. *(1977)) loads on cylinder per unit length as a function of submergence at $V = 1.35$ m/s. Left figure shows the total loads and in the right figure the boyancy contribution is subtracted from the total load.*

4.2.6 Discussion of Cylinder Impact Results

The visualisation of the computed cylinder impact clearly shows that the cases with the lowest grid resolution cannot predict the separation of the water jet from the cylinder. When the water flow attaches to the cylinder and no separation occurs, the solution is similar to a potential flow solution. However, the high grid resolution case predicted separation, which was also reported in the experiments. From this it can be concluded that the diffusion is not modelled correctly in the low resolution cases. This is supported by the fact that when other numerical tests were conducted where artificially high diffusion was added the flow did separate. Despite this difference in modelling the water jet, the resulting load on the cylinder is remarkably similar in the different grids, which means that the flow in the region of separation has very small influence on the overall load. The agreement between

computations and experiments is not perfect but the correspondence between experimental and computed results is considered satisfactory.

Chapter 5

Simulation of Tank Sloshing

For ships carrying liquid cargo sloshing can be critical in a partially filled tank, from a structural point of view. The sloshing of the liquid can increase the dynamic pressure on the tank sides and bottom, so that the integrity of the tank is put at risk.

Another sloshing problem occurs for LNG carriers. Though these vessels always sail with either nearly completely full or empty tanks, this might not be the case in the future. Previously, these vessels would always load and offload inside safe harbours, but for security reasons, these vessels might in the future have to load and offload at offshore terminals. Changes in weather conditions might force the load/offload process to be interrupted, leaving the tank partially filled, and the ship motion can then excite the fluid.

In either case, it is essential to be able to evaluate the dynamic load in partially filled tanks. This chapter will address this problem by numerically simulating sloshing and comparing it to experimental data. The experiments were conducted by Hinatsu *et al.* (2001) and were part of a workshop in which also National Maritime Research Institute of Japan (former SRI) and Technical University of Hamburg-Harburg participated (Hinatsu, 2001). Results from this chapter have previously been presented in Nielsen and Mayer (2001).

5.1 Sloshing Problem Setup

The experimental test with tank sloshing (Hinatsu *et al.*, 2001) was performed in a rectangular tank with dimensions of 1200×600×200 mm. The tank was equipped with acrylic end plates in order to visualise the flow inside the tank during the experiments, which were recorded by a video recorder. At various degrees of filling, the tank was accelerated in a horizontal sinusoidal motion, and during the test pressure measurements were performed inside the tank. A sketch of the setup is shown in Fig. 5.1, where the locations of the pressure gauges are indicated.

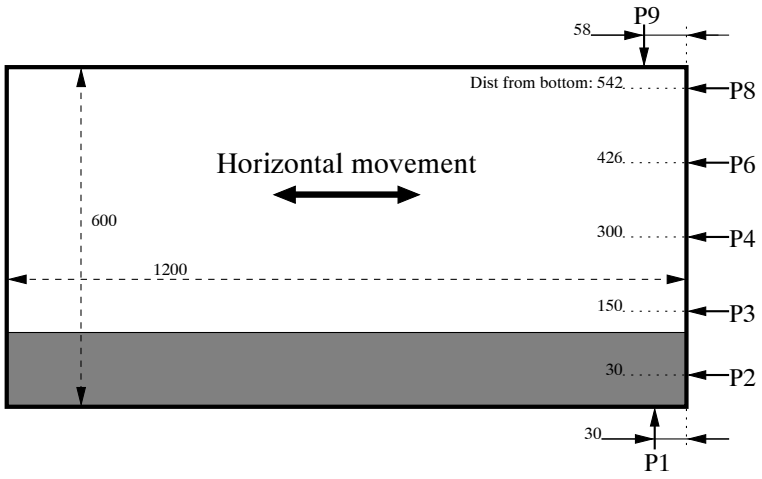

Figure 5.1: *Sloshing tank setup (units [mm]).* **P** *indicates pressure gauge.*

The sloshing experiments were conducted for a wide range of motion amplitudes and periods, and for the present investigation four different cases have been selected for comparison with computations. The cases are outlined in Table 5.1, where water level indicates the filling degree of the tank, period (T) is the period of the horizontal motion of the tank and amplitude (A) is the amplitude of this motion. Case 1 and Case 4 are resonance cases, in which the fluid motion is largest and the pressure measured inside the tank has the highest values.

5.2 Numerical Setup

At the time of these computations it was not possible to apply moving meshes in the NS3 code, and though this feature has since been implemented, the sloshing problem is solved by means of a steady mesh. This requires that the coordinate system for which the computational domain inside the tank is defined has a moving frame of reference. This can be done by adding a momentum source term to all computational cells, so that the magnitude of this source equals the acceleration of the frame of reference. Since the horizontal position of the tank is given by

$$x = A\sin(\omega t), \tag{5.1}$$

	Water level	Period	Amplitude
Case 1	20%	1.74 s	60 mm
Case 2	20%	1.94 s	60 mm
Case 3	60%	1.40 s	15 mm
Case 4	60%	1.47 s	15 mm

Table 5.1: *Outline of sloshing cases.*

where x is the horizontal position and ω equals $\frac{2\pi}{T}$, the acceleration of the coordinate system, and hence the magnitude of the source, can be found by

$$\frac{\partial^2 x}{\partial t^2} = -A\omega^2 \sin(\omega t). \tag{5.2}$$

On all boundaries the wall boundary condition has been used, and the viscosity equals $10^6 \frac{\mathrm{m}^2}{\mathrm{s}}$. For all computations the max CFL number equals 0.2.

5.2.1 Grid Resolution

In order to investigate the grid sensitivity of the sloshing problem, three different meshes are applied, and the resulting pressures inside the tank are compared. This is shown in Fig. 5.2, where the pressure at pressure gauges P1, P2 and P3 are compared between three meshes with a resolution of 96×48, 128×64 and 192×96 grid cells, respectively. The values of period and amplitude of the tank sloshing acceleration are equal to Case 1 in Table 5.1. The figure exhibits a characteristic behaviour as the pressure, at all three gauges, has a periodic pattern with a recurring period equal to the tank movement period. This is caused by a travelling wave being formed inside the tank, and following the movement of the tank out of phase, i.e. when the tank is in the left outer position, the wave impacts the right boundary and vice versa.

During the first sloshing period, all three grids give identical pressures. At this stage the free surface is very smooth, since the fluid inside the tank, which was initially at rest, has only been slightly excited. After the first period, the pressures predicted at the three grids begin to diverge slightly, but the overall profiles of the pressures are still comparable. The figure also shows, for some impacts, a large negative peak for gauges P1 and P2, which is a result of an air bubble formed along the boundary after the travelling wave encounters the end plate. This exposes the pressure gauge, which results in the peak. The bubble is not present for all impacts, and the three grids give different predictions for the time when the bubble appears. However, apart from this bubble the three grids give very similar results. As in the previous chapter, the difference in results is expected to be caused by the method by which the free surface is captured, where each cell only contains a single fluid interface. This may make it difficult to capture a very complex fluid interface when the interface is discretised and each cell only contains a single interface. Moreover the three grids might give different interpretations of the interface, leading to slightly different results.

5.3 Results of Sloshing Computations

During the experimental tests the fluid motion inside the tank was captured using VCR, and Figs. 5.3 and 5.4 present single images from this visualisation captured from the video.

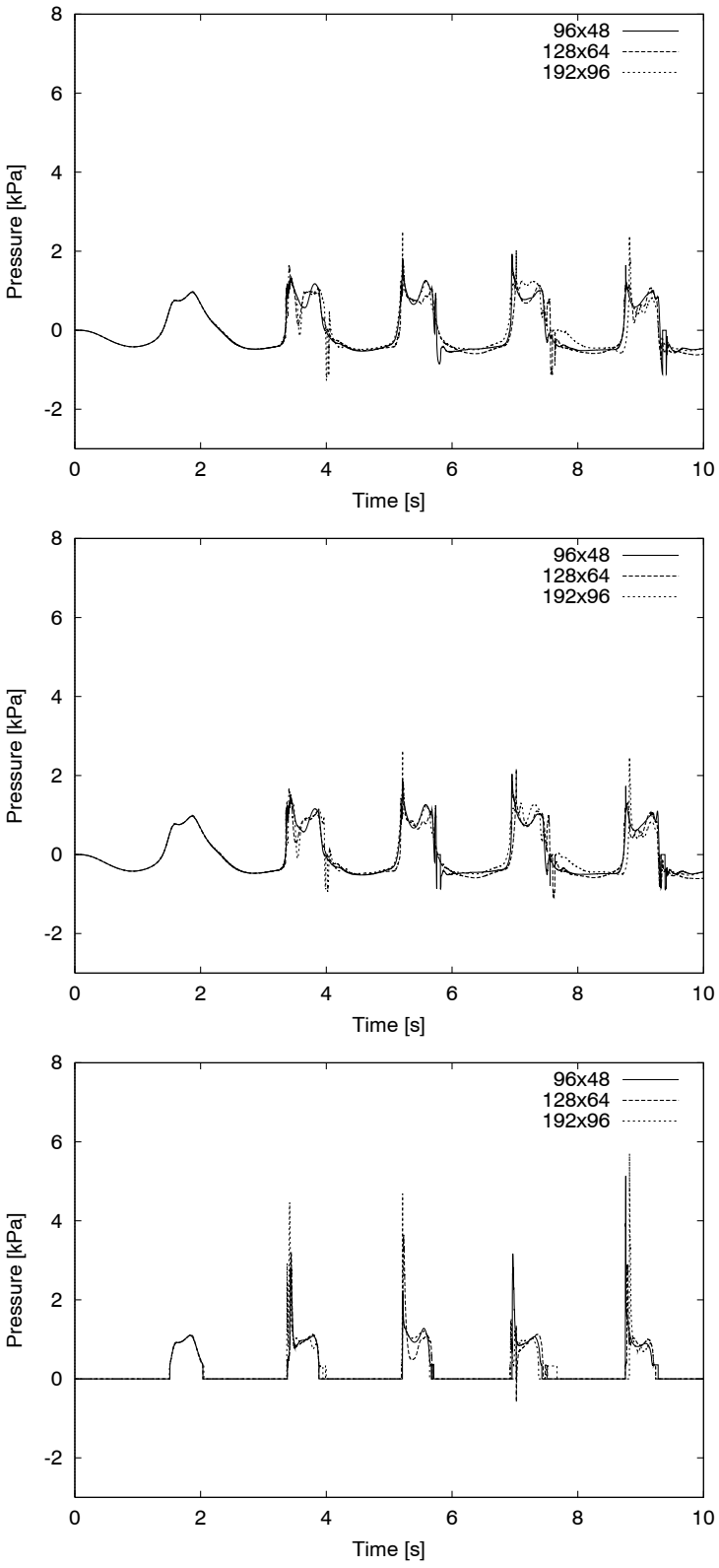

Figure 5.2: *Computations of sloshing problem using three different grids* (96×48, 128×64 *and* 192×96). *The figures show the pressure computed inside the tank at P1 (top), P2 (middle) and P3 (bottom).*

For equivalent time steps, the free surface from the computations has been captured and compared to the experiments. For the following results, the grid with 128×64 grid cells has been used.

5.3.1 Visualisation of the Fluid Motion

Fig. 5.3 presents the comparison for Case 1 at four different time steps with a time gap between the images equal 0.2 s. The first step (top left) clearly shows a travelling wave inside the tank, and the following pictures show the wave impact at the wall at the right side of the tank. A large amount of fluid separation at the free surface resulting from the wall impact is observed, and the last images also show the forming of a new wave, which travels in the opposite direction. By comparison of experiments and computations the dynamics of the flow exhibits great resemblance, as the travelling wave and the impact with the end wall are very similar. The large amount of fluid separation observed in the experiments is not captured in the computations. There may be two causes: First of all the NS3 code cannot resolve an amount of fluid which becomes smaller than a few grid cells, so in order to capture very small amounts of fluid separation flow features, a higher grid resolution is required. However, since this separation is not considered important for the overall flow dynamics, the effect of the fluid separation can be considered negligible. Secondly, some of the separation seen in the figure is a result of fluid which is pushed onto the plexiglas window on the side of the tank, i.e. as a result of threedimensional effects which cannot be captured with the present two-dimensional numerical model.

In Fig. 5.4 the fluid visualisation for Case 4 is shown. In this case the filling degree of the tank is increased to 60% and both period and amplitude are reduced. A travelling wave is also seen here, although it is not as distinct as previously. The impact with the end wall seems larger, due to the increased amount of water, and the fluid hits the top of the tank during each impact.

The travelling wave is best seen in the final image (bottom right of figure), where it moves away from the right wall and travels toward the left side of the tank. As in Case 1, the experiments show some fluid separtion which is not present in the computations, but the separation can also here largely be assigned to threedimensionality, as the water that encounters the tank end and top is pushed onto the plexiglas side of the tank. Still, the main flow features - the impact on the side wall, the travelling wave forming and progressing toward the left tank side and the amount of water that impacts the end and top of the tank - are well predicted by the computations.

5.3.2 Comparison of Pressure

During the experiments pressure measurements were conducted inside the tank in different locations. In Fig. 5.1 the locations of the gauges are indicated and during the computations

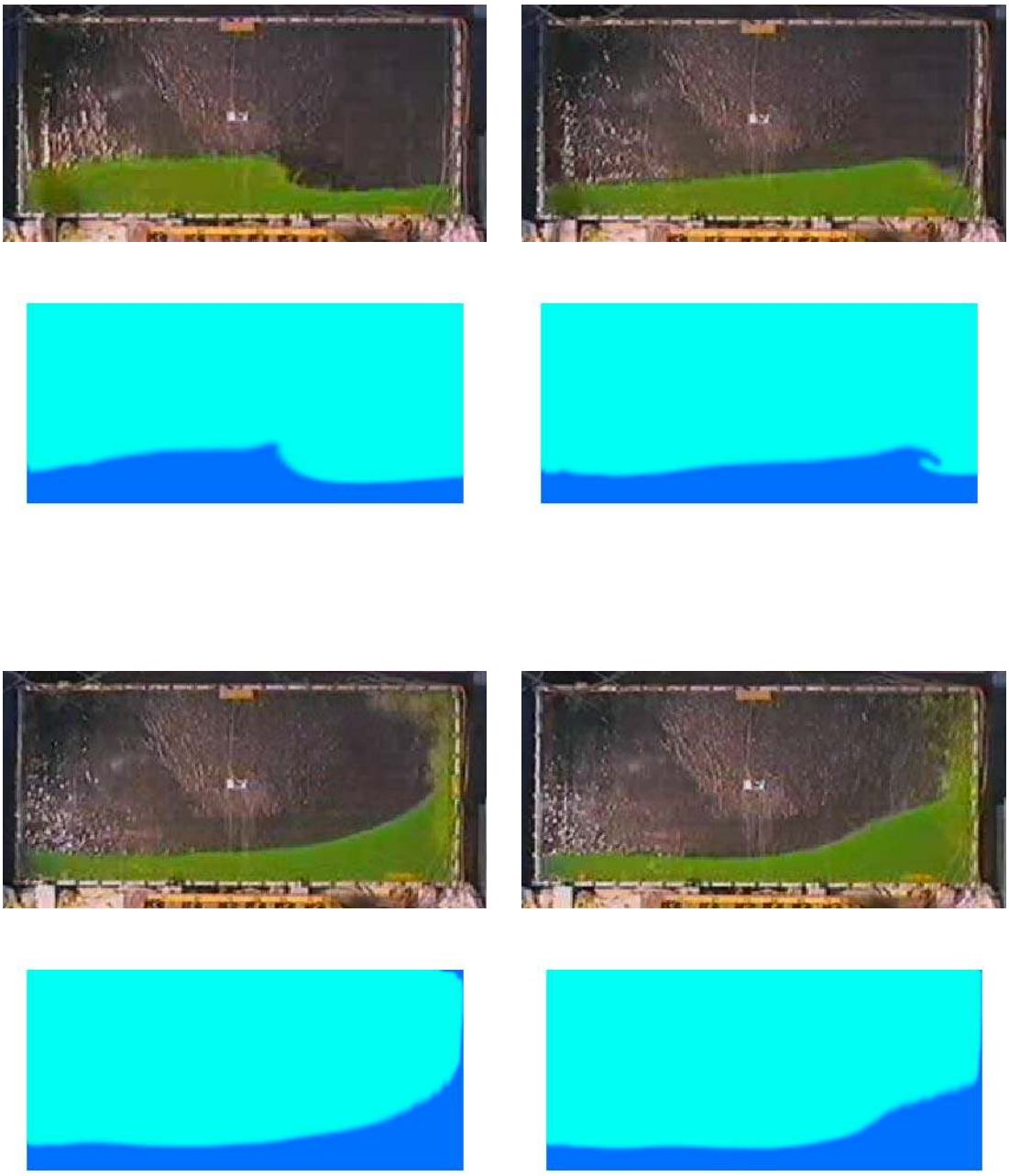

Figure 5.3: *Visualisation of the free surface contours in Case 1, for experiments and computations. Experiments are green and computations are blue.*

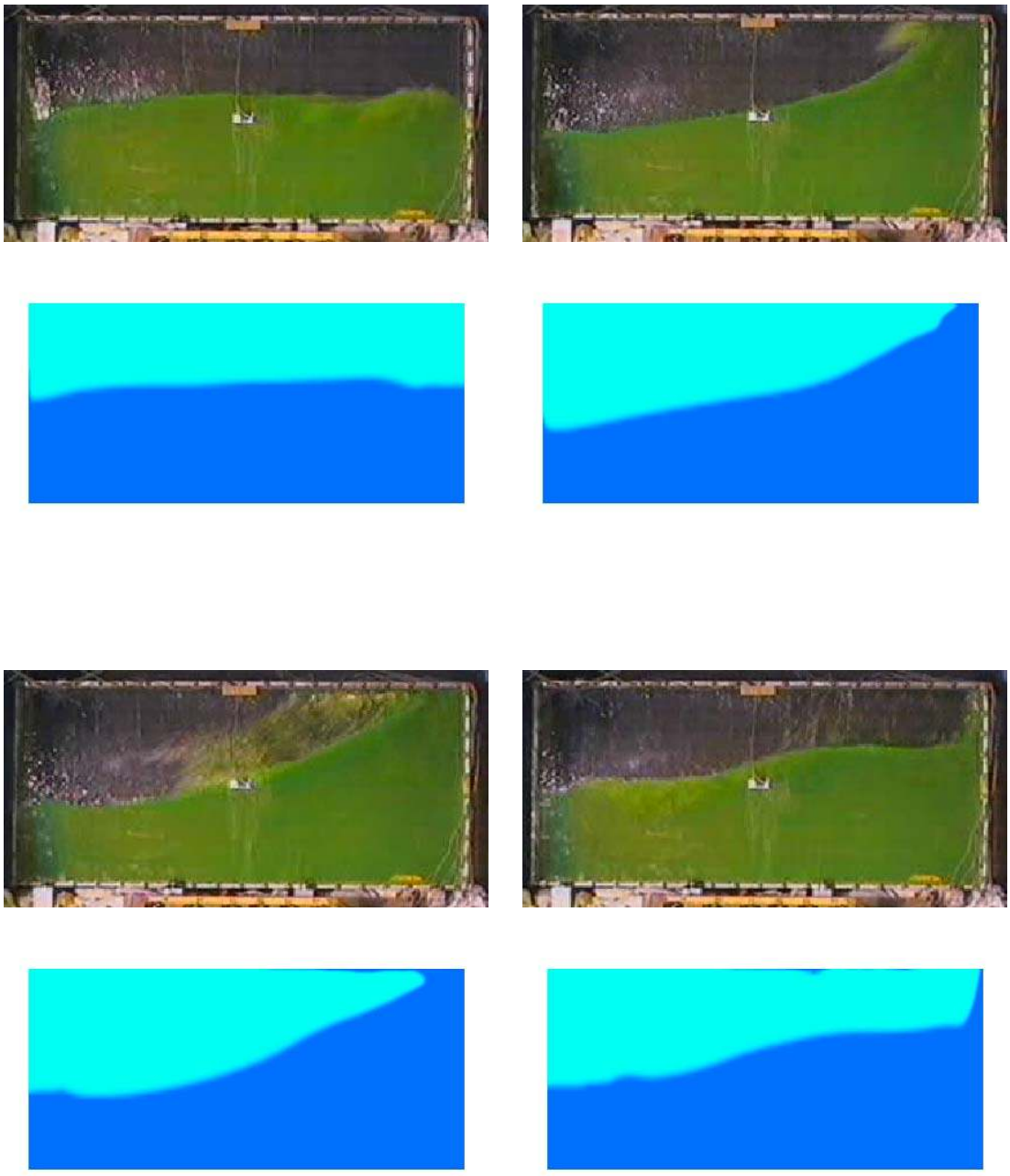

Figure 5.4: *Visualisation of the free surface contours in Case 4, for experiments and computations. Experiments are green and computations are blue.*

the fluid pressure has been recorded in the corresponding locations. Fig. 5.5 presents a comparison for gauges P1, P2 and P3 between numerical and experimental pressure time series. For the computed pressure the first two periods have been removed, because the fluid is not significantly excited. The experimental results were measured after the fluid was fully excited.

Gauge P1 in Fig. 5.5 shows that the computed pressure closely follows the experimental pressure and that the magnitude of each pressure peak, which results from the travelling wave impact with the right end wall, is well predicted. At the end of each impact the computed pressure has a negative peak, which is not seen in the experiments. This peak, as described earlier, is a result of a small void bubble forming at the tank end and the figure shows that it does not appear in the experiments. At the end of the time series a phase lag between experiments and computations is observed, which is caused by dissipation, i.e. loss of mass in the computational domain. The mass dissipation changes the flow properties so that the present period and amplitude no longer give resonance inside the tank, and the fluid motion inside the tank comes out of phase with the tank movement. As described in Chapter 3 this dissipation originates from a cleaning routine, which is enforced at each timestep. Since the amount of fluid separation is large relative to the total amount of fluid in the domain, this dissipation affects the total mass conservation.

For gauge P2 the comparison shows the same result: after each impact the computed pressure drops below the numerical level but quickly returns, and the two pressure profiles exhibit large resemblance. The phase lag observed at the end of the time series is also present for gauge P2. The P3 gauge, which is not initially submerged, has an impact of shorter duration, but the peaks appearing initially for each impact are larger. The experiment shows that each impact is different from the others, and that the peaks have significantly different values from period to period. This is also seen in the computations, though in general the peaks in the computations are not as large as in the experimental case. The phase lag also becomes apparent at the end of the time series.

Fig. 5.6 gives the values of gauges P1, P2 and P3 for Case 2. This case is a nonresonance case, as reported in Hinatsu *et al.* (2001), contrary to Case 1. This means that the fluid motion is less than that observed in Case 1, but Fig. 5.6 proves that the magnitude of the measured pressure is very similar to that of Case 1. The comparison between measured and computed pressure is also similar to case 1, with the characteristic drop in pressure after each impact for both gauges P1 and P2. In the computed results the last period seems to agree better with the experimental results than in Case 1, and the phase lag is not as evident.

The results for the pressure from Case 3, where the tank is 60 % full, are given in Fig. 5.7. Due to the increase in filling degree, gauges located higher in the tank are used for this validation. Gauge P4 (top left graph) exhibit a periodic behaviour, as the pressure peaks each time the travelling wave inside the tank impacts the tank side. The experimental and computed pressures are very close in magnitude, but the computed pressure clearly has a phase lag toward the end of the simulation. As previously this is due to mass dissipation. After each impact the pressure gauge is out of the water, because the water is pushed toward

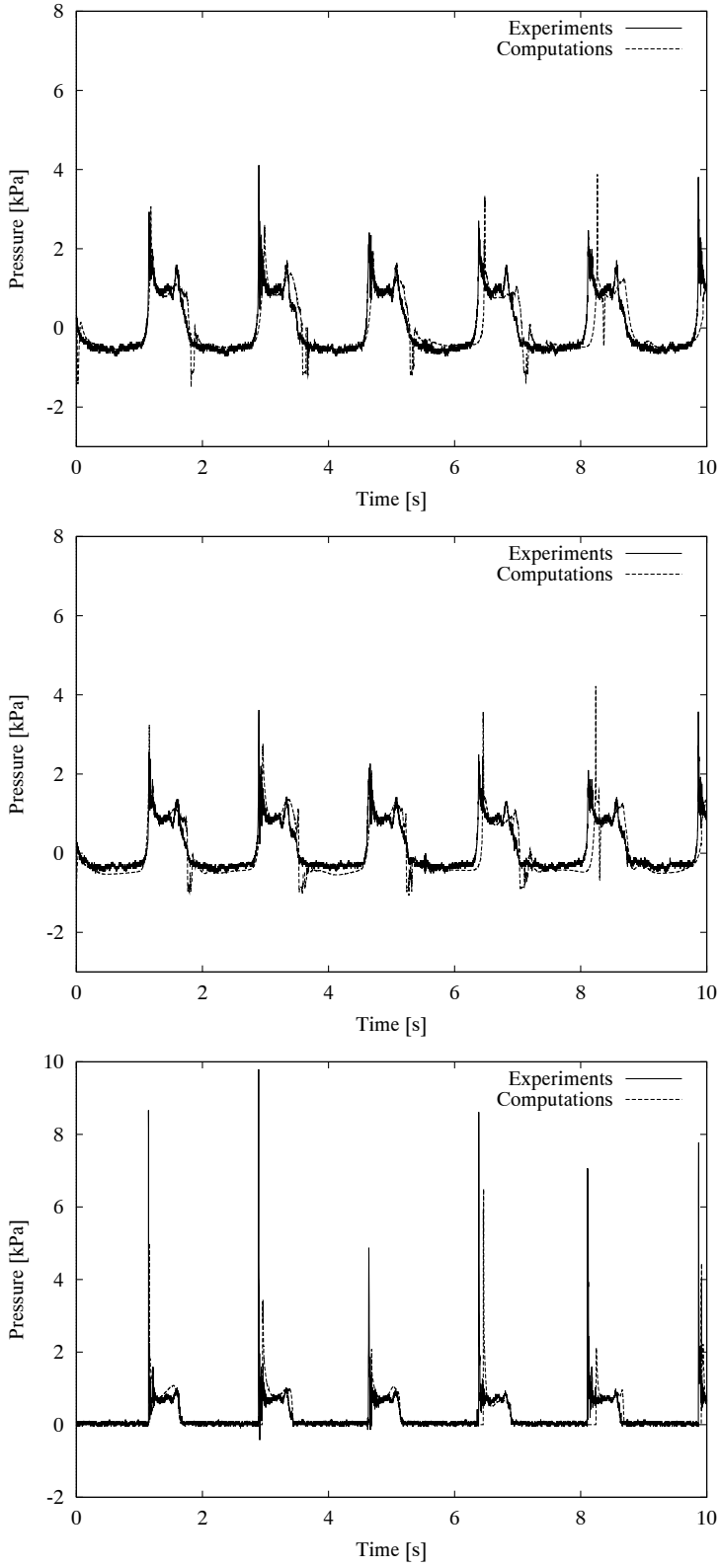

Figure 5.5: *Comparison of numerical and experimental (Hinatsu* et al., *2001) pressures, measured at gauges P1 (top), P2 (middle) and P3 (bottom), for sloshing Case 1. The grid resolution equals* 128×64 *grid cells.*

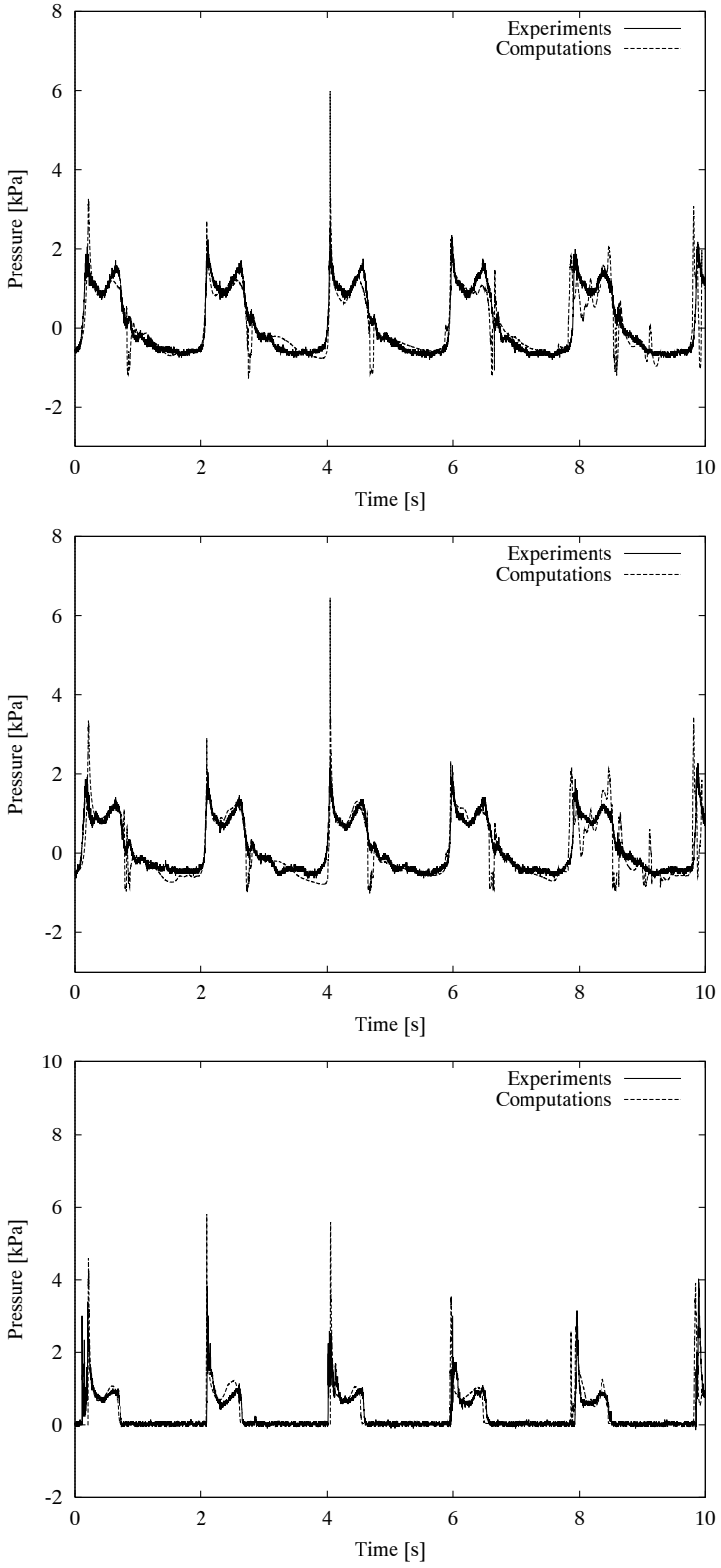

Figure 5.6: *Comparison of numerical and experimental (Hinatsu* et al.*, 2001) pressures, measured at gauges P1 (top), P2 (middle) and P3 (bottom), for sloshing Case 2.*

the other side of the tank. This results in a low pressure level of $\simeq -0.5$ kPa, which is equal to the static water pressure when the fluid is at rest. This is because that during the experiments the gauge was reset after the tank was filled and showed zero pressure, though the gauge was submerged. So when the gauge comes out of water it shows a value equal to the (negative) static pressure. The computed pressure, when the gauge is out of water, is set to -0.5 kPa in order to model the gauge being exposed.

P6 (top right) in Fig. 5.7 was initially out of water when the experiment was initiated. However, this gauge does not show zero pressure when the gauge is not under water. This indicates that the gauge was not properly reset before the experiment was initiated, and that the pressure level should be shifted slightly to bring the values of the exposed gauge closer to zero. With this in mind, the comparison between the magnitudes of the experimental and computed pressure shows good agreement, but the computed pressure also here shows a phase lag. Gauges P8 and P9 are out of the water during most of the experiment, but the figure shows pressure peaks each time the wave hits the right wall. The magnitude of the peaks is somewhat overpredicted by the computations, especially for gauge P9.

In Fig. 5.8 the pressure series for gauges P4, P6, P8 and P9 are shown for Case 4. The pressure measured at P4 is well predicted by the computations, but as previously a phase lag is present. P6 also shows little difference in the magnitude and profile of the pressure, but again the phase lag is present. As for Case 3, this gauge seems not to have been correctly reset which is revealed by the pressure level of the exposed gauge. Each time the gauge is out of the water the pressure level exhibits a short curving behaviour, because of the acceleration and deceleration of the tank which influence the probe. P8 and P9 are only wetted briefly, but the experiments here show larger peaks than in the previous case. Since the peaks for gauge P9 for the experimental and the computed pressure are very close, it is difficult to identify that both pressures have a large peak close to 5 s.

In Fig. 5.9 the relative mass is tracked during all four cases to investigate the loss of mass during the computations. The figure proves that after the first $1-2$ periods the domain loses mass, which is most apparent in Case 1. The loss of mass in the computations is caused by a cleaning routine, that is part of the solution procedure and is executed at each time step, as described in Chapter 3. The cleaning routine ensures that small regions of fluid, too small to be handled by the model, are removed. In the current case, the magnitude of the removed mass seems to influence the flow after a few periods.

5.4 Conclusions for Sloshing Test

In general the computations gives very good predictions for the sloshing flow, both in the visualisations and for the measured pressures. The dynamics of the flow is well predicted as the visualisations show some distinct flow features, such as the travelling wave inside the tank and the impact with the end wall of the tank which agrees very well between experiments and computations.

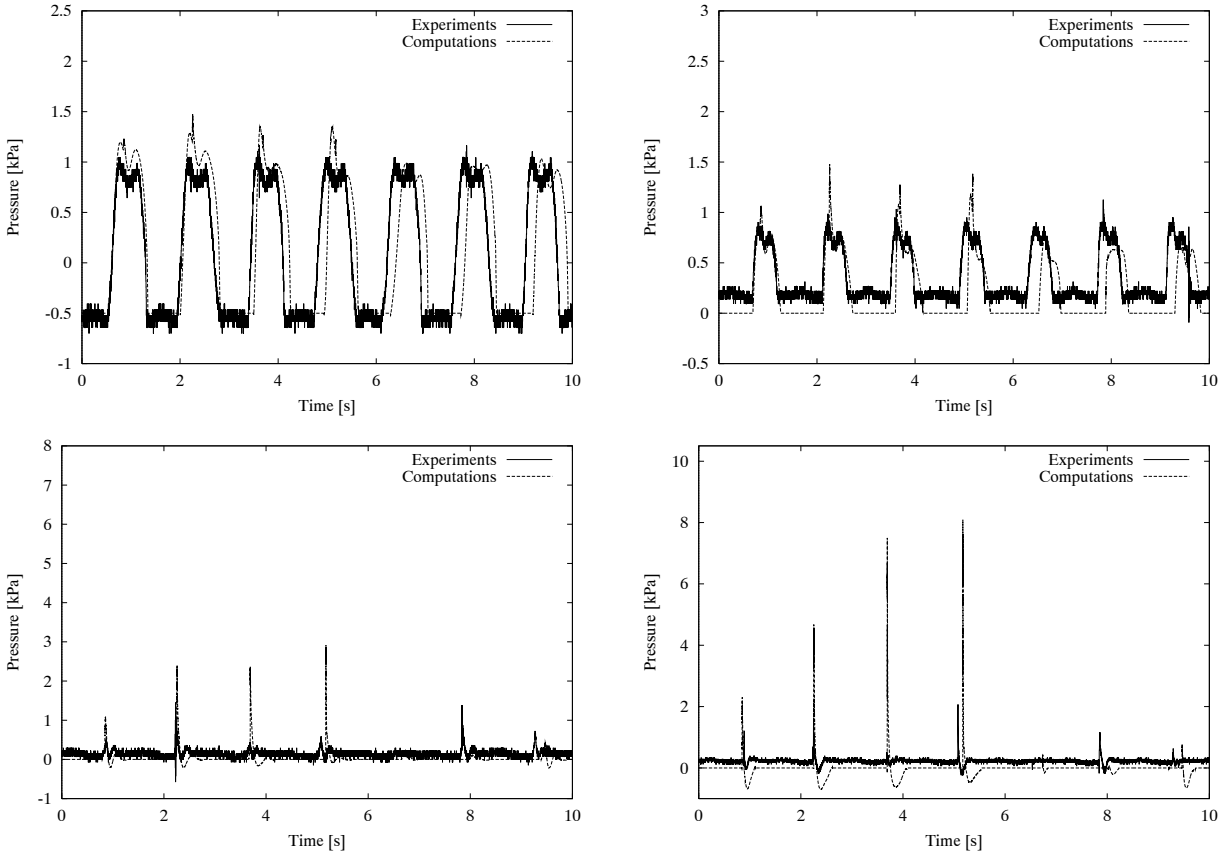

Figure 5.7: *Comparison of numerical and experimental (Hinatsu* et al., *2001) pressures, measured at gauges P4 (top left), P6 (top right), P8 (bottom left) and P9 (bottom right), for sloshing Case 3.*

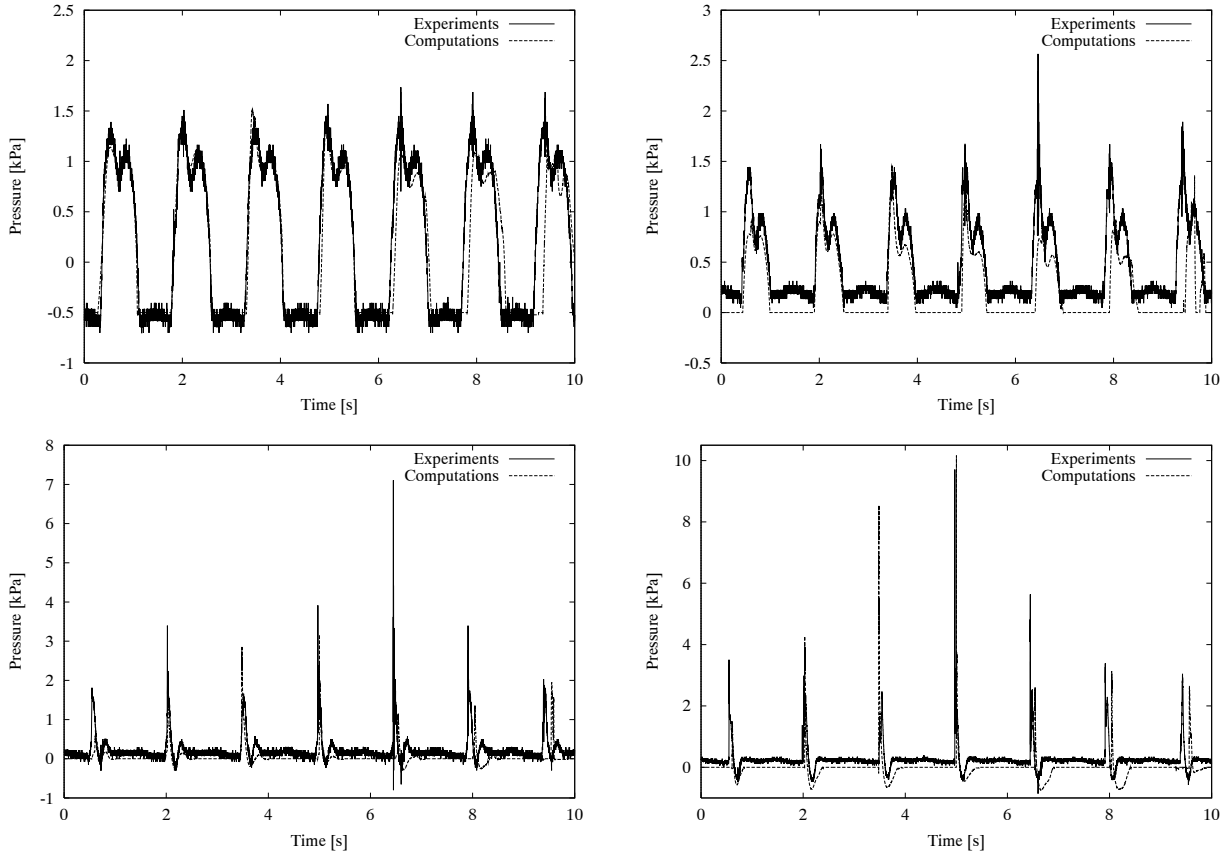

Figure 5.8: *Comparison of numerical and experimental (Hinatsu* et al., *2001) pressures, measured at gauges P4 (top left), P6 (top right), P8 (bottom left) and P9 (bottom right), for sloshing Case 4.*

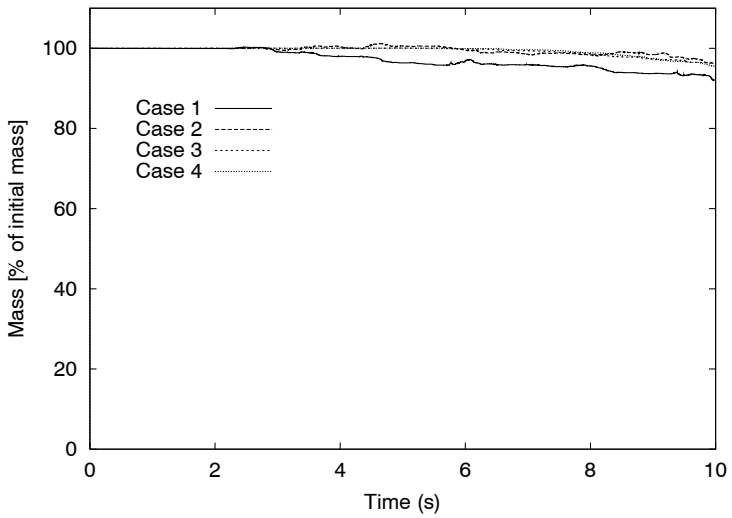

Figure 5.9: *Relative mass level for the four sloshing cases during the computations.*

The pressure levels inside the tank were also well predicted by the numerical model, since both the magnitude and the pressure profile for the impacts corresponded well. The formation of a bubble in the computations, which is not seen in the experiments, could be a result of the two-dimensional modelling. The 2-D modelling might overpredict some flow features which do not occur in the experiments.

The disagreement in the prediction of the accurate phase, where the computations showed a phase lag compared to the experiments, is more consistent. This starts after the first few periods, and grows throughout the simulation. The phase lag is due to loss of mass inside the domain, as illustrated in Fig. 5.9. The magnitude of mass being removed is normally insignificant, but for applications like the present sloshing case where a large amount of fluid sepertion from the free surface is involved, the amount of removed mass increases, which is significant to influence the flow properties, eventhough the small regions of separated fluid does not influence the water flow in the domain significantly. A new scheme has been implemented in the code in order to avoid removing too large quantities of mass from the domain, but this was not ready at the time of the present simulations and will be a topic for further study.

Chapter 6

Wave Impact Loads on Horizontal Rectangular Beams

In this chapter, wave impact loads on horizontal rectangular beams will be investigated by use of the NS3 model. This problem is connected with wave loads on offshore platform decks and not directly with green water loads. However, the problem is interesting in the sense that it can form a validation of the numerical model with respect to impact loads. Further, the wave impact on horizontal beams includes the very complex free surface interaction, which is also relevant for green water investigation.

6.1 Background

Prediction of wave-in-deck forces on offshore platforms has recently been given increasing attention for two reasons: (1) Subsidence of platforms and (2) Requalification of platforms for service time extension. Subsidence of platforms, caused by settlement of the soil foundation, decreases the air gap between the platform deck and the water surface. Re-qualification of older platforms requires new estimations of the ultimate limit state (ULS) condition waves, which often increases the design wave. In both cases there is an increased risk of impact of wave crests on the lower platform deck and on the beams on the underside of such decks, which increases the horizontal load on the platform significantly. To estimate the consequences of this wave impact an accurate prediction of the horizontal load is of vital importance.

Current industry standards for estimation of wave loads in the offshore environment are based either on direct model tests or on semiempirical approaches, including drag and inertia coefficients fitted for the appropriate deck element types and level of inundation, see e.g. Kaplan *et al.* (1995); Bea *et al.* (2001). Unfortunately, the empirical procedures do not take into account the change of flow kinematics due to the presence of the fixed body and the

influence this change has on forces on neighbouring structural members in typically combined structures. This is particularly important in descriptions of complex deck geometries and more complex wave kinematics.

Within the last decade a number of attempts have been made to predict numerically the combined effect of fluid motion and free surface changes around structures which penetrate from air into fluid. Since it can be shown that at least the initial stage of such water entry problems may be described within the framework of potential flow, most studies choose this approach. For example, Baarholm (2001) recently used a boundary element method (BEM) for solving the potential flow problem predicting impact loads underneath decks of offshore platforms. The method showed favourable agreement with experimental data at the initial stage of the impact and also predicted the water exit phase well.

When the potential flow approach is applied, it is not possible to handle the kind of topological changes of the fluid domain which occur when a volume of fluid separates or reconnects with the free surface. In such cases a line (in 2-D) or surface (in 3-D) is generated, across which only the pressure and the normal velocity are continuous while the tangential velocity is discontinuous. This discontinuity can be expressed by use of a vortex sheet and physically it is removed by diffusion into a region, which is not any more irrotational (and typically turbulent). As an alternative, free surface Navier-Stokes computations can be used for simulating the wave impact. The Navier-Stokes equation approach to wave impact problems has the advantage that topological changes of the fluid domain can, at least in practical terms, be handled in a relatively straightforward manner by use of interface capturing schemes such as the VOF method or the level-set approach, see e.g Arai *et al.* (1995); Muzaferija *et al.* (1998). As long as no topological changes are involved in the computation and the initial velocity field is irrotational, the predicted flow will in practice be irrotational and hence identical to the potential flow solution since viscous forces are negligible in real life applications. In these cases an accurate solution of free surface Navier-Stokes equations requires more computational effort than the equivalent potential flow solution and will be at a disadvantage.

While in theory the viscous terms are responsible for diffusion of vorticity away from the discontinuous vortex sheet, in practice the relevant Reynolds numbers in applications exceed by several orders of magnitude the limit of what can be resolved numerically by presentday computer technology. Hence, in reality the discontinuity is mostly damped by numerical dissipation, which will always be present in the codes, and the obtained solutions are often indistinguishable from solutions to the Euler equations on the same grid. In conclusion, from a formal point of view no converged solution of either the Navier-Stokes or the Euler equation will be obtained in configurations with complex free surface geometries, and the main advantage of using Navier-Stokes or Euler codes in water entry problems is their robustness. This is shown by the abovementioned work of Arai *et al.* (1995) and Muzaferija *et al.* (1998), both of which are practically solving inviscid flow problems. While Arai *et al.* (1995) only presents two-dimensional results in reasonably good agreement with measurements, Muzaferija *et al.* (1998) shows both two- and three-dimensional results, but in both

studies only one body was considered. Hence, the splashing of water was directed away from the body and it did not disturb the local pressure field close to the body boundary.

In this chapter the NS3 model, applied as an Euler solver, will be used for numerical simulation in two dimensions of the impact of wave crests on simple structural members with rectangular cross section, being a simplified model of structural elements used below platforms decks. Both a single structural elements and double elements are addressed. Particular focus is placed on the prediction of the interaction between the two bodies and the effect their proximity has on the wave impact loads. The numerically obtained forces are then compared to recent measurements and the results are discussed.

6.2 Experimental Data Used as Reference

The experiments were carried out at the large scale wave flume located at Forschungzentrum Küste (Grossen Wellenkanal (GWK)) in Hannover, Germany. The channel measures 300 m in length, has a maximum water depth of 7 m and a width of 5 m. With a piston type wave maker a maximum wave height of about 2 m can be produced. For details on the experimental procedure, see Sterndorff (2002). In the following only a brief outline is given of those aspects of the experiments which are important to the present numerical work.

The instrumentation of the flume consisted of a series of wave gauges along the channel measuring the free surface elevation with an accuracy of about ± 1.5 cm. Three electromagnetic flow gauges were mounted at a distance of $x_{struct} = 105$ m from the wave maker and at a distance from the bottom of 1.8 m, 2.8 m and 3.8 m, respectively. In the same axial position a transverse rectangular beam section of the height $h_{beam} = 0.1$ m, the thickness $d_{beam} = 0.01$ m and the length $l_{beam} = 1$ m was mounted with its lower edge $y_{struct} = 5.7$ m located above the flume bottom, see Fig. 6.1. At either end of the beam, dummy elements were placed with the same crosssectional profile in order to diminish end effects. The test beam was mounted on two force gauges measuring the load in all three dimensions. In later series several equivalent beams were placed behind each other with equidistant spacing. All time series (wave elevation, velocity and forces) were sampled electronically at the same data rate of 200 Hz and with a 16 bit resolution. The position of the elements was fixed during all tests. Different loading situations were realised by varying the nominal wave height H_n, the wave period T and the mean water level h.

A test run was started with water at rest everywhere with the wave maker generating an almost regular wave train with the period T and the nominal height H_n, for details see Sterndorff (2002). One test run had a duration of approximately the time needed for the first wave to be reflected from the end of the flume and travel back to the location of the test rig. The generated steep wave train clearly showed transients at startup and further exhibited spurious low frequency modes, altering the elevation at a given point within at least 10 cm. Further, the nominal wave height and the wave period were given as input parameters to the wave generation control unit - however, the nominal wave height only

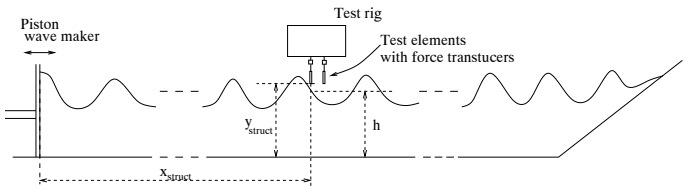

Figure 6.1: *Sketch of setup of reference experiments at GWK.*

Cases		A	B	C	D
No. of beams		1	1	2	2
Mean water depth (h)	[m]	5	5	5	4.8
Wave period (T)	[s]	5	5	5	5
Nominal wave height (H_n)	[m]	1.4	1.5	1.4	1.8
Wave height (H)	[m]	1.34	1.43	1.35	1.7
Crest height (η_{crest})	[m]	0.79	0.85	0.80	1.07
Inundation (β)	[%]	90	154	100	170

Table 6.1: *List of Test Cases A,B,C,D.*

agreed with the actually measured wave heights within 10 %. Therefore, for every test run, individual wave impact scenarios were extracted. For every scenario the peak elevation η_{crest} in the x-location of the structure was recorded, and a local relative inundation β was computed from

$$\beta = \frac{\eta_{crest} + h - y_{struct}}{h_{beam}}. \tag{6.1}$$

In the following only the horizontal force is used for validation, since this force component is dominating due to the small thickness of the beam section and because the horizontal load constitutes the critical component with regard to the stability of platform decks. The total force on the beam was measured as the sum of forces from the two force gauges on the beam. The difference between the two gauges was used as a measure of the two-dimensionality of the wave and flow fields to which the beam was exposed. Generally for a given test run, the measured forces on either side of the beam were initially equal to within a few percent. However, with an increasing number of impacts within a test run turbulent disturbances were created in the water column below the test rig and a clearly visible small scale wave component normal to the channel appeared. This caused increasing differences between the forces at either ends of the beam, as time went on. Therefore in the following, the impact scenarios selected for validation are all taken within the first three impacts of a test run.

Four different cases are presented in the following: two cases with a single beam section (A and B) and two cases with two beams mounted closely together (C and D), see Table 6.1.

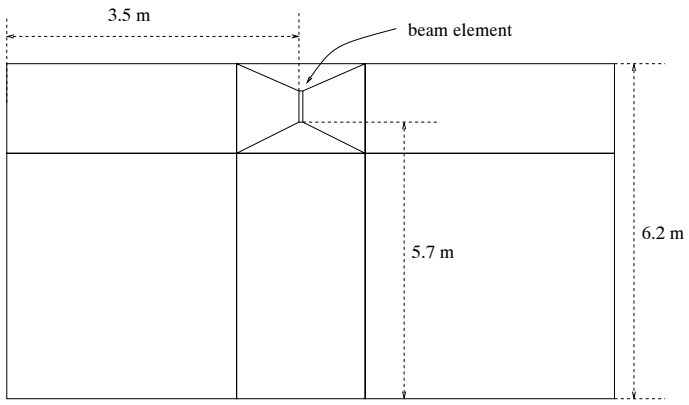

Figure 6.2: *Sketch of computational domain with multiblock topology layout.*

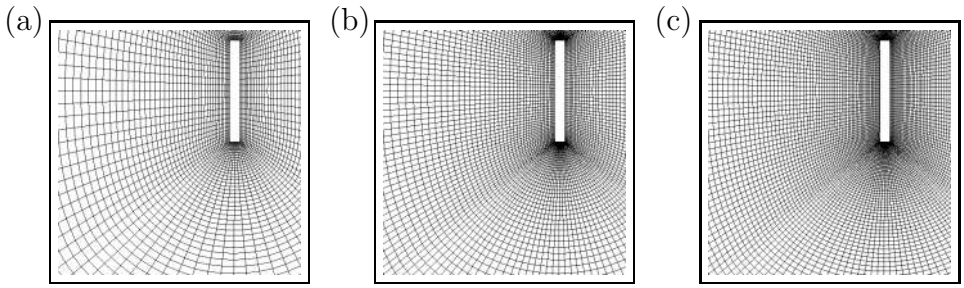

Figure 6.3: *Close-up of grid close to the first structural element. a) Coarse b) Medium c) Fine.*

6.3 Numerical Setup

Only a section of the wave flume is covered in the computational domain, of a total equivalent physical length of 10 m. The structure is located 3.5 m from the inlet boundary, see Fig. 6.2. A multiblock grid is generated with cells being refined close to the structure and cells being enlarged with increasing distance from the structure. The rectangular cross section of the structural elements is smoothed at the corners of the profile to improve grid quality, since for the layout of the multiblock grid an O-grid topology has been chosen around the structural element (in the following the inner block layer). Around this inner layer of blocks eight blocks are defined in an H topology. The spatial resolution of the outer block layer is fixed throughout the present study. The grid dependency of the simulations is examined by using three different resolutions (coarse, medium, fine) for the inner block layer. The coarse grid has 32 grid cells on the horizontal sides of the beam (N_H), 16 grid cells on the vertical sides of the beam (N_V) and 64 cells radially (N_R), for the medium grid and the fine grid those numbers are (N_H,N_V,N_R) = (64,32,64) and (64,32,96), respectively, see Fig. 6.3.

6.3.1 Wave Generation

A critical step in the validation procedure of the numerical method has been to generate in the code an appropriate wave flow field before impact. A deviation of the wave amplitude of just 1 cm corresponds to a quite significant 10% change of inundation. Therefore, the use of nominal wave heights in the numerical simulation is clearly no option, as the measured crest height deviates from the nominal values by more than 10 cm. Since the displacement time history of the wave maker piston has not been recorded, direct modelling of the wave generation process as in Mayer *et al.* (1998) is not possible. However, if it had been possible, the large size of the experimental wave flume compared to the necessary resolution close to the structures would have implied a very considerable computational overhead, if wave and flow fields were to be generated in a domain corresponding to the entire wave flume.

Therefore, the following procedure was used. For every selected wave impact scenario the peak elevation η_{crest} in the x-location of the structure was recorded. Then an optimisation procedure was used to find the height H and the mean water level η_o of a fully nonlinear wave of constant form with given period T and crest height η_{crest}, which gives the best match relative to the measured elevation time series. For describing the nonlinear wave the stream function theory of Rienecker and Fenton (1981) was employed. At a time instant just before initial impact t_i the stream function theory was then used to compute the elevation profile $\eta_i(x)$ and subsequently the void fraction field $f_i(x, y)$. Further, the flow field $\boldsymbol{u}_i(x, y)$ was computed. By sampling $f_i(x, y)$ and $\boldsymbol{u}_i(x, y)$ for all grid points in the computational domain of NS3, initial conditions for the unsteady flow computation were established. This procedure ensures that for the numerical setup the profile inundation and wave characteristics are identical to those of the experiments and to the accuracy of the wave gauges. For control purposes, test computations are carried out without the presence of structures in the computational domain for test Cases A and B. Figs. 6.4 and 6.5 show a comparison of the measured and computed time history of the wave elevation at x_{struct} and the velocity at $x, y = (x_{struct}, 3.8)$. The agreement is seen to be good, apart from a small phase lag in both the elevation and the velocity time series.

6.4 Verification of Numerical Results

For Case A a grid sensitivity study has been carried out. Fig. 6.6 shows the resulting force on the beam section, calculated with the three grids. The force time history shows gridindependence for the medium and fine grids, so these are considered to be sufficiently fine for obtaining - in practical terms - converged solutions for the force time series. A characteristic spike in the total horizontal force is seen for all three grids at the initial stage of the wave impact, this feature is found in most simulations with sufficiently fine gridding. The spike is the result of water which separates from the front bottom corner at a high velocity. The separation process generates a large local pressure gradient at the lower front corner of the profile, increasing the pressure level in the whole region around that corner.

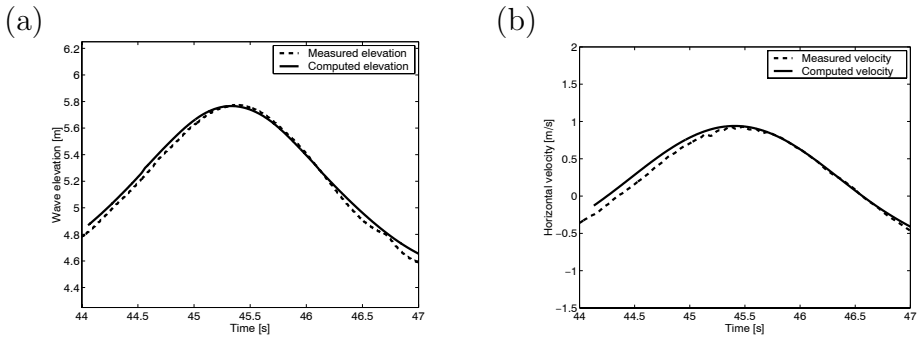

Figure 6.4: *Simulation of undisturbed wave. Case A:* $H = 1.34$ *m,* $T = 5$ *s and* $h = 5$ *m. Comparison of numerical and measured time series. a) elevation at* $x = 105$*, b) velocity at* $(x, y) = (105, 3.8)$.

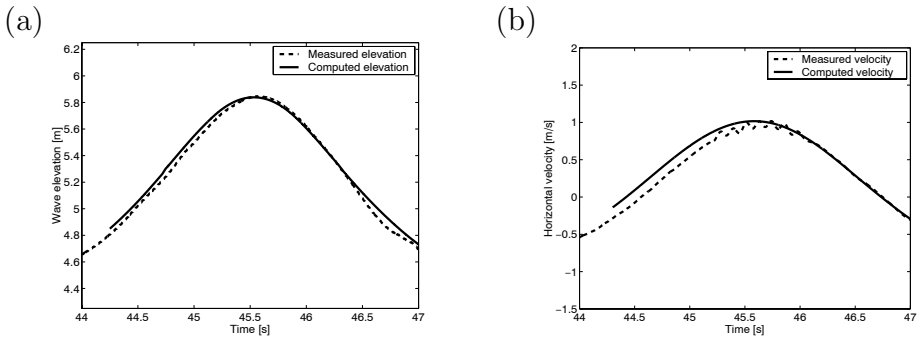

Figure 6.5: *Simulation of undisturbed wave. Case B,* $H = 1.43$ *m,* $T = 5$ *s and* $h = 5$ *m. Comparison of numerical and measured time series. a) elevation at* $x = 105$ *m b) velocity at* $(x, y) = (105, 3.8)$.

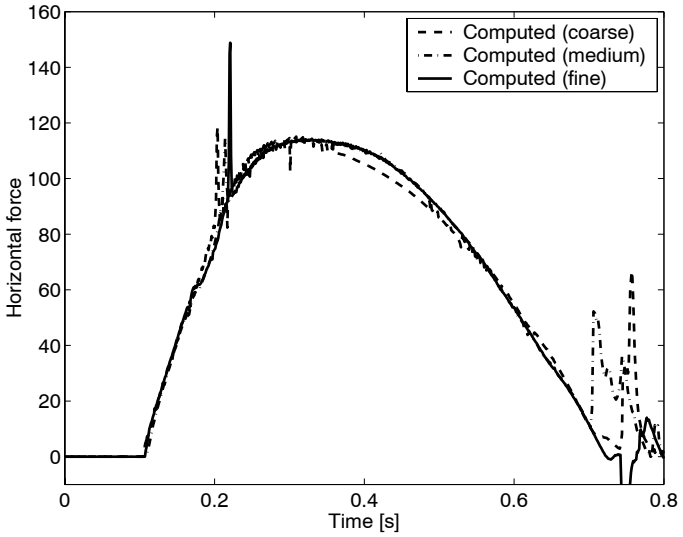

Figure 6.6: *Force time histories for grid sensitivity test with three grids. Incident wave* $H = 1.34$ *m,* $h = 5$ *m,* $T = 5$ *s.*

Even though the separation process is very short, it is resolved by several tens of time steps in the calculation.

In addition to the grid sensitivity study, the effect of the Courant number criterion C_{cfl} and thus of the time step size has also been investigated. For Case A, a change of the criterion to $C_{cfl} = 0.1$ had no significant influence on the results.

6.5 Resulting Pressure Compared between Computations and Experiments

6.5.1 One Beam Element

Fig. 6.7 shows snapshots of the free surface contours in the numerical simulation for the single element Case A, with the incoming wave height $H = 1.34$ m and a profile inundation of $\beta = 90\%$. The free surface contours are captured at four different time steps as the incoming wave encounters the structure. At the initial stage of the encounter the wave pushes a water jet up along the profile. Once it reaches the top of the profile, the jet continues over the profile in the wave propagation direction and encloses a void of air behind the profile.

Fig. 6.8 shows the computed time histories of the total horizontal force for Test A. In the plot the instants a-d are indicated, which correspond to the snapshots of Fig. 6.7. The force

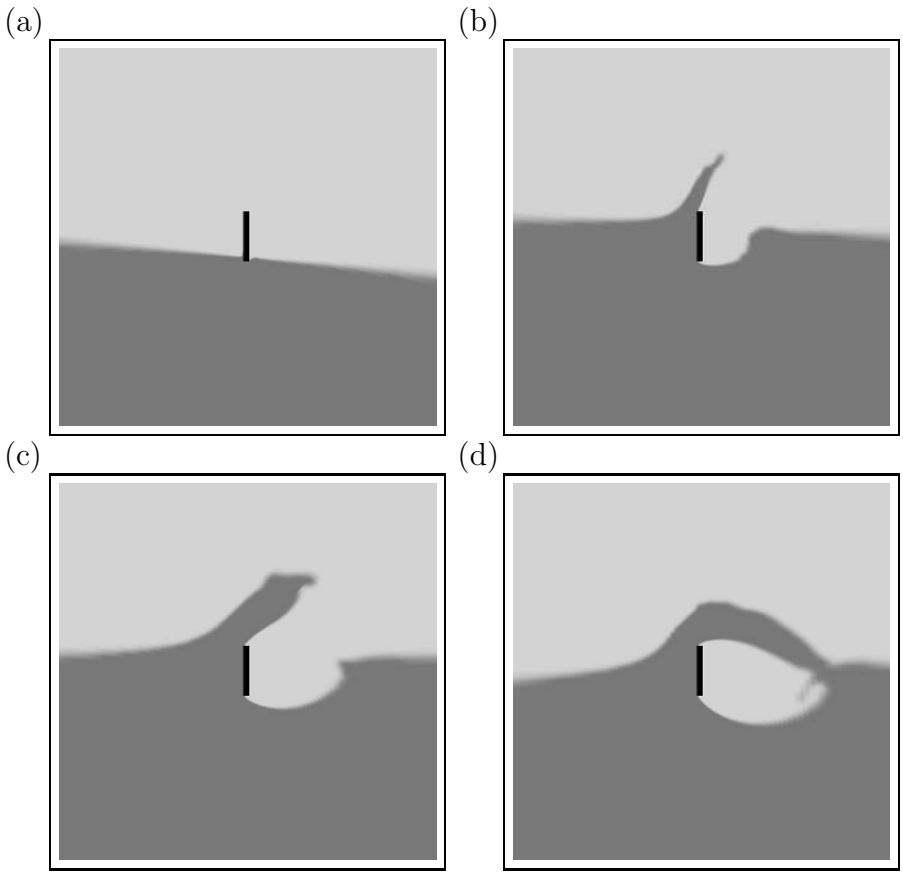

Figure 6.7: *Simulation of wave impact on a single beam. Case A: Incident wave* $T = 5$ *s,* $H = 1.34$ *m,* $h = 5$ *m, inundation* $\beta = 90\%$*. Free surface geometry at wave impact. Time interval between images 0.15 s.*

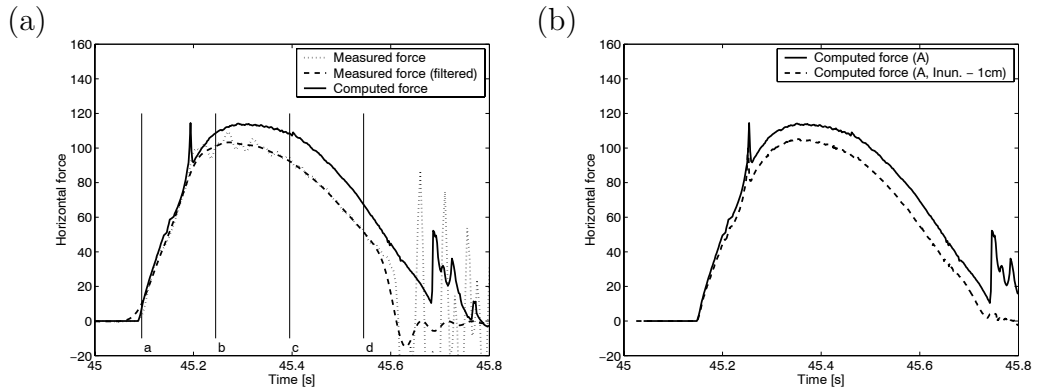

Figure 6.8: *Simulation of wave impact on a single beam. Case A: Incident wave $H = 1.34$ m, $h = 5$ m. Horizontal force time histories for three different grids. Lines a-d indicate times of snapshots in Fig. 6.7. a) inundation $\beta = 90\%$, b) inundation $\beta = 90\%$-10%.*

time history can be divided roughly into three stages: First an initial impact where the resulting force on the element rises very quickly as the incoming wave builds up on the front side of the beam. At the second stage the steep gradient of the force history is reduced and the rise of the resulting force is smaller and the curvature smoother. After reaching its maximum, the force slowly approaches zero at a constant rate of change.

The measured total force is also shown for comparison. Throughout the experiments, problems were encountered due to insufficient stiffness of the test rig. The wave impact frequently excited vibrations of the test rig, which appeared in the force measurements as large amplitude oscillations. Therefore, a post-processing procedure is employed in order to remove the fluctuations caused by vibrations of the structure. This filtered data is also shown in Fig. 6.8a for Test A. Of course, filtering introduces a risk of modifying or removing part of the actual load signal. However, since these fluctuations are in a high frequency range compared to the duration of the whole load sequence, this risk is expected to be acceptable. The numerical results are seen to over predict the measured forces to some degree, and also the duration of the load sequence is predicted to be longer than measured. One explanation for this could be that the effective crest height of the incoming wave was somewhat lower in the experiment than measured by the wave gauge. To show the sensibility of the computed forces to changes in inundation, a simulation was carried out with the inundation decreased by 1 cm, corresponding to a decrease of β of 10%, bringing the numerical results very close to the measurements, see Fig. 6.8b. Of course, the decrease of the peak force is in agreement with expectations, since the momentum of less water is transferred to the structure. Furthermore, the duration of the loading phase is shortened, since with decreased inundation the width of the wave crest at the level of the lower edge of the beam is shrunk, decreasing the time for the structure to leave the wave crest.

For Case B the incoming wave height is increased to 1.43 m, and the corresponding free surface contours from the numerical simulation are shown in Fig. 6.9. The figure also shows that a larger part of the incoming wave runs over the structure than in Case A. In the initial

phase the flow patterns are similar to those of Case A, however, during the exit stage of the impact scenario the free surface geometry is clearly more complex.

The force time history of Case B is shown in Fig. 6.10a. The load pattern is similar to the previous one, but the magnitude is increased and the duration of the load is longer, which is to be expected due to the larger incoming wave. In addition to the short duration spike in the uprise phase, a spike appears in the decay phase of the force time history. This is due to the influence of a jet impinging on the lower side of the profile from behind, as it rushes downwards within the 'void bubble' which is seen behind the profile. The impinging of the water on the lower side of the profile influences the pressure levels around the lower front corner, and for a short time interval raises the pressure level on the upstream side. Further, a few additional negative peaks of much smaller magnitude are seen when sprayed water impinges directly onto the downstream side of the profile. However, apart from the presence of the short duration peaks in the load time series, excellent agreement is found over the entire load sequence between numerical and experimental results. As in Case A, the computations are repeated for the inundation decreased by 1 cm, see Fig. 6.10b. The peak load is seen to be lesser affected by changes in the inundation, than in Case A.

6.5.2 Two Beam Elements

In Cases C and D a second beam section is placed 20 cm behind the existing beam, located in the direction of wave propagation. Fig. 6.11 shows the free surface contours from the numerical simulation of the twoelement Case C. It should be noted that the wave run-up is not as significant on the second profile as it is on the first, and the amount of water shipped over the second profile is significantly smaller than for the first profile.

While the load pattern on the first structure in Fig. 6.12a is similar to the previous one, the load pattern on the second beam is different, see Fig. 6.13a. For this beam, the force history shows two distinct peaks, separated by a region with zero force. The first peak results from the initial wave impact, and the second peak is caused by the water jet being shipped over the first beam and onto the second. The magnitude of both peaks on the second element is reasonably well reproduced in the calculations, but a small phase lag is noted.

In the last Case D the water depth (h) is lowered to 4.8 m, but the elevation of the incoming wave is higher, resulting in an increased profile inundation $\beta = 170\%$ and a considerable increase in the velocity of the impinging water. Fig. 6.14 show snapshots of the free surface, indicating that the amount of water shipped over the first beam is significantly increased compared to the previous Case C.

Figs. 6.15a and 6.16a show the force time histories on the two beams for Case D. The shielding effect is also evident in the force history, where the load pattern on the second beam differs significantly from the first beam, similar to what is seen in Case C. In particular the duration of the first peak in Fig. 6.16a is seen to be considerably reduced compared to

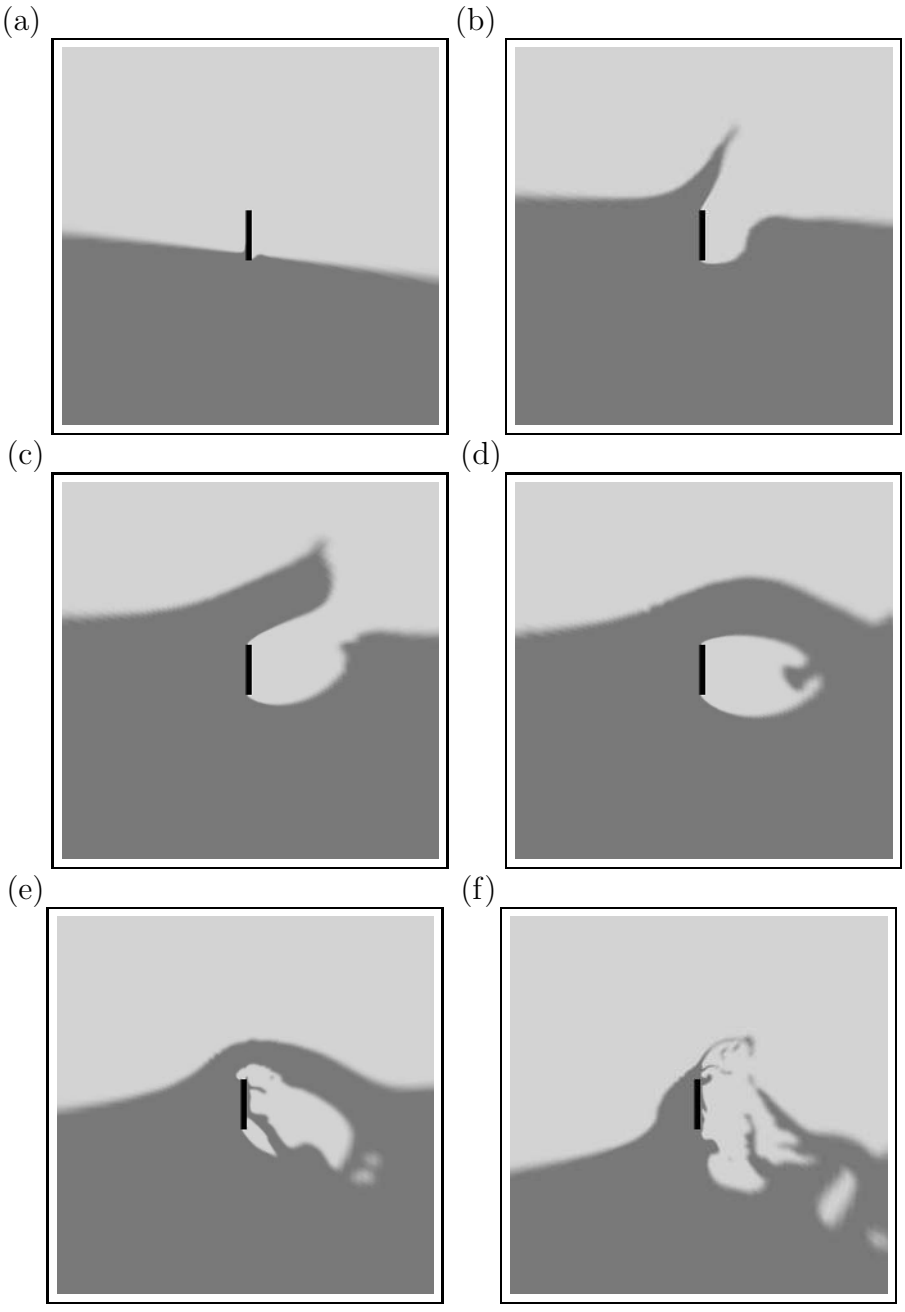

Figure 6.9: *Simulation of wave impact on a single beam, Case B: Incident wave* $H = 1.43$ *m,* $h = 5$ *m, inundation* $\beta = 154\%$*. Free surface geometry at wave impact. Time interval between images 0.15 s*

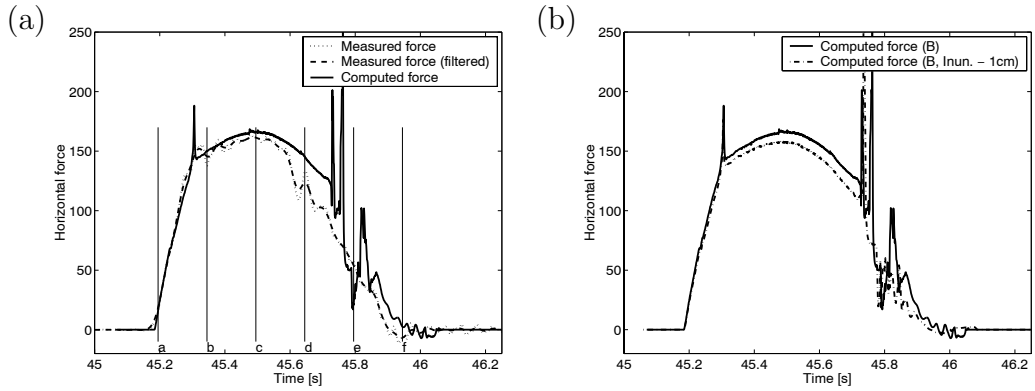

Figure 6.10: *Simulation of wave impact on a single beam. Case B: Incident wave* $H = 1.43$ *m,* $h = 5$ *m. Horizontal force time histories for three different grids. Lines a-f indicate times of snapshots in Fig. 6.9. a) inundation* $\beta = 154\%$*, b) inundation* $\beta = 154\%$*-10%.*

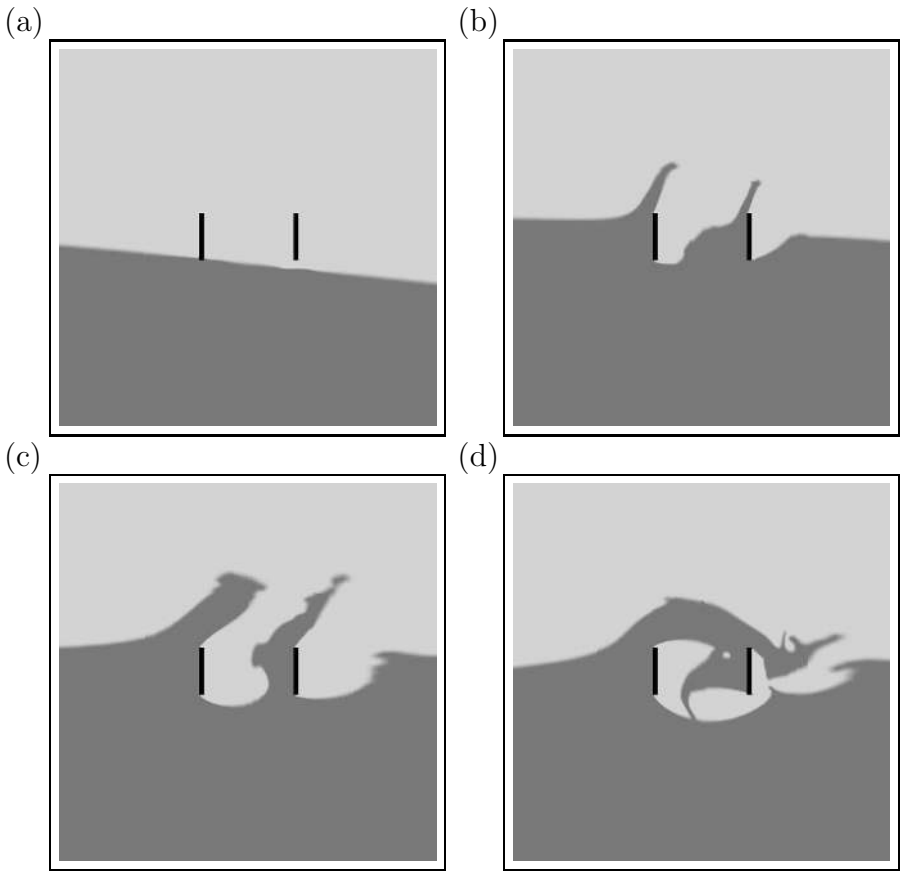

Figure 6.11: *Simulation of wave impact on a two beams, Case C: Incident wave* $H = 1.35$ *m,* $h = 5$ *m. Inundation* $\beta = 100\%$*. Free surface geometry at wave impact. Time interval between images 0.15 s*

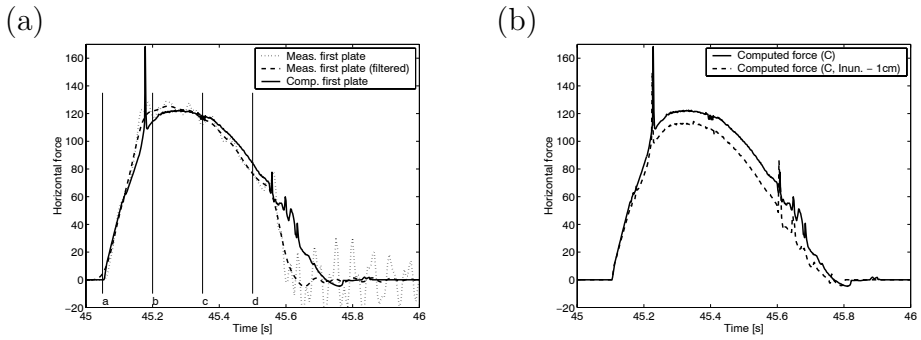

Figure 6.12: *Simulation of wave impact on two beams, Case C: $H = 1.35$ m, $h = 5$ m. Horizontal force time histories on first beam. Lines a-d indicate times of snapshots in Fig. 6.11 a) inundation $\beta = 100\%$ b) inundation $\beta = 100\%$-10%.*

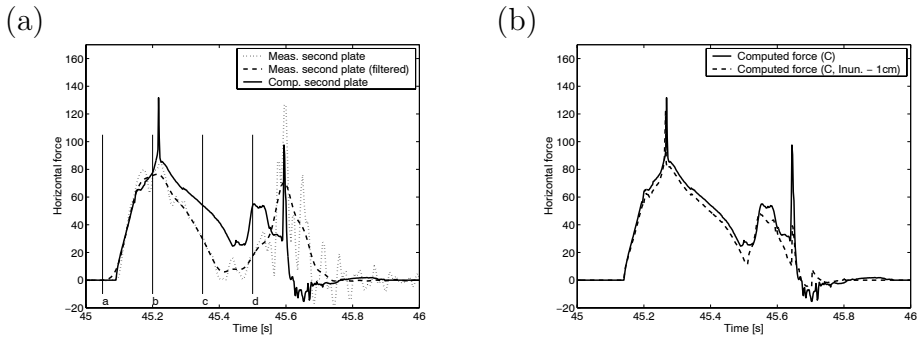

Figure 6.13: *Simulation of wave impact on two beams, Case C: $H = 1.35$ m, $h = 5$ m. Horizontal force time histories on second beam. Lines a-d indicate times of snapshots in Fig. 6.11 a) inundation $\beta = 100\%$ b) inundation $\beta = 100\%$-10%. Lines a-d indicate times of snapshots in Fig. 6.11*

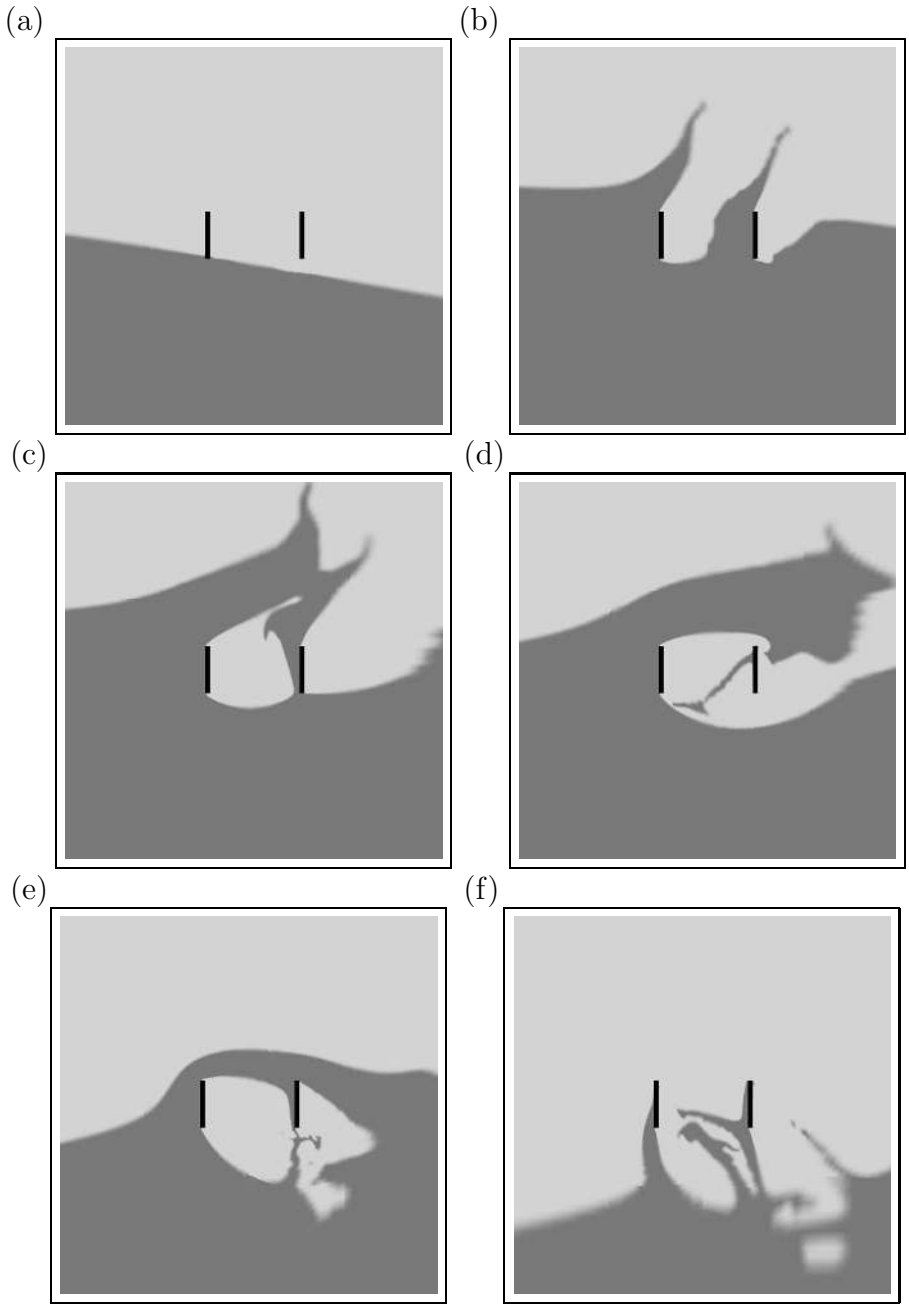

Figure 6.14: *Simulation of wave impact on two beams Case D: Incident wave* $H = 1.71$ *m,* $h = 4.8$ *m. Inundation* $\beta = 170\%$*. Free surface geometry at wave impact. Time interval between images 0.15 s.*

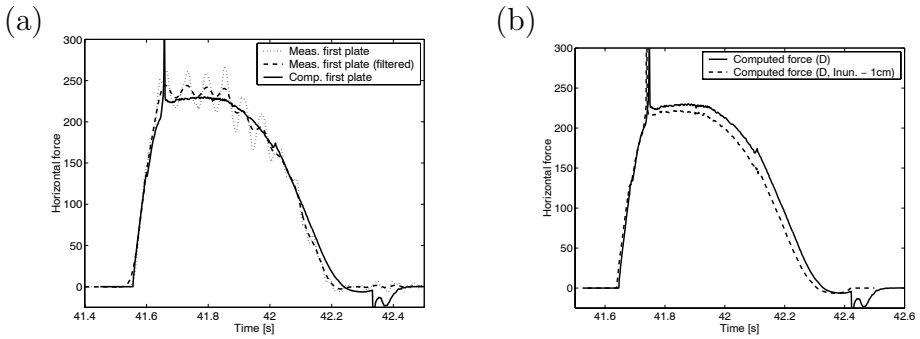

Figure 6.15: *Simulation of wave impact on two beams. Case D: Incident wave $H = 1.75$ m, $h = 4.8$ m. Horizontal force time histories on first beam. Lines a-f indicate times of snapshots in Fig. 6.14. a) inundation $\beta = 170\%$, b) inundation $\beta = 170\%10\%$.*

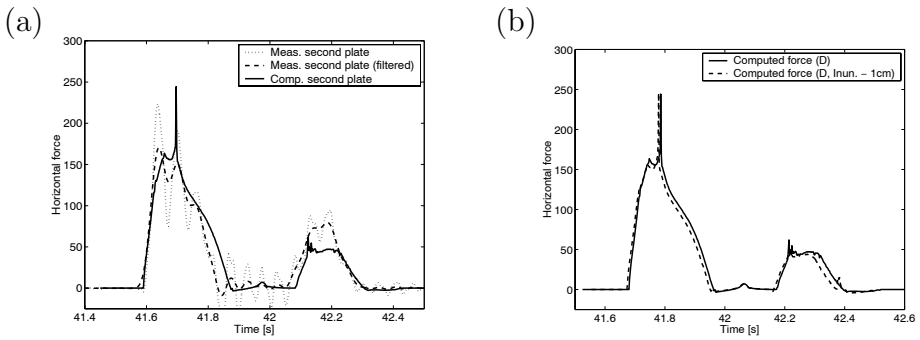

Figure 6.16: *Simulation of wave impact on two beams. Case D: Incident wave $H = 1.75$ m, $h = 4.8$ m. Horizontal force time histories on second beam. Lines a-f indicate times of snapshots in Fig. 6.14 . a) inundation $\beta = 170\%$, b) inundation $\beta = 170\%$-10%.*

Fig. 6.15a, while the peak level is less affected. Again a second load peak is predicted on the second element, in this case with both force levels and the overall shape of the peak being in very good agreement with the measured data. The whole force history for both elements is well predicted in the numerical calculations, compared to the experiments. The second load peak of the second beam is somewhat under predicted but opposed to Case C the timing of the peak is seen to be correct. As in Cases A and B, the two beam computations are repeated for the inundation decreased by 1 cm, see Fig. 6.12b, Fig. 6.13b, Fig. 6.15b and Fig. 6.16b, respectively.

6.6 Discussion and Conclusion

An attempt has been made to predict the horizontal loads on simple structures with rectangular cross section. The premise of the present work has been that the problem can be described within the framework of inviscid flow and in two dimensions only. Great care

has been taken in the experiments to reduce three-dimensional effects. While three dimensional disturbances clearly evolved during the individual test-runs, the assumption of two-dimensionality seems to be reasonable, since only the first few impacts within a test run are used for comparison, where the difference between the measured force time series on each end of the beam sections is small.

The results from Tests A and B show that both the magnitude and the duration of the loading of one single isolated beam are well predicted. The differences between numerical data and measurements are within the experimental uncertainty, as it is shown by the sensibility study of the result to changes in the nominal inundation β. The change of the inundation of 1 cm in these computations is clearly smaller than the precision of the wave gauges. While excellent overall agreement has generally been found between the computational results and the measurements, two types of spikes appear in the numerical results which are not seen in the experimental data. One type of spike is connected with the separation of water along the lower bottom side of the beam. The other type of spike is due to the impact of a jet which impinges from behind within the void bubble. In both cases, the physics of the flow are simplified by the numerical code. A proper description of both the jet and the separation should include the role of viscous stresses and turbulence. Further, flow features on such small scale compared to the overall flow will in any case be three-dimensional and when integrated over the entire length of the beam hardly be visible as such. Further, it should be noted that, by using the same filtering procedure for the numerical force time series as that used for the experimental data, effectively all the encountered spikes would be reduced to insignificant levels. Generally, in the two dimensional computations the spikes do not play a major role in the overall transfer of momentum from the water to the structure due to their short duration.

One of the main purposes of this study was to investigate whether the interaction of neighbouring elements can be successfully predicted. The present results seem to indicate that this is possible. Overall, the accuracy of the forces on the second element seems to be somewhat lower than that on the first element. However, the main features of the load sequence on the second element are well predicted and the computed peak loads are within acceptable agreement with the measured data.

In conclusion it seems likely that the present method or similar approaches can be used for prediction of loads also in more complex cases, including three dimensional structures in more complex three-dimensional sea states. In this context the major problem to overcome will be the rather great computational resources required by such studies.

Chapter 7

2-D Wave Run-up and Simplified Green Water Shipping

As presented in Chapter 1, green water loads on ships and FPSO's are a complex phenomenon, involving ship wave interaction, wave diffraction and reflection, wave overturning and breaking, and complicated flow on deck. In order to simplify the simulation of green water loads, the problem will initially be investigated in 2-D and the interaction effects will be reduced. First, a 2-D wave run-up problem will be investigated where an incoming wave encounters a solid wall and flows onto the top of the wall. This problem can be seen as an initial stage of green water shipping. Second, the wave impact on a 2-D FPSO will be investigated, with waves encountering an FPSOlike structure, for which the resulting wave heights on deck and the impact with a structure located on deck are measured. Both cases are investigated numerically and the results are compared to experimental data.

7.1 Wave Run-up on a Solid Wall

Wave run-up on a solid wall was investigated in a wave flume, with a wave generator at one end and a wall at the other, with a small clearance from the mean water level to the top. The incoming waves run up and over the wall and the free surface contours are captured during the run-up so the physics of the flow up along the wall, and the shipping of the water over the top edge of the wall can be investigated. A sketch of the wall rup-up problem is shown in Fig. 7.1.

7.1.1 Physical Setup of Wave Run-up Problem

Wave run-up was experimentally investigated by Cozijn (1996) both to model the early stages of a green water incident but also to evaluate the effect of ship's bow geometry on green water

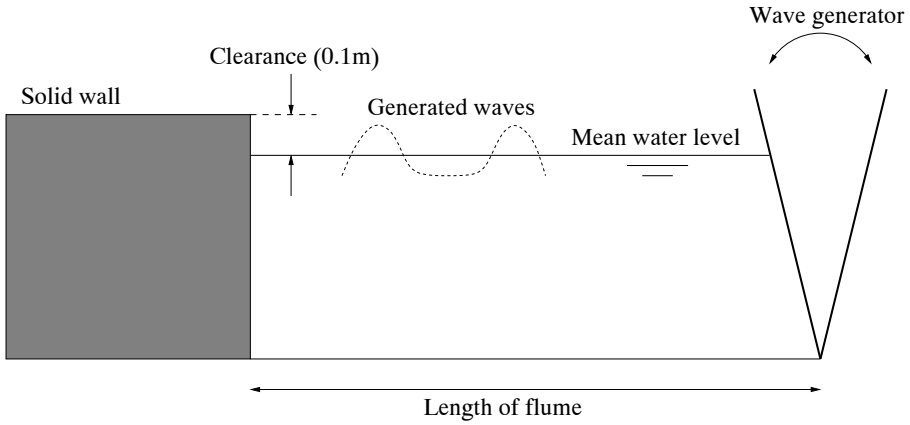

Figure 7.1: *Sketch of wave run-up on wall. The length of the flume is used as a parameter in the numerical study.*

shipping. The study was carried out on simplified structures using two different types of wall: the first configuration was just a normal square wall, and in the second case a shiplike flare was added to the wall. The two configurations are presented in Fig. 7.2. Table 7.1

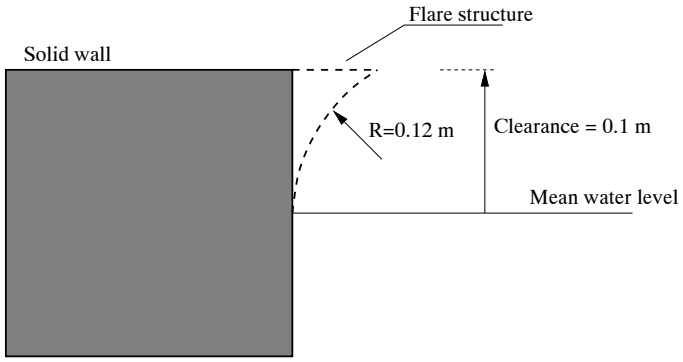

Figure 7.2: *Wall geometry in wave run-up case.*

gives the wave parameters for the two run-up experiments. The experiments were initiated when the flap type wave generator was set in motion, and the waves started travelling from the wave maker toward the structure. In the flume, 29.86 m in total length, three wave gauges were placed to record the wave elevation during the experiments. They were placed 26.29 m, 5.31 and 0.40 m from the solid wall, respectively. The resulting wave heights were measured by means of the gauge located nearest to the wave generator. In both experiments the wave generator was given the same input parameters, where the maximum flap motion amplitude equalled 5^o and the flap period was 1.256 s but still rendered slightly different resulting wave heights when measured in the wave flume. The difference in generated wave heights was approximately 3 %, which can be caused by disturbances in the flume from a previous experiment, measuring inaccuracy or other factors. The experiments also reported problems with the hydraulic system controlling the flap motion, which could also cause the difference in generated wave heights.

Case	Run-up A	Run-up B
Water depth	1.03 m	1.03 m
Wave height	0.128 m	0.132 m
Wave period	1.257 s	1.257 s
Wave length	2.503 m	2.507 m
Clearance	0.1 m	0.1 m
Structure	Wall	Flare

Table 7.1: *Wave kinematics for run-up cases.*

During the experiments the free surface location was recorded on video in order to capture the dynamics of the flow while the wave runs up and over the wall. A plate was placed on the wall, perpendicular to the incoming waves, on which a square grid had been drawn. The grid was used to indicate the proportion of the shipping wave in the video recordings, and by use of the individual still frames from the video recordings, the free surface location could be determined from the grid and plotted for each time step. These free surface contours are used for comparison with the numerical results. Unfortunately, the experiments did not indicate which incoming wave crest was used to plot the free surface contours, so it was not possible to evaluate how long after the experiments had started the free surface contours had been captured. For the experiment with the straight wall (Run-up A) three different wave contour series were plotted, captured for three different shipping incidents. These series of shipping waves did not show exactly the same type of behaviour, though the maximum shipping water height above the wall and the contour lines of the water travelling along the top of the wall were quite similar. Even though the exact wave crest used for the shipping incidents was not indicated, the time between the three incidents was stated, as equal to 16.8 s and 29 s, respectively. In the flared case (Run-up B) two different incidents were recorded, in which the shipping wave also exhibited a slightly different behaviour. These two wave incidents were taken from consecutively incoming waves.

7.1.2 Numerical Simulation of Wave Run-up

The computational domain is shown in Fig. 7.3. It illustrates the type of boundary conditions applied, and shows the three blocks (BL1, BL2 and BL3) into which the domain is divided. The domain length in the figure is used as a parameter in the validation of the numerical results.

In the numerical computations the water is initially at rest and waves are generated at the right outer boundary shown in Fig. 7.3. The horizontal velocity components are imposed where the magnitude of the velocity has been determined from stream function theory, as described in Appendix A.

To investigate the influence of the flume length on the resulting wave generation and on the shipping wave, four different domain lengths are used for the numerical simulations. The

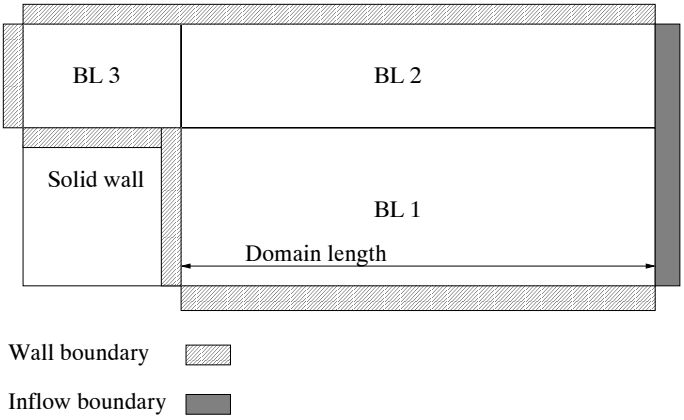

Figure 7.3: *Computational domain for wave run-up on wall*

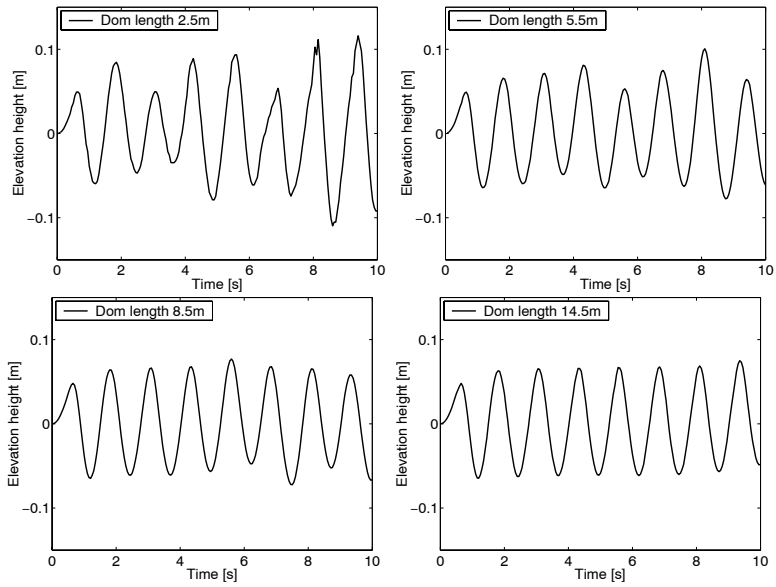

Figure 7.4: *Wave elevation measured 0.5 m from the wave generator using four grids of different domain lengths (H = 0.128 m, T = 1.256 s).*

domain length parameter is defined in Fig. 7.3. The four grids have 128×256, 256×256, 384×256 and 512×256 grid cells in Block 1, respectively, and the corresponding domain lengths are 2.5 m, 5.5 m, 8.5 m and 14.5 m. The input wave parameters of Case A, with a simple wall structure, are applied.

The resulting wave elevations in the flume from the numerical simulations are plotted in Fig. 7.4, showing that large disturbances are present at the initial stage of the tests for the grids of a small domain length, and that these disturbances decrease with increasing domain length. The generated wave length is 2.5 m, which is equal to the smallest of the domain lengths, and since these two lengths correspond the disturbance of the first generated waves will almost immediately affect the following waves, due to reflection against the wall structure. The disturbances decrease as the domain length increases, and for the highest

Table 7.2: *Four lowest order resonant wave periods for the four domain sizes. Resonant periods closest to the generated wave period ($T = 1.28s$) is indicated with a box.*

Domain length	[m]	2.5	5.5	8.5	14.5
$T_{res,1}$	[s]	1.57	3.64	5.35	9.12
$T_{res,2}$	[s]	0.79	1.73	2.67	4.51
$T_{res,3}$	[s]	0.52	1.15	1.78	2.93
$T_{res,4}$	[s]	0.39	0.86	1.33	2.38

length (14.5 m) the disturbance from the first generated waves is not yet visible. The return time of the first wave, reflected off the wall structure, is $\simeq 15$ s, which means that the wave probe for the largest domain has not yet met the (returning) first wave.

Disturbances in the domain do not only include the previous wave crests reflected from the domain boundary but also the creation of resonant waves, where the wavelength of the lowest order resonant wave (single node) is equal to twice the domain length. The resonant wave is a shallow water wave, due to the large ratio between wavelength and flume depth. From shallow water wave theory the group velocity c_g is defined as

$$c_g = \sqrt{gh}, \tag{7.1}$$

where g is the gravitational acceleration and h is the water depth. The period of the lowest order resonant wave $T_{res,1}$ is given by

$$T_{res,1} = \frac{2L_{dom}}{\sqrt{gh}}, \tag{7.2}$$

where L_{dom} is the length of the flume or the domain. For higher order resonant waves with periods equal to $T_{res,2}$, $T_{res,3}$ and $T_{res,4}$ the period is determined from an equivalent expression (Eq. (7.2)), but where the numerator on the right hand side equals L_{dom}, $\frac{2}{3}L_{dom}$ and $\frac{1}{2}L_{dom}$, respectively. For the four computational domains, the period of the four lowest order resonant waves are listed in Table 7.2. The table shows that all domains have resonant wave periods close to the period of the generated wave. And for the domain length of 8.5 m the resonance period of the second resonant wave ($T_{res,2}$) is close to twice the generated wave period, which can also excite this wave mode.

7.1.3 Comparison of Free Surface Contours for Straight Bow

The computed free surface contours for the shipping wave on top of the solid wall are shown in Figs. 7.5 and 7.6, where lines from the experimental surface contours are plotted on top. The figures show the surface contours at six different time steps, using two different computational domains, of a domain length of 8.5 m and 14.5 m respectively.

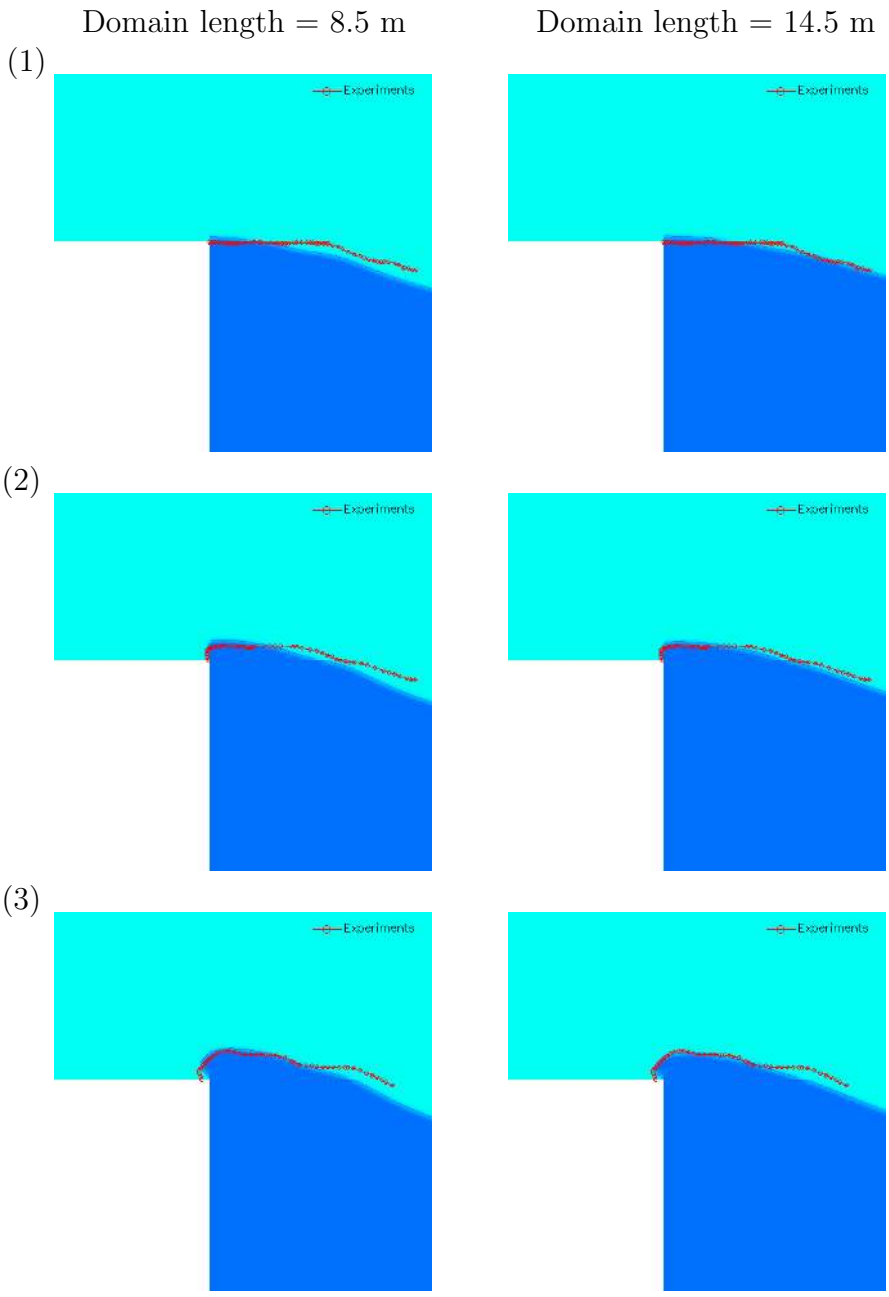

Figure 7.5: *Part 1 of wave contours on solid wall for two different domain lengths. Experimental contours shown with red. The time step between frames equals 0.04 s. Images 1-3. ($H = 0.128$ m, $T = 1.256$ s).*

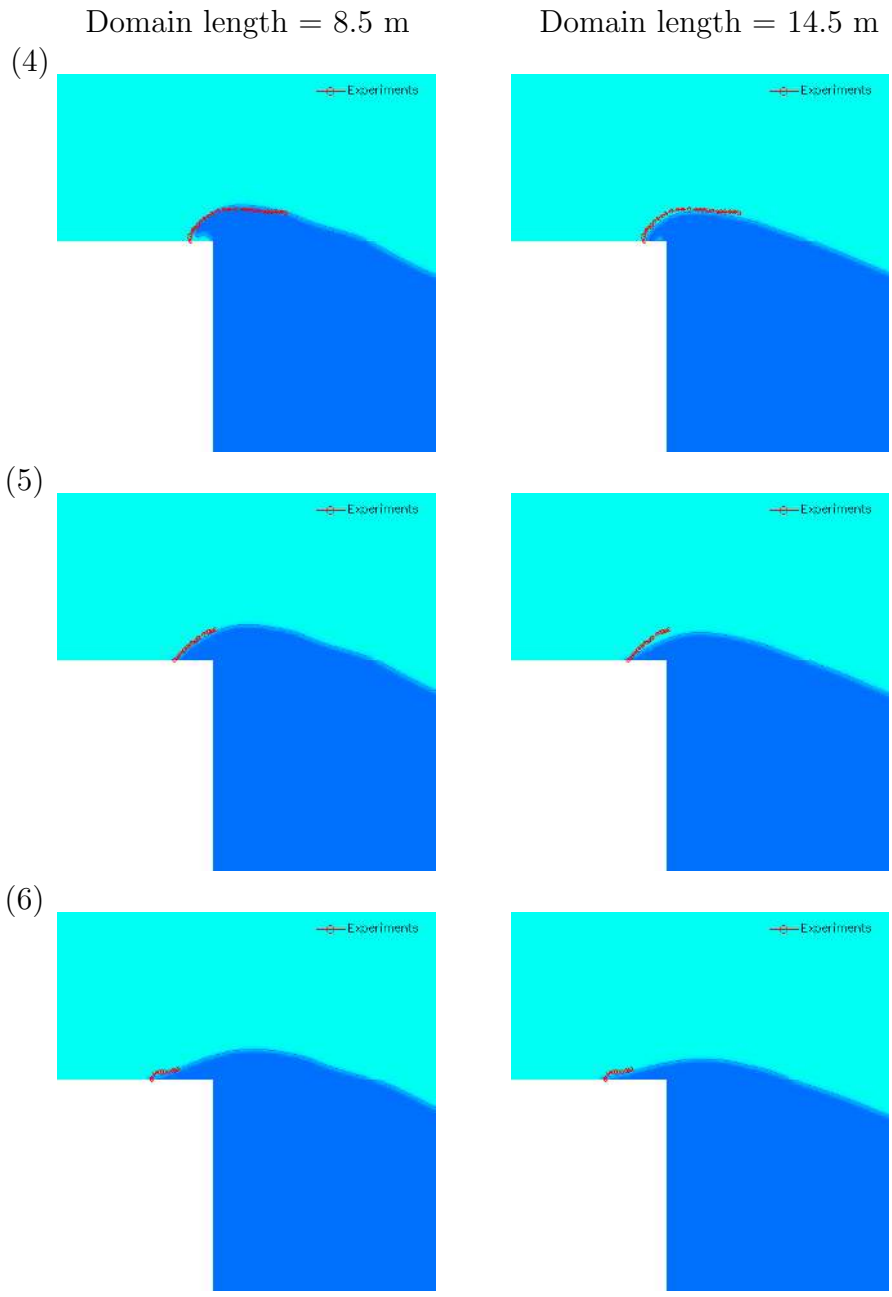

Figure 7.6: *Part 2 of wave contours on solid wall for two different domain lengths. Experimental contours shown with red. The time step between frames equals 0.04 s. Images 4-6. ($H = 0.128$ m, $T = 1.256$ s).*

The time step between each image is 0.04 s, and the contours from the computations with the 8.5 m domain are taken 10.7 s after the computations were started, while the contours from the 14.5 m domain are captured after 16.4 s.

The figures show good correspondence between computed and experimental free surface contours for both domain lengths. A small difference is observed toward the end of the shipping incident, as the magnitude of the shipping wave in the large (14.5 m) domain is slightly smaller than both the experiments and the computations from the small domain. Moreover, the experiments did not report any formation of a cavity, located at the top corner of the wall, which can be seen in the computations at steps (3) and (4).

The contours for the computed results with the 8.5 m domain are from the 6th wave component that encounters the wall, and the contours from the 14.5 m domain are from the 8th component that encounters the wall. In both cases no previous wave component shows any significant shipping water on top of the wall, which means that the previous, regular incoming waves have no significant height to overflow the wall. The waves are generated from initially still water, in which case the first (transient) waves do not have the desired wave height prescribed at the inflow boundary condition. However, after the second component the waves have the desired wave kinematics. The reason why shipping does not occur until the 6th and 8th wave component, respectively, is that disturbances from the previous wave components are required to create waves large enough to flood the top of the wall. Since it was not documented in the experiments when the free surface contours were captured, it is not possible to recreate the experiments in the numerical simulation, even if an equivalent domain length is used. The fact that disturbances in the water are required to overflow the top of the wall could explain why several different shipping wave incidents were shown in the experiments, of which each incident differed slightly.

To investigate the effect of the disturbances in general, and the resonant wave in particular, Fig. 7.7 shows the wave elevation just in front of the solid wall using the two domain lengths. It proves that the two incidents of the visualisations, using the grids with a domain length of 8.5 m and 14.5 m, respectively, are the first instances of wave elevations larger than the 0.1 m freeboard. The following wave impacts show a large scatter for the max elevation, which means that the incoming wave is disturbed by previous components as well as by the standing wave. After approximately 20 seconds the 8.5 m domain shows a large increase in wave motion, since both the maximum and minimum wave elevations rise significantly. This is caused by the returning of the first generated waves, which return (the second time) to the wall after 20 seconds. For the 14.5 m domain the returning period is 34 seconds, and because the first wave transients are not very large this return is not visible in the figure. The resonant wave periods for the two domains are 5.34 and 9.12 seconds, but it is hard to distinguish the resonant wave from other disturbances.

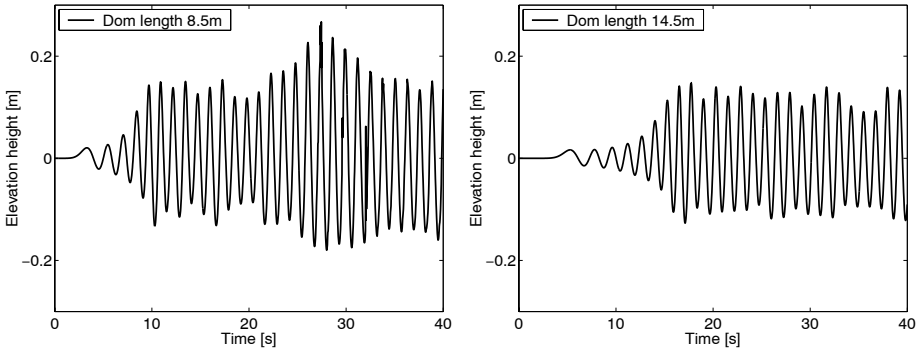

Figure 7.7: *Wave elevations 0.1 m in front of the solid wall. Two domain lengths (8.5 m (left) and 14.5 m (right)).*

7.1.4 Comparison of Free Surface Contours for Flared Bow

In Fig. 7.8 the free surface contours for the wave run-up on the solid wall with a flare structure are presented. The computational domain with of a length of 8.5 m is used. For the first image, the experimental contour is only a short line located away from the structure, because the location of the free surface near the structure was difficult to identify from the video recordings, because of spray. In the second image the experimental and computed surfaces do not show exactly the same location, but the general flow behaviour is similar. The third and fourth images show better agreement between experimental and computed results.

As for the straight wall, the computed contours are captured after 10.7 s, and in the wave encounters prior to this event, the wave run-up only shows very minor water shipping. Again, this is due to the generation of the resonant wave inside the tank and disturbances from previous waves. Visualisations using the 14.5 m domain are omitted, since they show the same correspondence as in the straight wall case, where the shipping wave is slightly smaller than in the 8.5 m domain case.

7.1.5 Conclusions to Wave Run-up Case

The purpose of the wave run-up on wall cases is to investigate initial green water loading events. The study is preliminary with regard to green water loads since the interaction effects are simplified, and furthermore the study is only 2-D. The comparisons between experimental and numerical results proved that the numerical model is able to predict the simplified green water flow.

Moreover, it can be proved in relation to green water investigation that the presence of flare in the structure significantly reduces the amount of water which is shipped onto the top of the structure. Though the general green water problem is more complex, this result is in

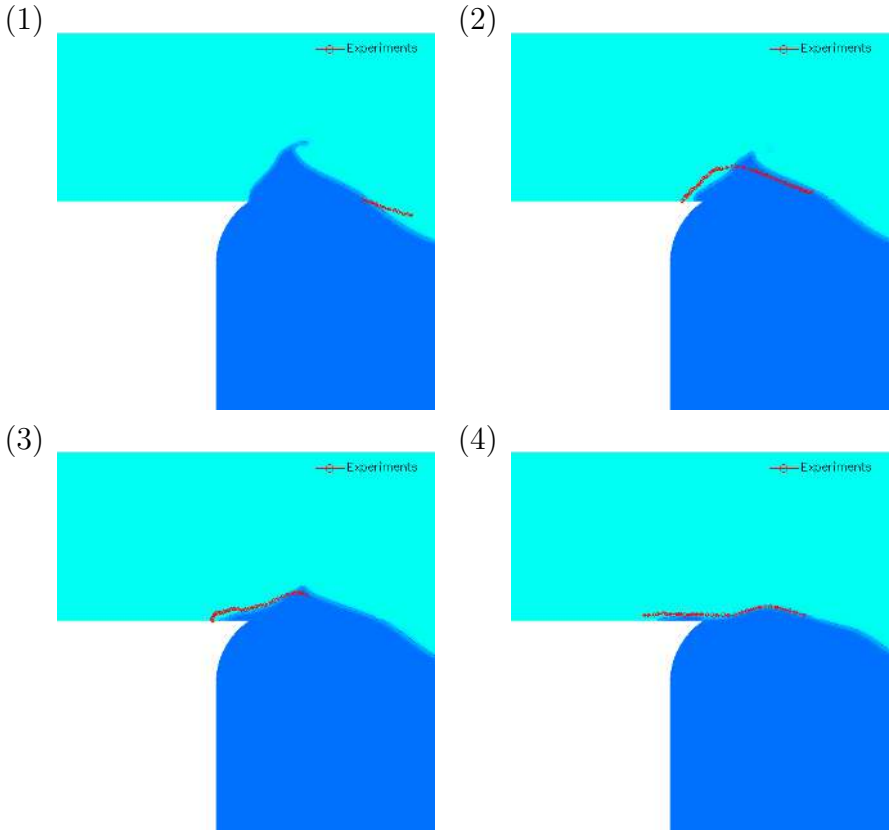

Figure 7.8: *Wave contours on solid wall with flare for a domain length equal to 8.5 m. Experimental contours shown with red. The time step between frames equals 0.04 s. ($H = 0.132$ m, $T = 1.256$ s).*

agreement with the study by Buchner and Voogt (2000), which also showed that increase in bow flare reduces the amount of water on deck.

Due to the disturbances in the flume and resonant waves, the study also focused on requirements for domain length. The shortage of information from the experiments made the reproduction of wave shipping events difficult, and to improve the numerical investigation of this type of initial green water incidents it is necessary to obtain experimental results with a better description of incoming wave kinematics and flume disturbances. The next section tries to compensate for some of the shortcomings of the present investigation by using a more realistic setup and having better control of the generated wave.

7.2 Green Water on 2-D FPSO

A further study of two-dimensional simulation of green water incidents was performed in Greco (2001). Different bow shapes were tested to investigate their effect on the shipping wave, and the flow onto deck was studied in detail. Greco (2001) also performed numerical simulation of the test cases, using a modified boundary element method with a special scheme to handle the free surface from the wave shipping at the bow of the FPSO. In this section green water shipping on a 2-D FPSO model is simulated by the NS3 model and compared to the experimental results.

7.2.1 Experimental Simulation of 2-D Green Water Loads

The experiments of the 2-D green water incidents were performed in the wave flume of the Faculty of Marine Technology at the Norwegian University of Science and Technology, Trondheim (Norway). The flume is 13.5 m long, 0.6 m wide and the water depth is 1.035 m. During the experiments a structure (the FPSO) was mounted in the flume, spanning the whole width of the flume, which ensured the two dimensionality. The FPSO structure was located 5.54 m from the wave generator. A sketch of the test setup is shown in Fig. 7.9. During the experiments the wave elevation was measured in the tank. This was done at WP1 and WP2, which were located 0.8 m and 5.436 m from the wave generator, respectively. Similarly, the wave heights on deck of the FPSO structure, resulting from the water shipping, were measured. This was done using the probes WL1, WL2 and WL3. These were located at the front end of the bow, 0.075 m and 0.15 m from the bow, respectively.

The tests were carried out by use of a simplified FPSO bow structure, with a straight vertical bow, and a small rounding at the bottom of the bow, with a radius of 0.08 m. During some of the experiments, a vertical wall was mounted on the structure, located 0.2275 m from the bow. On the wall, two pressure gauges were mounted (PR1 and PR2), 12 mm and 32 mm above the FPSO deck, respectively. The details at the bow are shown in Fig. 7.10.

A detailed discussion about the uncertainties and measuring errors during the experiments is also given in Greco (2001).

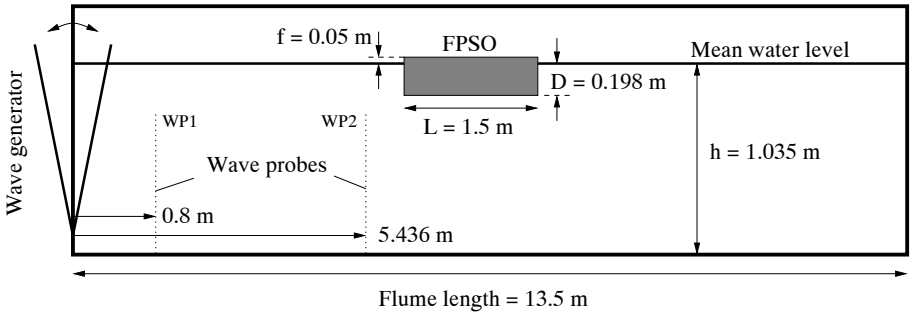

Figure 7.9: *Setup during 2-D green water tests.*

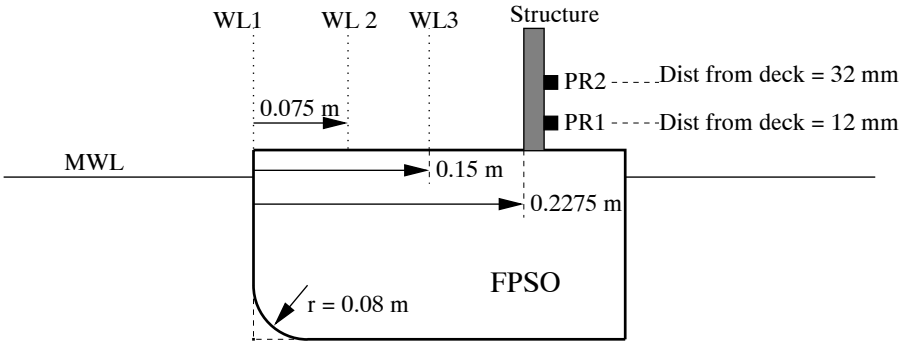

Figure 7.10: *Details around the FPSO structure*

7.2.2 Numerical Simulation of 2-D Green Water Loads

The simplified 2-D green water incidents on the FPSO are investigated numerically to determine the applicability of the model to this type of problem. The obtained numerical results are compared to experimental results obtained by Greco (2001) for verification. Before any comparisons are made, the required grid resolution will be investigated, to verify the numerical results.

Two factors must be considered before constructing the grid for the 2-D green water modelling. First, the generated waves must be modelled correctly, with corresponding wave kinematics between experiments and simulations, which requires sufficient grid cells in the domain in front of the structure. Second, once the wave encounters the FPSO a different flow pattern will form, and the involved wavelengths for the shipping wave are much smaller than the incoming wave, which requires grid cells on a smaller scale. Therefore, the effect of grid resolution will be investigated for both incoming wave kinematics and the shipping wave. The overall grid topology is given in Fig. 7.11, where the left boundary is the input (wave generation) boundary and all other boundaries are wall type boundaries.

In order to ensure that a sufficient amount of grid cells is present around the FPSO bow, the grid is stretched horizontally from the wave generator to the FPSO. A horizontal stretch factor of 15, equal to the ratio of the largest and the smallest cells, is applied to the coarse grid and a factor of 10 to the medium and the fine grids. The grids are given different stretch

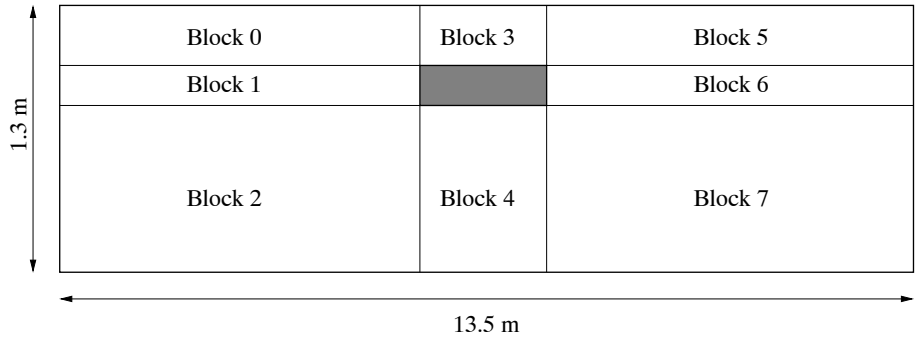

Figure 7.11: *Block distribution for numerical simulation of 2-D green water incidents.*

factors in order to have wellproportioned cells which do not differ too much in size between the different blocks, in the region near the FPSO. Similarly, the grids are stretched vertically from the domain bottom to the bottom of the FPSO to ensure a sufficient amount of grid cells on the free surface. A stretch factor of 3 is used. In Table 7.3 the grid cell resolution for the three grids used for the numerical simulation is shown. A close-up of the grid resolution

Table 7.3: *Grid resolutions for numerical simulation of 2-D green water loads ($n_{hor} \times n_{ver}$).*

	Coarse	Medium	Fine
Block 0	160×32	256×32	320×64
Block 1	160×32	256×32	320×48
Block 2	160×64	256×64	320×64
Block 3	128×32	160×32	320×64
Block 4	128×64	128×64	128×64
Block 5	128×32	128×32	128×64
Block 6	128×32	128×32	128×48
Block 7	128×64	128×64	128×64

around the FPSO bow is shown in Fig. 7.12. A rounding is applied to the FPSO structure for the experiments, and an equivalent rounding is applied to the FPSO bow bottom. Waves are generated at the left boundary and stream function theory is employed to calculate the elevation and velocity of the fluid, as described in Appendix A.

7.2.3 Verification of the Numerical Results

To verify that the numerical problem has been sufficiently resolved, the resulting wave elevations in the location of the probes are compared, by use of the three different grids. The following wave parameters are used to generate the incoming wave: wave height $H = 0.16m$, wave period $T = 1.1s$ and wavelength $\lambda = 2m$. During the start-up, a linear sinusoidal ramp function of a duration of 2 s is used to give a smooth transition from calm water. This ramping of the wave generation helps to avoid the generation of unwanted transient waves.

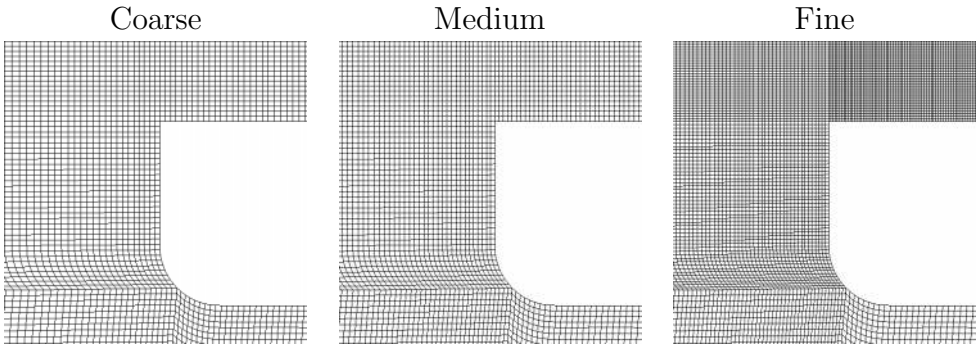

Figure 7.12: *Grid resolution around 2-D FPSO bow.*

The resulting wave elevations at probes WP1 and WP2 are presented in Fig. 7.13, obtained by the three different grids. The figure shows that only very little difference is visible between the grids, and that only the coarse grid has a little deviation from the results obtained by the medium and the fine resolution grids. This means that for the incoming wave, the grid resolution is satisfactory. It may be added that in the coarsest part of the grids, near the wave generator, the number of grid cells in the horizontal direction per wavelength is equal to 24 for the coarse grid, 50 for the medium grid and 54 for the fine grid.

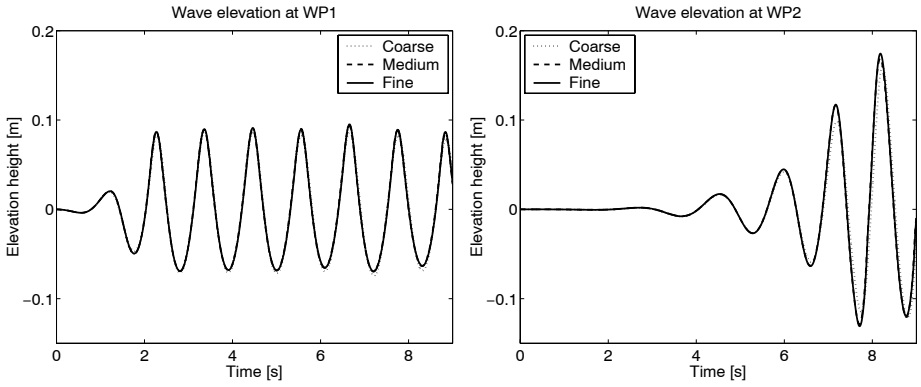

Figure 7.13: *Wave elevation at WP1 (left) and WP2 (right) from numerical simulations using three grids ($H = 0.16$ m, $T = 1.1$ s, $\lambda = 2$ m).*

The resulting wave height on deck of the FPSO, by use of the three different grids, is given in Fig. 7.14. It shows water shipping for two wave impacts, of which the second impact is significantly larger than the first. The difference between the grids is more visible, but the results from the medium and the fine grids still give almost identical results. The probes exhibit a clearly decaying behaviour, as the first probe WL1 measures the largest water height and the following two probes show decreasing maximum water height.

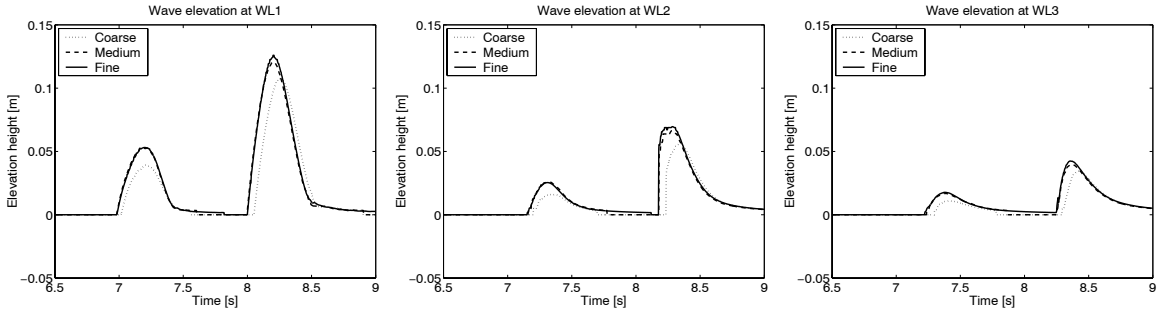

Figure 7.14: *Wave elevation at WL1 (left), WL2 (centre) and WL3 (right) from numerical simulations using three grids ($H = 0.16$ m, $T = 1.1$ s, $\lambda = 2$ m).*

7.2.4 Comparison of Experimental and Numerical Visualisations

Visualisations from experiments and computations, for the first shipping incident, are compared in Fig. 7.15. It shows the free surface contours at the initial impact, where the incoming wave encounters the ship's bow and an overturning wave is formed, which breaks onto the deck and forms a water front that travels along the deck. The agreement between experimental and computed free surface contours is very good. The largest discrepancy between the results is seen in image 3, where the breaking wave encounter the FPSO deck. The experimental wave front seems more rounded than the computed one, and the latter seems to be a small time step ahead of the first. There may be two causes of this: first, the numerical model does not include surface tension, which could add more curvature to the interface, and second, it is difficult to match the time series exactly, since the experimental images are not matched with probe measurements, which could help identify the exact timing of the incident. At the end of the incident (image 5), the computed wave seems slightly smaller than the experimental one. However, in the background, two black double lines are observed, against the white plate. These are the wave probes WL1 and WL2, and measurements from the probes will clarify whether there is any difference between computed and experimental water heights on deck.

In particular it should be noted from the visualisations that a cavity is formed on the front of the FPSO deck. Both the size and the duration of the cavity are well predicted in the computations, and contrary to the formation of the cavity in the "wave run-up on wall" case (Section 7.1), this cavity is also seen experimentally. Greco (2001) reported that the formation of the cavity clearly was a two dimensional phenomenon, which formed all along the width of the structure. These experiments used a special fluorescent dialute to enhance the free surface contour. The experiments for the wave run-up case, performed by Cozijn (1996), did not apply this technique, which could have made it more difficult to identify the existence of the cavity.

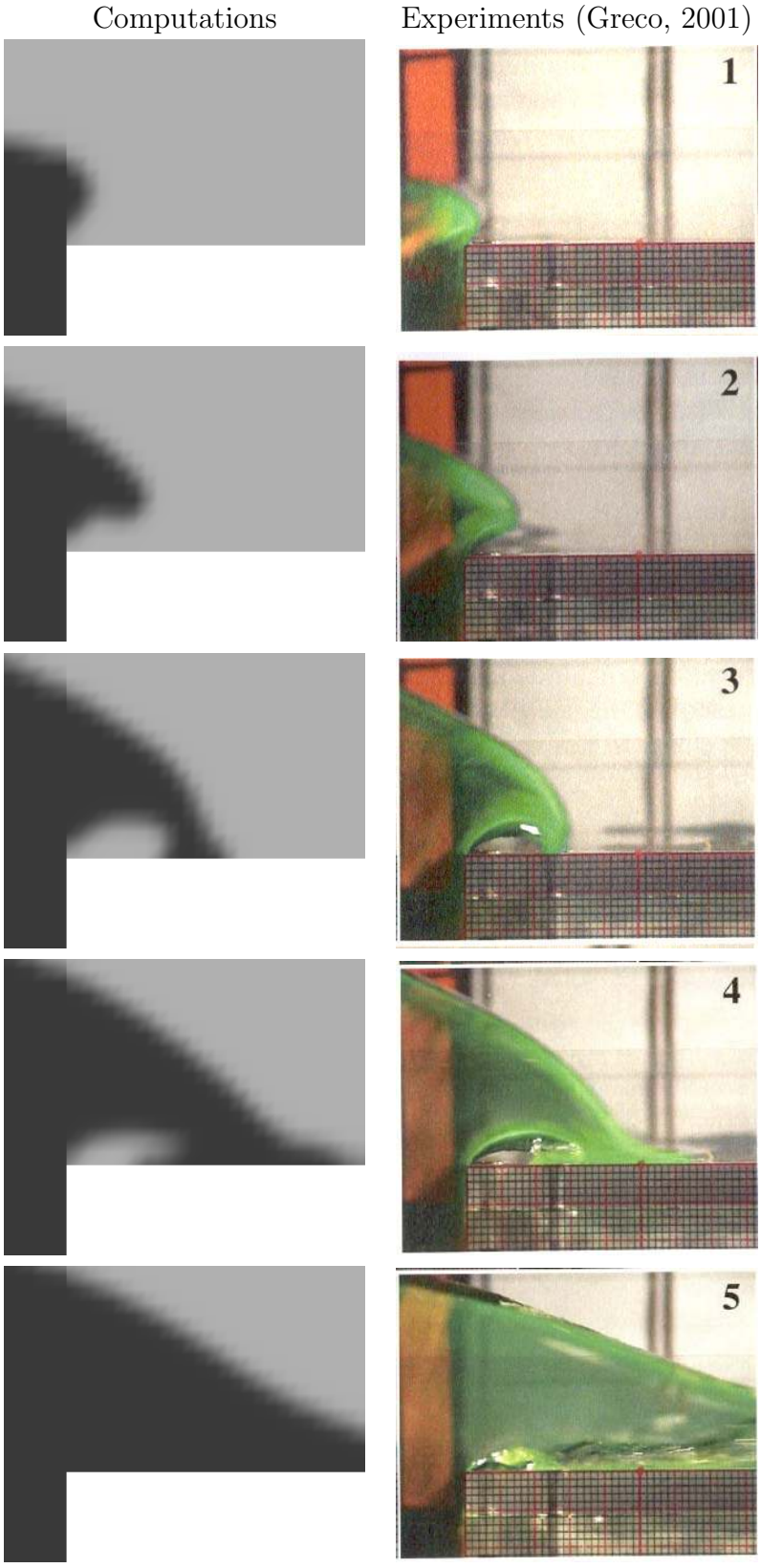

Figure 7.15: *Visualisation of shipping wave on the FPSO deck. The computations employ the fine grid of Table 7.3. The smallest grid scale shown in the experiments is 2mm. $H = 0.16$ m, $T = 1.1$ s, $\lambda = 2$ m.*

7.2.5 Wave Kinematics and Resulting Wave Height on Deck

To validate the computed incoming wave kinematics against the experimental probes, the elevations measured at probes WP1 and WP2 are shown in Fig. 7.16. It is seen that the wave crests of the initial wave transients are not exactly matched between experiments and computations for probe WP1, but that the disagreement is small. During the rest of the time series, and especially after the wave transients, the agreement is good. At probe WP2, which is located further into the domain from the wave generator, the difference between experiments and computations is even smaller. It is observed that the resulting wave height at WP2 after the first two waves is larger than at probe WP1. This is due to reflection of the first wave components against the FPSO structure, which is located only 0.1 m from the probe.

The difference in wave transients for WP1 could be caused by the wave absorption system, which was an integrated part of the flap type wave generator used in the experiments. This active absorption system was used to cancel out any unwanted (resonant) wave components, but details of how the absorption system works were undisclosed. However, the flap signal concerned was listed as part of the experimental results. As a test, this signal was used to generate waves in the computational domain, to try to generate waves of exactly the same type as in the experiments. The flap movement was transformed into a flux type boundary condition and applied to the inflow boundary in the computational domain. However, because only a flux condition was applied, and not the actual movement of the flap, this type of wave generation did not give better results, on the contrary, the generated wave differed more than the normal wave generation, even though only slightly. Details of this test are shown in Appendix B.

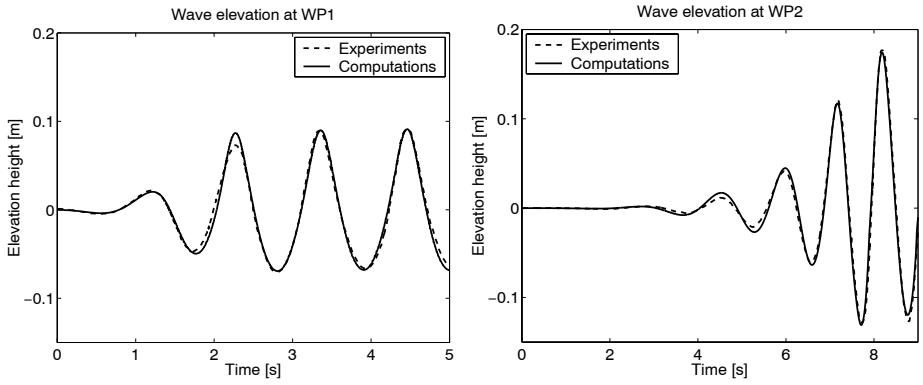

Figure 7.16: *Comparison of wave kinematics at wave probes WP1 (left) and WP2 (right) for experiments (Greco, 2001) and computations (fine grid). $H = 0.16$ m, $T = 1.1$ s, $\lambda = 2$ m.*

A comparison of the resulting water height on deck at the three probes WL1, WL2 and WL3, located at the front of the FPSO deck, is seen in Fig. 7.17. Probe WL1 shows very fine agreement between computed and experimental results the first shipping wave occurring at $t \simeq 7s$ is slightly overpredicted by the computations and the second wave is an exact

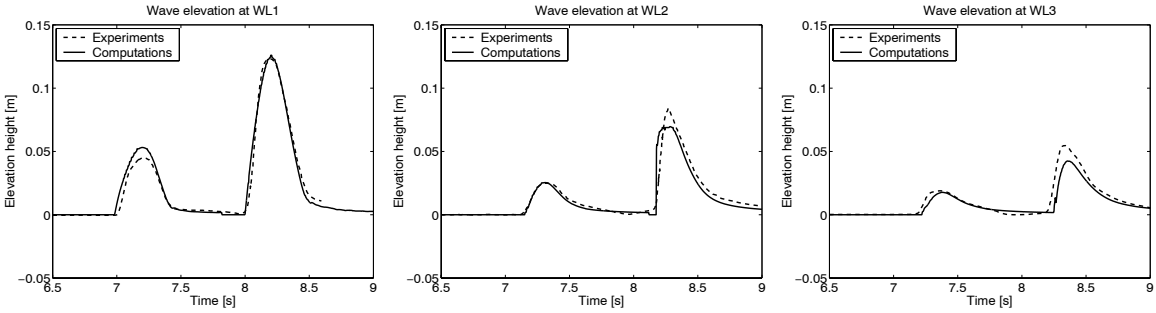

Figure 7.17: *Resulting water height on deck, measured at probes WL1 (left), WL2 (centre) and WL3 (right). Experiments by Greco (2001), the computations applied the fine grid (Table 7.3). $H = 0.16$ m, $T = 1.1$ s, $\lambda = 2$ m.*

match. At the second probe (WL2) the first wave seems to have decreased relative to the experimental one, so that these two now correspond, and the second wave is now slightly smaller and more rounded at the top, in the computations. And further down the FPSO deck, the probe WL3 exhibit the same behaviour. Here the first wave in the computations has dropped slightly below the experimental value, and the second wave is also smaller in the computations. A reason for this behaviour, where both the first and the second shipping waves decay faster in the computations than in the experiments could be the initial wave generation. From the probes WP1 and WP2 it is clear that the initial wave transients are not identical for experiments and computations. These transient components are not the waves which cause the actual shipping, they come from consecutive waves. However, the wave transients are reflected against the FPSO structure and return toward the wave generator, which could cause the following wave components to lose energy. This might explain why the shipping waves does not sustain the same energy as the experimental ones.

7.2.6 Impact on Structure

A structure is now added to the FPSO, located on the fore part of the deck, 0.2275 m from the bow (see Fig. 7.10), on which two pressure gauges are used to obtain a pressure time series. In Fig. 7.18 the pressure time series for the two pressure probes (PR1 and PR2) are shown for both experimental pressure, obtained by Greco (2001), and the presently computed pressure. For both probes two significant peaks occur, the first is the result of the initial impact, and the second appears when the water front begins to run down from the wall, after having reached the maximum. During the experiments, the test was repeated several times to investigate the reproduction of the data. These tests revealed that the exact same result could not be obtained, though the pressure level and the pattern of the pressure time history were very similar. The magnitude of the differences between the different repetitions was in the order of 10 % and maybe slightly more for peak values. As in the dam break problem (Chapter 4) this can be explained by the non-deterministic nature of the pressure incident,

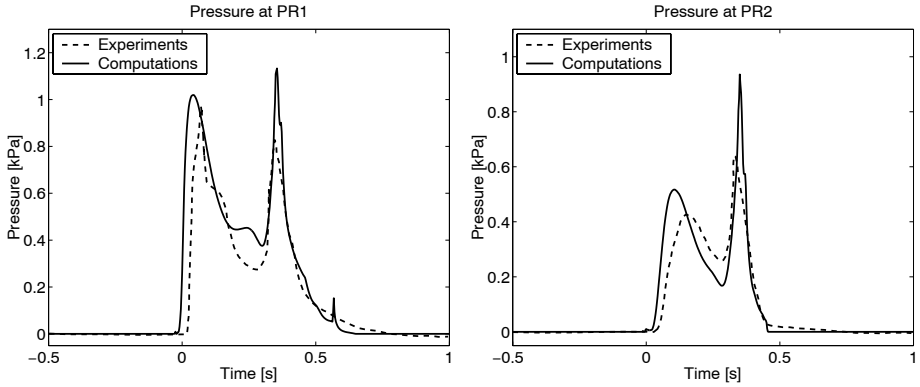

Figure 7.18: *Resulting pressure at probes PR1 and PR2 located on structure on FPSO deck. Experiments by Greco (2001), the computations applied the fine grid (Table 7.3). $H = 0.16$ m, $T = 1.1$ s, $\lambda = 2$ m.*

which occurs a while after the start of the experiment. Moreover, small differences in initial conditions can result in a change in outcome. With this in mind, the comparison between computed and experimental pressures shows good agreement, though the computed pressure seems to overestimate the pressure peaks to some degree. Both the overall pressure level and the evolution of the pressure time history with the two peaks are well predicted numerically. It may be added that the threedimensionality of the experiments was investigated in Greco (2001) by using two pressure gauges at the same vertical level as PR1 but in a different cross ship locations. This test also gave slightly different pressure time series, but the variation between the two probes was the same order of magnitude as seen in the repeatability tests.

7.2.7 Conclusions to 2-D Green Water Incidents on an FPSO

This section demonstrates the application of the numerical model to simplified 2-D green water incidents on an FPSO type structure. Two major approximations were made from real green water incidents to the present investigation. The first simplification was the application of 2-D modelling. In reallife applications the bow geometry, i.e. flare and deck curvature, influence the shipping wave as described in Chapter 1. The second approximation was the neglect of the ship motion. The ship affects the dynamics since the FPSO moves relative to the wave, and the relative motion is the primary factor in most current methods for determining green water loads. However, as a study of the physics related to green water shipping and green water impact on deck structures, the present investigation targets the primary details of shipping water and impact on deck mounted structures. The visual investigation shows that the numerical model clearly predicts the formation of a cavity at the corner of the FPSO bow, as was seen in the experiments. The shipping of the wave, and the formation of a travelling wave were also in good agreement between the computations and the experiments. The quantitative comparison of the water level on deck, measured

by deck mounted probes, also shows very good correspondence between experiments and computations. As in the case of the impact on a deck mounted structure, the numerical model also showed that it was capable of predicting correctly both the pressure level and the evolution of the pressure history. From this, it is concluded that the numerical method possesses promising features as regards the possibility of numerical prediction of green water loads. In the following chapter the complexity of the green water incidents will be increased by applying 3-D modelling, and simulation of the relative wave motion will also be included.

Chapter 8

Green Water Load on an FPSO

So far the green water investigation has concentrated on simplified flow problems with green water loads, such as dam break and cylinder impact (Chapter 4) related to the water flow on deck and impact on deck structures as well as simplified 2-D green water incidents (Chapter 7), where relative motions are neglected. In this chapter the complexity level of the green water incident modelling will be increased to include the relative ship motion, and the problem will also be investigated in three dimensions. This extension requires two elements not previously introduced: relative ship modelling and 3D computations. Modelling the relative wave motion will be discussed and tested in detail, but the 3-D computational model is a trivial extension to the 2-D model which was introduced in Chapter 2 and will not be described further. In Chapter 1 an introduction is given to related work including other numerical investigation of green water events.

For validation of the numerical results, model experiments by Buchner (1995a) will be used. The next section introduces the experimental setup and discusses the relevant parameters with regard to the numerical modelling.

8.1 Green Water Experiments

Experimental modelling of green water incidents on an FPSO was presented in Buchner (1995a) and further analysed in Buchner (1995b). The main dimensions of the full size FPSO are given in Table 8.1, and the experiments were conducted on a scale of 1:60. The water depth during the experiments was equal to 150 m. The bodyplan of the FPSO is shown in Fig. 8.1, which corresponds to the bodyplan of the ship with flare, as given in Buchner (1995a).

During the experiments the FPSO bow was equipped with water height and pressure gauges to obtain time histories of the water flow on deck and the green water induced pressure.

Table 8.1: *Main particulars for FPSO*

Length	260.34 m
Beam	47.10 m
Draught	17.52 m
Freeboard	8.88 m
Depth	26.40 m
Displacement weight	183,053 t

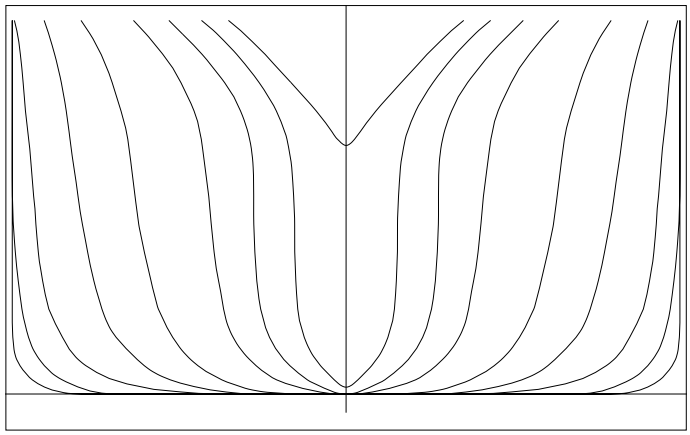

Figure 8.1: *Bodyplan of FPSO*

In the current investigation only the results of the water height on deck will be used. In Buchner (1995b) the resulting water height on the deck at two probes (entitled H8 and H6 in the paper) was reported. These two probes correspond to locations 4.2 m and 9.4 m aft of the bow of the FPSO, in the centerline of the ship. For simplicity these two locations will be denoted H1 and H2 in the following.

The experimental test series included both regular and irregular waves but here only the regular wave results are used. During the experiments the forward (surge) motion of the vessel was restricted by a vertical cylinder with roller bearings, attached to the FPSO model through the centre of gravity of the model. This simulates the mooring system of a real life FPSO. The heave and pitch motions were not restricted, which also corresponds well with real life applications since the mooring system has very little effect on the vertical dynamics of the vessel.

From the experiments a single (regular) wave incident, with the wave period $T = 11.2$ s and the wave height $H = 17.3$ m, will be compared with the present numerical simulation of green water loads. The corresponding wavelength (λ) is 209.5 m and the FPSO length (L) is equal to 260.34 m, which corresponds to wavelength - ship's length ratio[1] $\lambda/L = 0.80$.

[1]In Buchner (1995a) the wavelength - ship's length ratio was stated to be 0.75. This is the case when linear (Airy) theory is applied to the computation of the wavelength, which gives $\lambda = \frac{gT^2}{2\pi}$. However, due to

8.2 2-D Numerical Prediction of Green Water on Deck

The experimental data described in the previous section was obtained using a floating ship model and the experiments included all the complicated phenomena such as relative wave motion, ship motion and three dimensionality of the structure, described in Chapter 1. The most difficult interaction problem to model numerically is the relative motion of the ship, including the actual ship response, which results from the ship - wave interaction. Full modelling requires threedimensional computations with moving meshes, to track the actual movement of the ship, coupled with equations of motion for the ship. Though this type of interaction has previously been presented using a CFD code (Repetto, 2001), it is computationally very expensive. In the last section of this chapter (Section 8.3), 3-D modelling of a green water incident will be investigated. However, both for simplicity and in order to be able to distinguish between 3-D effects and other interaction phenomena, the problem will initially be investigated by use of a 2-D model. The difference between 2-D and 3-D results will be discussed in Section 8.3.

A simplified type of relative motion modelling is introduced where the vertical motions of the vessel, i.e. heave and pitch motions, are modelled by closed-form expressions for the transfer functions for the ship motion, using a formulation presented by Jensen *et al.* (2003). The vertical motion can be transformed to the computational domain by changing the mean water level by use of a velocity boundary condition at the bottom boundary of the domain. Fig. 8.2 shows a sketch of the principle used for the relative motion modelling. It should be noted that the actual pitch motion is not included in this model, since only translatorial vertical motions can be included. However, the pitch contribution to the vertical motion at the bow is modelled. Before the relative motion model is tested, a brief introduction to the closed-form transfer functions is given.

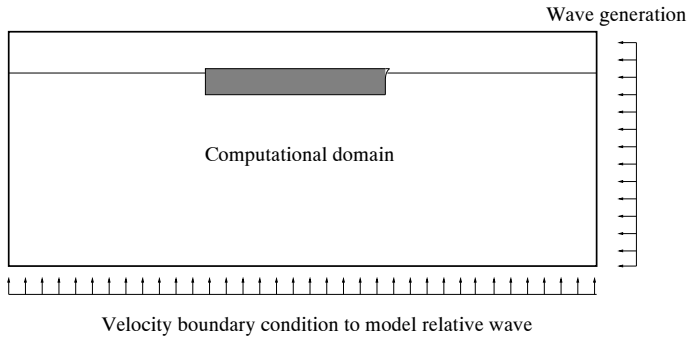

Figure 8.2: *Sketch showing the principle of relative motion modelling in the computational domain. Regular wave generation from the right boundary and relative motion (velocity) boundary condition at the bottom of the domain. The vessel is fixed in the domain.*

the large wave height, linear theory is not applicable and with stream function theory the wavelength equals 209.5 m.

8.2.1 Closed-form Transfer Functions

The vertical wave induced response of a vessel is given by the heave $w(t)$ (vertical translation) and pitch $\theta(t)$ (rotation about the y-axis) components resulting from an incoming wave with the wave elevation $\zeta(x,t)$. For linear (Airy) wave theory, the wave elevation is given by

$$\zeta(x,t) = a\cos(k(x - x_{\text{bow}}) + \omega t), \tag{8.1}$$

where a is the wave amplitude, ω is the wave number, t is time and x is measured from the centre of gravity. The heave and pitch motion response of the vessel resulting from the incoming wave (Eq. (8.1)) is given as

$$w(t) = a\Phi_w \cos(\omega t + \xi) \tag{8.2}$$

$$\theta(t) = a\Phi_\theta \sin(\omega t + \xi) \tag{8.3}$$

where Φ_w and Φ_θ are the transfer functions for heave and pitch, respectively, and ξ is the transfer function phase angle. The 90^o degrees phase lag between heave and pitch is a consequence of the assumption found in Jensen *et al.* (2003). The total vertical motion $r_z(t)$ in the bow section location x_{bow} is found by adding the two response components:

$$r_z(t) = w(t) - x_{\text{bow}}\theta(t) \tag{8.4}$$

valid for small θ angles. The pitch contribution is subtracted from the heave contribution, since the pitch angle is defined as a rotation where a positive pitch results in a motion in the negative z-axis direction for positive x.

The traditional method for determining the transfer functions of a vessel is by use of strip theory (Salvesen *et al.*, 1970), dividing the vessel hull into a number of 2-D hydrodynamically uncoupled cross sections, for which the response to the incoming wave is computed individually. This method has been simplified by Jensen *et al.* (2003), assuming a homogeneously loaded, box-shaped vessel for which the transfer functions have been derived analytically and for zero forward speed and head sea take the form

$$\Phi_w = \eta F_T \tag{8.5}$$

$$\Phi_\theta = \eta G_T \tag{8.6}$$

where

$$\eta = \left(\sqrt{(1-2kD)^2 + \left(\frac{A_{\text{hyd}}^2}{kB}\right)^2} \right)^{-1}, \tag{8.7}$$

with k equal to the wave number ($k = \frac{2\pi}{\lambda}$, λ = wavelength), B and D equal to breadth and draught of the box, and A_{hyd} equal to the sectional hydrodynamic damping amplitude given by the following approximation:

$$A_{\text{hyd}} = 2\sin\left(\frac{1}{2}kB\right)\exp\left(-kD\right). \tag{8.8}$$

Table 8.2: *Parameters for heave and pitch transfer functions.*

η	2.3782
G_T	0.001219
F_T	-0.06594
ξ	-1.3
x_{bow}	130 m

The two forcing functions F_T and G_T, from Eqs. (8.5) - (8.6), are determined from

$$F_T = \kappa f \frac{2}{kL} \sin\left(\frac{kL}{2}\right) \tag{8.9}$$

$$G_T = \kappa f \frac{24}{(kL)^2 L} \left(\sin\left(\frac{kL}{2}\right) - \frac{kL}{2}\cos\left(\frac{kL}{2}\right)\right) \tag{8.10}$$

where the Smith correction factor κ is given by

$$\kappa = \exp(-kD). \tag{8.11}$$

The transfer function phase ξ in Eqs. (8.2) - (8.3) can be determined as

$$\xi = \arccos\left[\frac{1-kD}{f}\right] + \arccos\left[(1-2kD)\eta\right] - kx_{\text{bow}} \tag{8.12}$$

where f is defined as

$$f = \sqrt{(1-kD)^2 + \left(\frac{A^2_{\text{hyd}}}{kB}\right)^2}. \tag{8.13}$$

For the present vessel with main particulars listed in Table 8.1, the parameters determining the transfer functions are listed in Table 8.2. Since the required vertical motion is at the bow of the FPSO, the location used to estimate the vertical movement caused by the pitching motion (Eq. (8.4)), is set to $x_{\text{bow}} = 130m$, equal to the bow location measured from the c.o.g. of the FPSO. The wavelength used to determine the wave number k is 209 m, corresponding to the wave kinematics used in the experiments, where the wave height was 17.3 m and the wave period was 11.2 s.

In Fig. 8.3 the transfer functions, computed by Eqs. (8.5) - (8.6), are shown for the x_{bow} location with the incoming wave crest also located at x_{bow}. The responses are shown for a duration of one wave period and are given for a coordinate system with origin in the mass centre of the vessel. Thus a negative response corresponds to a decrease in freeboard when the relative motion model is applied. It must be added that for the current wave height of 17.3 m linear wave theory no longer applies, due to the high wave steepness ($H/\lambda \simeq 0.083$), but as an approximation to the vessel motions it will serve as a good first approximation

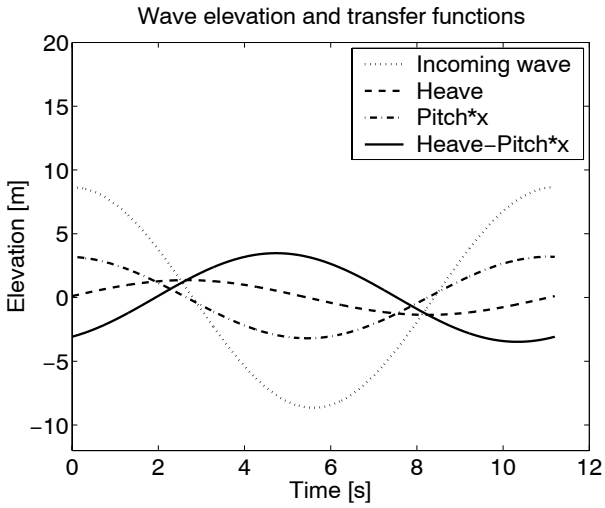

Figure 8.3: *Incoming wave and vessel response using transfer functions computed in the bow location ($x_{\text{bow}} = 130$ m).*

and the actually incoming wave will be modelled correctly in the computational domain. Further, in Jensen *et al.* (2000) it was shown that the nonlinearities in steep waves have very little effect on vertical motions (i.e. heave and pitch).

Fig. 8.3 shows that the absolute vertical motion of the vessel (at x_{bow}) is close to a minimum at the time when the incoming wave has a maximum. This results in a large relative wave height and it is therefore expected to add a significant increase in wave height on deck of the vessel, when the relative motion model is included in the numerical simulation.

8.2.2 Verification of Numerical Results

Two main tasks need verification before any validation against experimental data can be conducted. First, the relative motion model must be tested in order to investigate whether this type of modelling is applicable. Second, the required resolution for modelling 2-D green water incidents will be investigated. When these tests are completed, the resulting water height on deck for the 2-D computations will be compared to experimental data for validation.

In Fig. 8.4 a sketch of the computational domain used for the 2-D FPSO simulations is shown. The computational domain is divided into eight blocks and the block numbers indicated in the figure are used for reference, when the resolution of the computations is investigated.

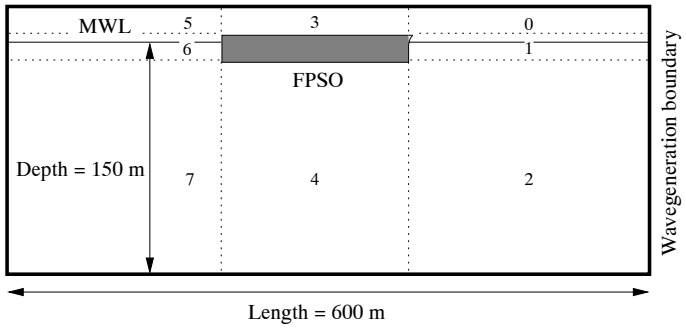

Figure 8.4: *Sketch showing the computational domain for the 2-D FPSO computations. Small numbers indicate block number. Block boundaries shown with dashed lines.*

8.2.3 Test of Relative Motion Model

In the first test, the influence on the generated wave by the relative motion model is investigated. The FPSO structure in the computational domain is removed for this test in order to investigate the incoming wave kinematics, without disturbance from the structure. The grid consists of a single block, with 320×128 grid cells, which is sufficient to resolve the approximately three wavelengths which the full domain can contain. In Fig. 8.5 the wave elevation in the x_{bow} location (if the FPSO structure had been present) is compared for two tests, one with relative motion modelling and one without relative motion modelling. The relative motion model, which corresponds to a vertical displacement of the mean free surface, is also shown in the figure. It is obtained in a test where an incoming wave is not generated, but only the velocity boundary condition at the bottom is applied. It is further noted that the peak of the relative motion occurs slightly before the crest of the incoming wave. This is in accordance with the time series of the combined (heave and pitch) transfer function shown in Fig. 8.3, which also occurs slightly before the crest of the incoming wave. In Buchner (1995a) the relative wave height was measured just in front of the FPSO bow and the maximum relative elevation was stated to be 17.9 m. In Fig. 8.5 the relative wave elevation can be obtained directly from the figure, since the relative motion is seen from a vessel fixed coordinate system. Here the maximum elevation is seen to be approximately 14 m. However, in the computed result the FPSO structure is not present, i.e. the swell-up of water in front of the FPSO bow is not included, which means that these two results can not be directly compared.

The nominal maximum crest elevation is equal to 9.89 m and the nominal wave trough is at -7.41 m, computed by stream function theory (Fenton, 1988). These values correspond to the crest and trough values of the second generated wave in Fig. 8.5 in the case without relative motion modelling, with max elevation at the time equal to approximately 32 s. Hence when the green water modelling is investigated numerically, this is the wave crest corresponding to the (nominal) incoming wave kinematics in the experiments, and the water height on deck resulting from this wave crest will be compared with experimental results.

To investigate whether the application of the relative motion model influences the generated

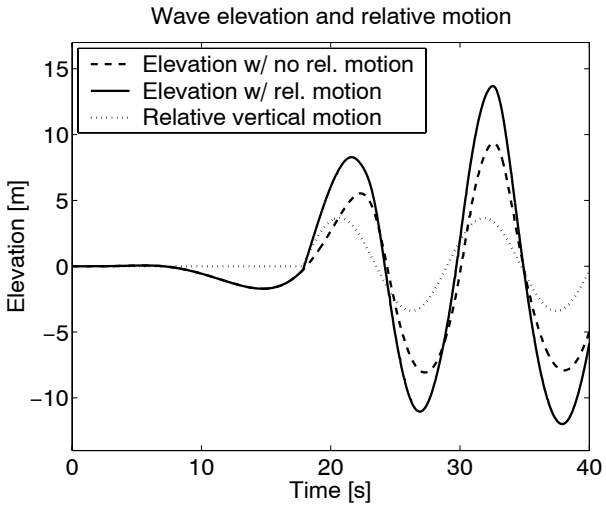

Figure 8.5: *Wave elevation in the x_{bow} location, computed without presence of FPSO structure in the computational domain. The elevation is shown for two cases, one with and one without relative motion modelling (two solid lines). The relative motion for the case where relative modelling is applied is also shown (dashed line). $H = 17.3$ m, $T = 11.2$ s.*

wave, the two elevations shown in Fig. 8.5 are plotted in Fig. 8.6, but here the displacement of the free surface is subtracted from the wave elevation in the case where the relative motion is applied. A small difference is observed for the second wave crest, which might be ascribed to a disturbance created in the domain due to the relative motion model, but the difference in wave height between the two computations is in the order of 5 % of the total wave height, which is an acceptable disagreement. In general the figure shows that the generated wave corresponds well in the two cases, which means that the application of the relative motion model has no significant effect on the wave generation.

8.2.4 Grid Resolution Test

The green water incident is investigated by use of three different grids with increasing resolutions. Table 8.3 shows the resolutions of the three grids where the block numbers correspond to the blocks indicated in Fig. 8.4.

The resulting water height on deck, by use of the three grids outlined in Table 8.3, is shown in Figs. 8.7 and 8.8. The figures include results obtained both with and without application of the relative motion model. Regarding the grid resolution both figures give similar results for all three grids. Small differences are observed for the peak of the water height, especially in Fig. 8.7 for the case without application of relative motion modelling. This is not expected to be due to underresolution in the computations, but rather to the fact that the dynamics of the shipping water flow is so sensitive to initial conditions that the small changes resulting from increasing the grid resolution affects the flow and variations in the water height on

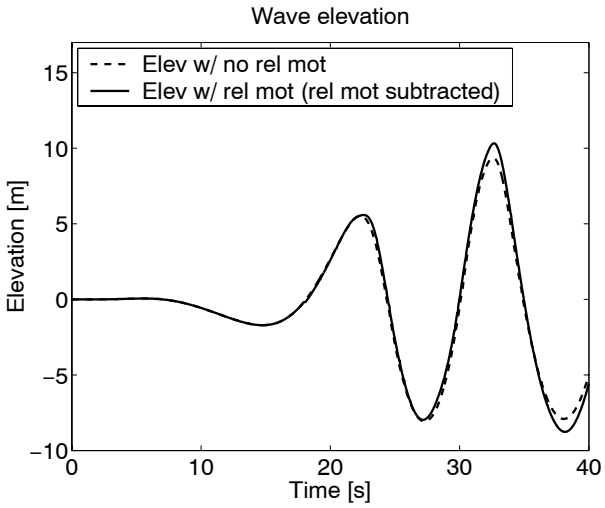

Figure 8.6: *Wave elevations from Fig. 8.5. The magnitude of the relative motion is subtracted from the wave elevation for the case where the relative motion model is applied.*

Table 8.3: *Grid resolutions for numerical simulation of 2-D green water loads with relative motion modelling ($n_{hor} \times n_{ver}$). Grid topology is shown in Fig. 8.4*

	Coarse	Medium	Fine
Block 0	96×32	160×48	224×64
Block 1	96×32	160×48	224×64
Block 2	96×64	160×48	224×64
Block 3	128×32	192×48	320×64
Block 4	96×64	160×48	224×64
Block 5	32×32	64×48	96×64
Block 6	32×32	64×48	96×64
Block 7	32×64	64×48	96×64

deck may be caused by numerical inaccuracies. However, generally the difference between the results for the three grids is small.

Regarding the magnitude of the resulting water height on deck, it is clear that the application of the relative motion model increases the water height on deck, as expected. Further, it is shown that the resulting water height is significantly larger at the first probe (H1) than at the second probe (H2). Whether the magnitude of the resulting water height on deck corresponds to the experimentally measured results will be investigated later. First, a visualisation of the wave shipped on the deck will be shown for the two cases for discussion of the flow features connected with the green water incident.

Regarding CPU time it can be noted that the computation time for the full simulation (until $t = 40\ s$) is 1 hour for the coarse grid and 7.2 hours for the fine grid, on a single processor 1.2 GHz P3 computer.

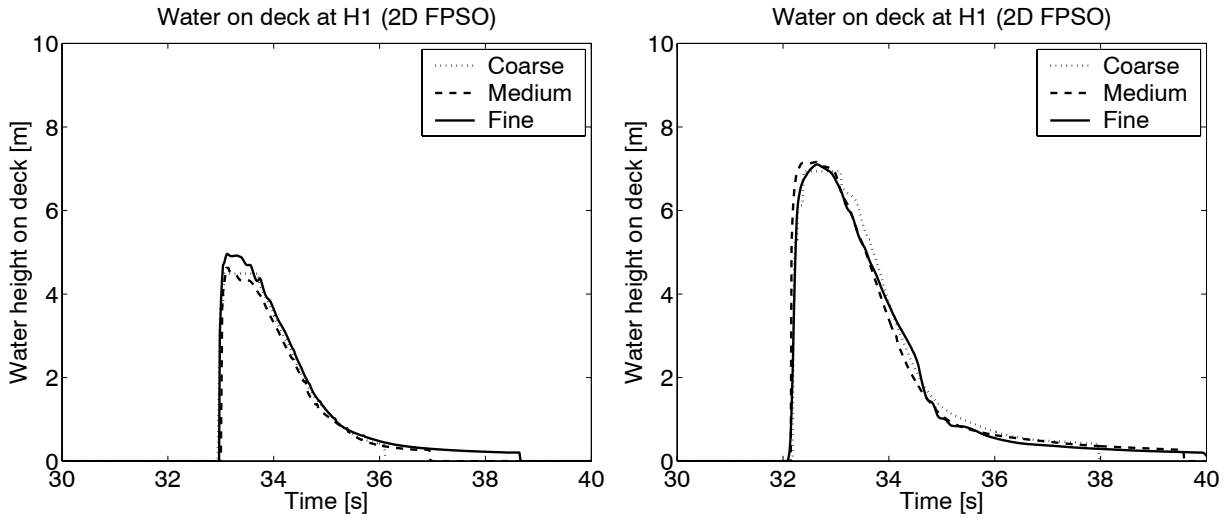

Figure 8.7: *Resulting water height on deck at probe H1 for the 2-D FPSO case, using the three grids described in Table 8.3. In the left figure only regular wave generation is applied, and in the right figure both regular wave generation and the relative motion model are applied. $H = 17.3$ m, $T = 11.2$ s.*

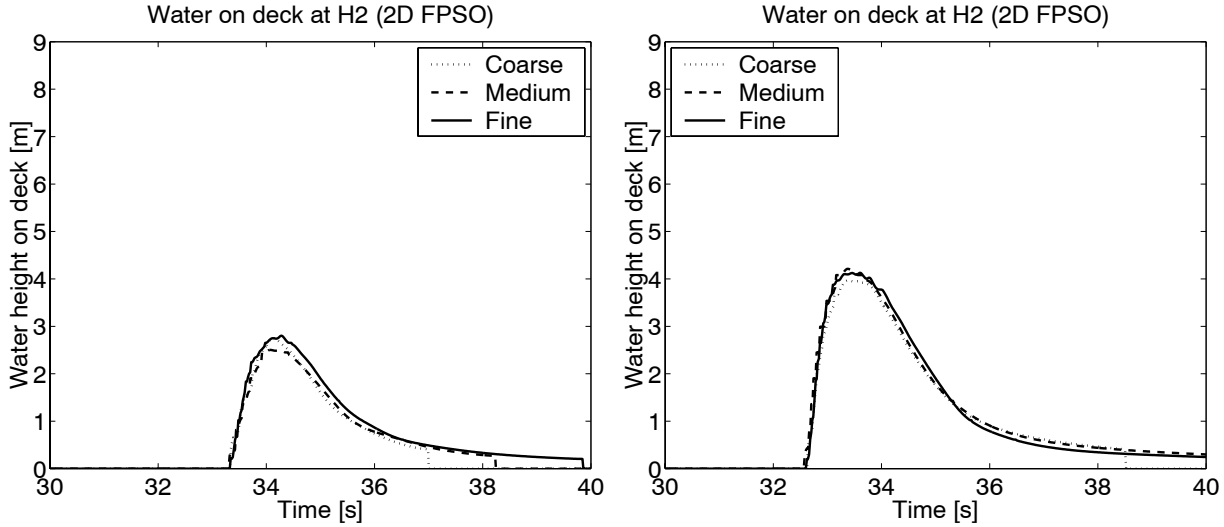

Figure 8.8: *Resulting water height on deck at probe H2 for the 2-D FPSO case, using the three grids described in Table 8.3. In the left figure only regular wave generation is applied, and in the right figure both regular wave generation and the relative motion model are applied. $H = 17.3$ m, $T = 11.2$ s.*

8.2.5 Visualisation of the Shipping Wave in the 2-D FPSO Case

The free surface contours of the 2-D green water shipping event with and without relative motion modelling are shown in Fig. 8.9. The shipping incidents are captured at identical time steps for the two modelling cases, and the figure proves that the magnitude of the resulting water height on deck is significantly larger in the case where the relative motion model is applied, similar to what was shown for the water height probes. The figure shows that the incoming wave is significantly disturbed by the presence of the FPSO structure, and it no longer has a smooth symmetric curvature. A halfcircle shaped wave on top of the incoming wave in front of the bow is seen in both cases, seemingly generated when the incoming wave travels up along the bow and encounters the curvature in the bow near the deck. In the case without relative motion modelling this wave travels away from the FPSO, whereas in the other case the wave stays at the same distance from the FPSO bow, until it disappears into the descending water in front of the bow. It is also seen that the shipping wave reaches the water height probes much sooner in the case with relative motion than in the case without relative motion, which is also seen for the probes in Figs. 8.7 and 8.8.

The shape of the flow on deck was in Buchner (1995a) compared to a dam break type flow. However, the visualisations in Fig. 8.9 show one significant difference from the dam break flow, which is the plunging type wave front observed at the corner of the deck at the initial stage of the wave shipping. Dam break flow was investigated in Chapter 4, and in the beginning of the dam break flow, which should correspond to this wave front, the water progresses fastest at the bottom of the domain and does not exhibit this plunging wave behaviour. However, apart from this difference, the remaining part of the flow does show resemblance to the dam break flow. Modelling of the deck flow resulting from wave shipping using dam break flow has also previously given promising results in the publications described in Chapter 1. Fig. 8.10 shows the contours of the flow on deck and in front of the FPSO bow, captured in the $x - z$ plane during the experiments (Buchner, 1995b). The flow on deck shows good resemblance to the computed flow contours in Fig. 8.9. The same type of plunging flow behaviour is seen at the initial stage for the experiments, though not quite as distinct as in the computations. For the flow in front of the bow there seems to be more difference between computations and experiments. The experiments more clearly show two wave crests travelling away from the bow. However, since only the contour, and not the whole field, is included it is not possible distinguish the finer flow contours. One thing is clearly different between experiments and computations. The surface elevation in front of the bow seems to rise continuously during the experimental sequence. Although the time steps in the computations and the experiments are not directly comparable, it is clear that in the computations, the corresponding surface elevation peaks around the second frame and in the following sequence drop. The experimental sequence is captured with a time step of 0.3 s, whereas the computations are captured with 0.6 s. From comparing the two figures it can be seen that the second experimental line correspond to the first image from the computations, and due to the differece in timestep, the following four experimental lines correspond to two computed images. However, the two figures still indicate that the relative ship motion in the computations does not have the same phase angle to the incoming

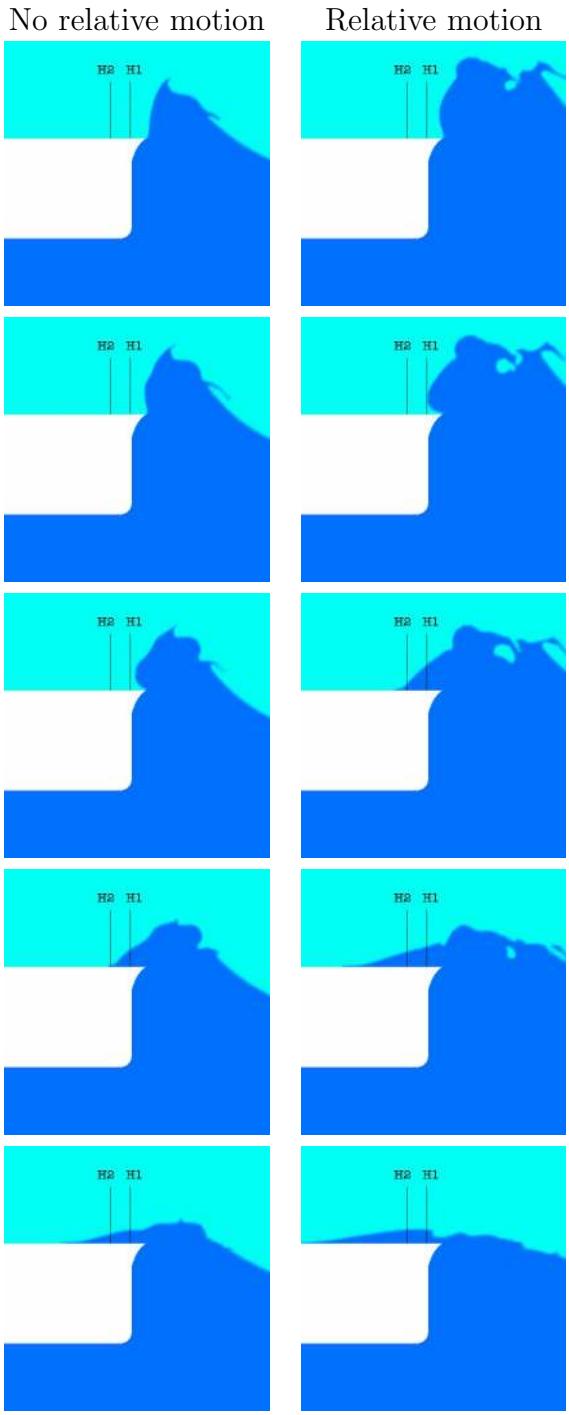

Figure 8.9: *Visualisation of the free surface near the 2-D FPSO bow from time $t = 31.6$ s, in increments of 0.6 s. The location of the water height probes H1 and H2 is indicated by lines. The left column is for computations without relative motion modelling, in the right column the relative motion model is included. Fine grid, $H = 17.3$ m, $T = 11.2$ s.*

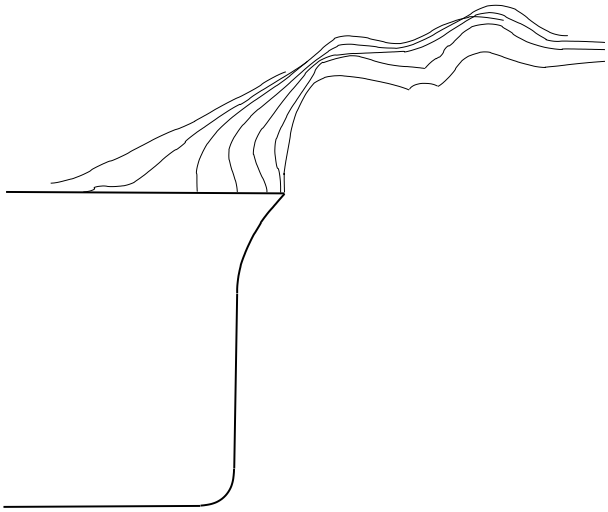

Figure 8.10: *Bow wave contours captured during experiments (Buchner, 1995b). Time step between contours* $\Delta t = 0.30$ *s.*

wave as the relative ship motion in the experiments. This can possibly be ascribed to the simplified relative ship motion model, which is used during the computations. This relative motion model both assumed simplifications in the hull structure and used a linear incoming wave profile. Further, the phase angle in the simplified motion model is calculated using the added mass, which is assumed to be constant and equal to the still water displacement. These simplifications can explain the difference in phase angle between computations and experiments.

8.2.6 Resulting Water Height on Deck for 2-D FPSO Case

The computed resulting water height on deck obtained by use of the fine grid is in Fig. 8.11 compared to the experimentally obtained water height at the probe H1. The figure shows that the numerically predicted result is close to the experimental result and only very small differences are observed in the peak value and the duration of the water flow at the probe. The computed and the experimental results for the second probe H2 are compared in Fig. 8.12. The agreement between the results is not as good here as with the previous probe. The two figures show that the computed resulting water height on deck decays faster along the deck than measured during the experiments. This may be caused by many factors, but most noteworthy is the simplifications of the green water incident made during the numerical prediction. First of all the simulation is performed in 2-D, which eliminates possible 3-D effects of wave diffraction and reflection around the bow and the flow from the side of the bow onto the deck. Further, the full interaction between ship and incoming wave is not modelled by the relative motion model applied in the computations. This model only ensures a correct relative vertical motion between vessel and mean water level, but the ship-wave interaction is more complex than just the vertical motion, where first of all the pitching motion may

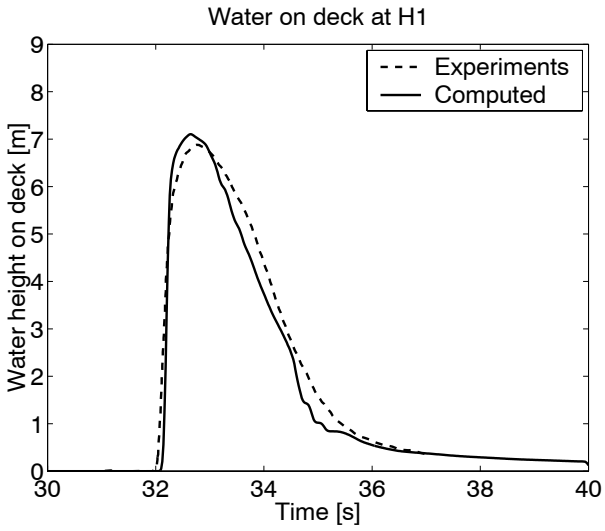

Figure 8.11: *Comparison between experimental (Buchner, 1995a) and computed water height on deck at probe H1. The computed results are obtained using the 2-D FPSO grid with the fine resolution, see Table 8.3.*

have a significant influence. The vessel, which has a continuous heave and pitch motion, could be more influenced by the incoming wave than seen in the computations, where only the vertical translation of the mean surface is modelled. The probe H2 is reached by the wave at approximately $t = 32$ s. This is approximately 1 second before the pitching angle becomes negative, implying that the bow is only slightly inclined relative to the mean water level.

In the experiments only the nominal incoming wave height has been given. An experiment without the presence of the structure where the incoming wave kinematics could have been verified was not reported. This makes it difficult to evaluate how accurate the incoming wave kinematics was reproduced in the computations, compared to the experiments. If the resulting water height on deck during the experiments was not obtained from the first incoming wave component, the reflection from previous wave components would probably influence the incoming wave kinematics.

The computational domain, shown in Fig. 8.4, might also be relatively small, considering that the incoming wavelength $\lambda = 209.45$ m. In Chapter 7, as part of the wave run-up on wall investigation, the necessary size of the computational domain relative to the incoming wave was investigated. This investigation gave the indication that an optimum domain size would be at least five times the size of the generated wavelength. However, the disturbances in the flume caused by a smaller domain are not noticeable until after about four periods for a domain length a little larger than three times the wavelength, so with this in mind, the current domain size is considered satisfactory.

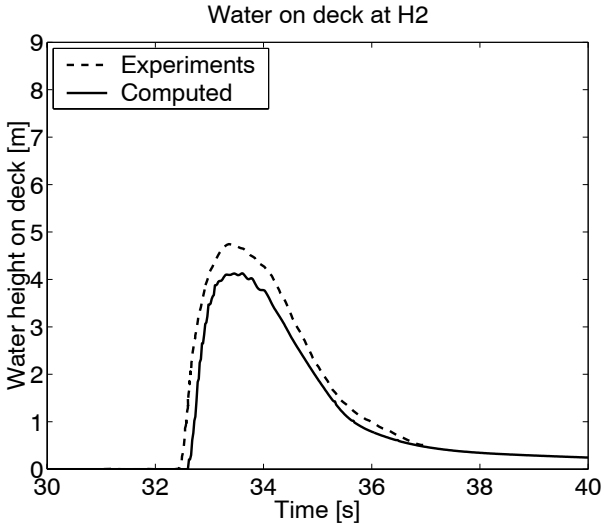

Figure 8.12: *Comparison between experimental (Buchner, 1995a) and computed water height on deck at probe H2. The computed results are obtained using the 2-D FPSO grid with the fine resolution, see Table 8.3.*

8.2.7 Conclusion to 2-D Green Water Modelling

The agreement between experimental and computed results shown in the previous section is satisfactory, especially considering the simplifications made in the computed results. However, many aspects still need investigation in order to be able to conclude anything about the general applicability of the present method. First of all the investigation must be extended to include a wider range of incoming wave kinematics, to investigate the sensibility toward incoming wavelength and wave height, which will both influence the shipping wave and the ship motion. The investigation must also be extended to include other bow geometries, with variations especially in bow flare and freeboard height, to determine whether the present results stem from any cancellation effects, which have benefited the overall agreement between computations and experiments. However, as an attempt to model green water load on an FPSO, this 2-D model gives very good results. Considering how little information regarding the full FPSO is required, i.e. main particulars and a contour definition, this method of predicting green water load is applicable even at the conceptual design stage.

8.3 3-D Numerical Prediction of Green Water on Deck

The next step in the green water investigation is to extend the simulations to three dimensions. The numerical investigation will be an extension to what was discussed in the previous section, using the Buchner (1995a) experiments for validation and applying the relative motion model described in Section 8.2.1. First, details about the computations are given.

8.3.1 3-D Numerical Simulation

The grid topology used for the 3-D computations is presented in Fig. 8.13. The domain is divided into 19 blocks in three layers. Two grids are used with different resolutions, in order to investigate convergence properties. The grids are outlined in Table 8.4 where the block numbering is as follows: the blocks in front of the FPSO are numbered 0, 1 and 2, the forward blocks at the port and the starboard side are 3, 4, 5 and 6, 7, 8, respectively, the two forward blocks on top and below the FPSO are numbered 9 and 10, the aft blocks port and starboard of the FPSO are numbered 11, 12, 13 and 14, 15, 16, respectively, and finally the two aft blocks above and below the FPSO are numbered 17 and 18. The two grids are stretched toward the FPSO where the ship wave interaction requires a larger amount of cells. Compared to the resolution used in the 2-D case, the 3-D grids are significantly less resolved in the $x - y$ plane. In the 2-D case the three grids, for the horizontal resolution of the block in front of the FPSO, used 96, 160 and 224 grid cells, respectively. In comparison, the two 3-D grids apply 32 and 64 grid cells horizontally. However, both memory requirements and computation time make it difficult to resolve the problem more than in the present fine case, where approximately 0.9M grid cells are applied. The full simulation with the fine grid requires approximately 30 hours on a linux cluster, employing 14 computational nodes, each with a 2.3 GHz P4 processor. The total computational domain length in the 3-D computations is 400 m. This is shorter than in the 2-D case, but again this length was reduced in order to reduce the required number of cells. The generated wave kinematics will be investigated in the following to verify that the generated waves in the 3-D case are similar to those in the 2-D case. The width of the domain equals 300 m and the total height of the domain is 180 m, with a water depth of 150 m.

Table 8.4: *Grid resolutions for numerical simulation of 3-D green water loads. The grid topology is shown in Fig. 8.13. The grid cells are given as $n_x \times n_y \times n_x$ (nr. of cells in the sailing direction of the FPSO $\times$ nr. of cells horizontally perpendicular to the sailing direction $\times$ nr. of vertical cells).*

	Coarse	Fine
Blocks 0,1,2	$32 \times 32 \times 32$	$64 \times 32 \times 32$
Blocks 3,4,5,6,7,8	$32 \times 32 \times 32$	$32 \times 64 \times 32$
Blocks 9,10	$32 \times 32 \times 32$	$32 \times 32 \times 32$
Blocks 11,12,13,14,15,16	$16 \times 32 \times 32$	$16 \times 64 \times 32$
Blocks 17,18	$16 \times 32 \times 32$	$16 \times 32 \times 32$

To investigate the wave kinematics generated during the 3-D computations, the wave elevation is compared in a location 100 m to the starboard side of the FPSO bow with the location equivalent to the wave kinematics investigation in the 2-D case. The wave elevation is computed during the green water incident, with the FPSO structure located in the domain. Since the elevation is computed so far away from the structure, the waves reflected from the structure have not yet travelled to the location of the elevation probe and will not influence

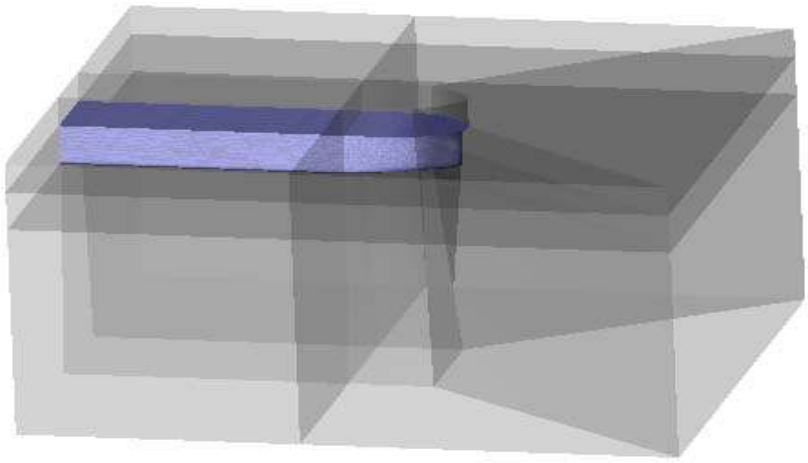

Figure 8.13: *Multiblock structured grid used for 3-D green water investigation. The grid consists of 19 blocks in three layers, the first layer from the sea bottom to the bottom of the FPSO, the second layer at the same level as the FPSO, and the third layer on top of the FPSO.*

the computed wave elevation. The elevations are shown in Fig. 8.14, including the wave kinematics computed in the 2-D case. It must be added that the computations performed with the coarse grid could not be computed all the way to time $t = 40$ s, but had to be stopped at $t \simeq 35$ s due to a numerical problem, so the wave elevation for the coarse grid is not computed beyond this point. This did not influence the computations of the green water incident, since the majority of it occurs before this point. The wave elevation in the figure shows that the wave kinematics for the two grids is almost identical, and also identical to the wave elevation computed in the 2-D case, at least for time $t < 35$ s. After this point the disturbance due to the presence of the FPSO structure in the (3-D) computational domain could be the cause of the disturbance observed in the computations. However, before this point, the elevations for the 3-D computations exhibit the same behaviour as in the 2-D case, which ensures that the incoming wave kinematics is correct. The kink in the elevation curve which is observed at time $t \simeq 18$ s is at the starting point of the relative motion model, described previously.

The next step in the verification of the 3-D numerical results is a comparison of the resulting water heights at the probes H1 and H2 for the two grids. These are plotted in Fig. 8.15, which shows a small difference between the two grids. The quantitatively biggest difference between the two results is in the peak value at probe H2, but at the H1 probe the plots also differ slightly. Moreover, while the generated wave kinematics shows that convergence is reached with respect to the incoming wave, the results here indicate that the flow on deck is not sufficiently resolved. However, the difference is relatively small and the computations are believed to be close to convergence.

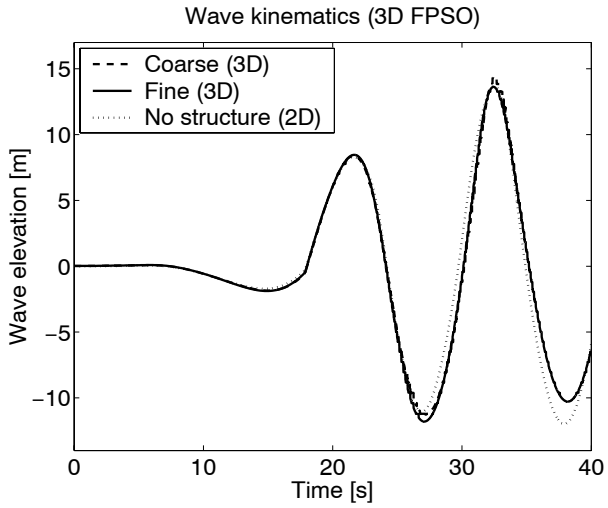

Figure 8.14: *Incoming wave kinematics for the 3-D green water computations, using the two grids specified in Table 8.4. The wave elevation is computed in a location 100 m to the starboard side of the FPSO bow during the wave impact. The wave kinematics from the 2-D case, computed without the presence of a structure, is included for comparison.*

The obtained results are close to the same water heights computed with the 2-D grid (see Figs. 8.11 and 8.12). This is surprising as three dimensional effects were believed to have an influence on the flow on deck. However, since the incoming wave is longcrested, and in this sense two-dimensional, the 3-D effects can only arise from diffraction around the (curved) FPSO deck. Apparently, this has no significant effect on the present configuration. Whether this conclusion holds for other configurations, i.e. different incoming wave kinematics, other bow shapes, variations in ship's length - wavelength ratio etc., further investigations will have to clarify. In the following section a visualisation of the flow on deck is presented, which illustrates the physics of the flow on deck.

8.3.2 Visualisation of the Flow on Deck

A visualisation of the water flow on deck is given in Fig. 8.16. Only the water on top of the FPSO deck is shown and the water in the remaining domain is removed in order to be better able to identify the flow on deck. The first image (1) shows a small region of water entering from in front of the FPSO. The shape of the water region indicates that a plunging wave breaking occurs in front of the FPSO, similar to the behaviour seen in the 2-D visualisations. The entering of this plunging wave explains the sudden rise in water height at the probe H1, which was shown in Fig. 8.15. The occurrence of the plunging wave increases the water height at the probe instantaneously. At probe H2 it drops closer to the deck, which explains the drop in peak height at this probe.

The water initially enters the deck area from the front of the FPSO, and as the water height in the front part of the deck increases, water also enters from the sides of the deck. The

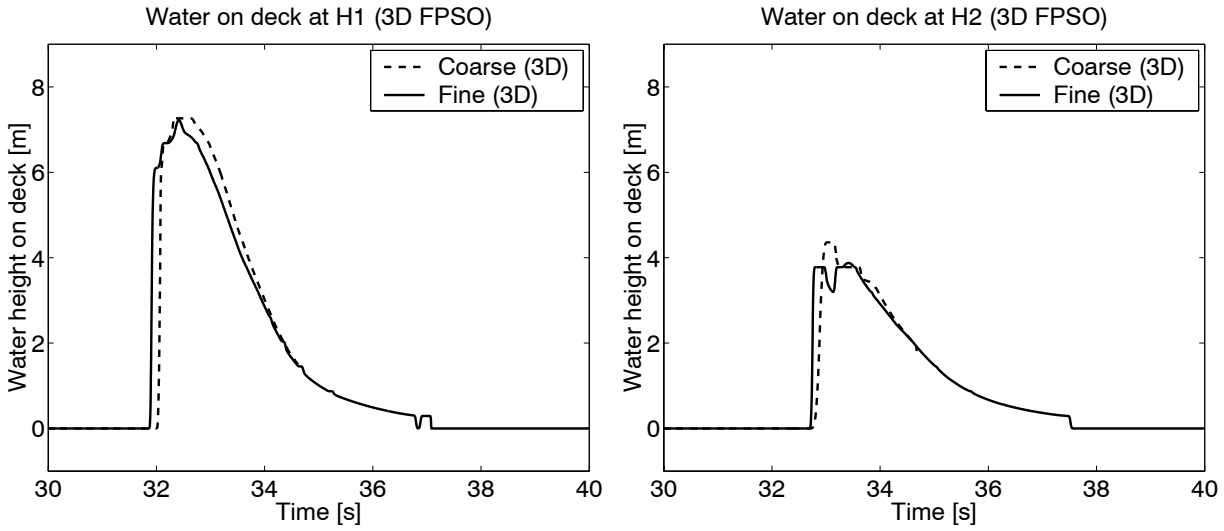

Figure 8.15: *Resulting water height on deck at probes H1 (left) and H2 (right) for the 3-D FPSO case, using the two grids described in Table 8.4. $H = 17.3$ m, $T = 11.2$ s.*

largest amount of water is clearly in the very forward part of the deck and as the flow progresses along the deck the water height at the front decreases. Toward the end of the visualisation the formation of a 'tongue' of water at the centerline of the deck is clearly seen. This flow behaviour is very similar to what was documented by Buchner (1995a). During these experiments the deck flow contours are captured by a vessel mounted camera and these contours are shown in Fig. 8.17. A similar 'tongue' of water forming toward the end of the green water incident is seen in the experiments, although it is slightly narrower than for the computations. A quantitative validation of the flow on deck is given in the following section where the resulting water height on deck is compared between computations and experiments.

8.3.3 Validation of 3-D Computations

The resulting water height on deck depicted in Fig. 8.15 is compared in Fig. 8.18 to the experimental data from Buchner (1995a). The results from the 2-D computation are also included for comparison. The figure shows good agreement between the 3-D computations and the experimental results. Both the magnitude and the duration of the water height at H1 are very well predicted in the computations. The second probe shows a larger deviation between numerical and experimental results, but the water heights are still very close. The figure also illustrates that the difference between 2-D and 3-D results is very small, and only significant at the second probe (H2). As previously discussed, the 3-D computations are possibly not sufficiently resolved, but further cells are however not expected to influence the results significantly. The visualisations in Fig. 8.16 also demonstrates that except at the edge of the FPSO deck, the curvature of the flow across the ship's deck is only seen further

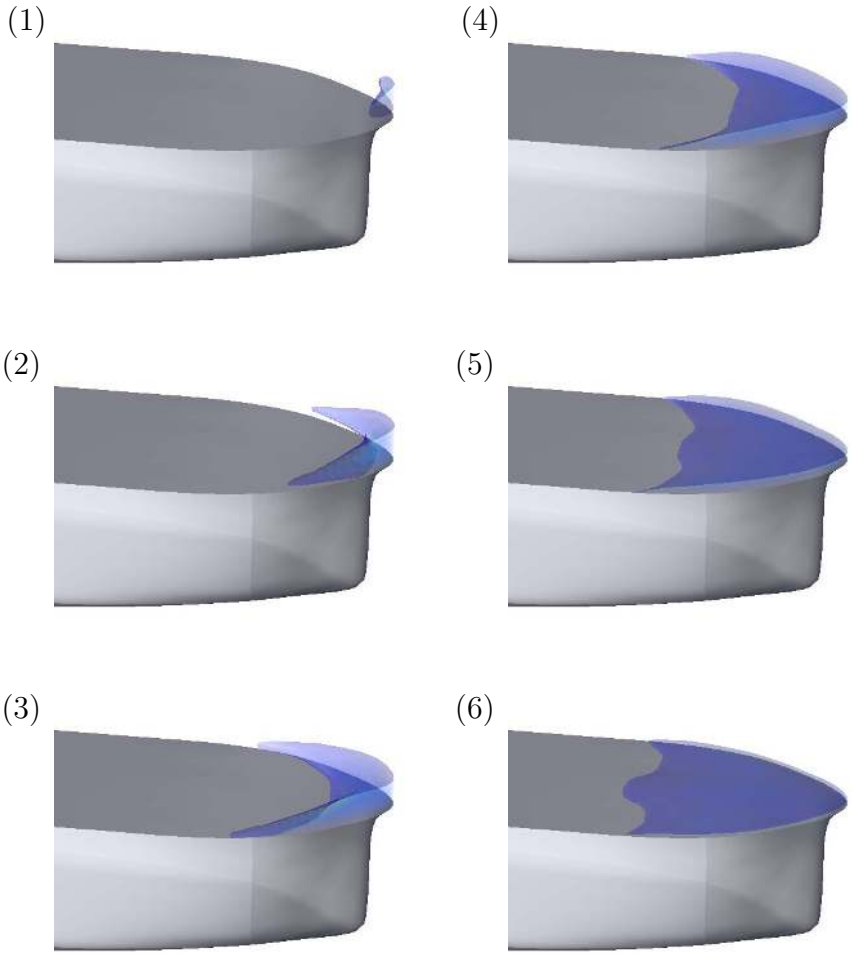

Figure 8.16: *Visualisation of the flow on deck for 3-D green water computations, obtained by use of the fine grid Table 8.4. Only flow directly above deck is included in order to be able to determine deck the flow behaviour. Frame (1) is at* $t = 32s$*, and the time step between frames* $\Delta t = 0.5s$*.(*$H = 17.3$ *m,* $T = 11.2$ *s).*

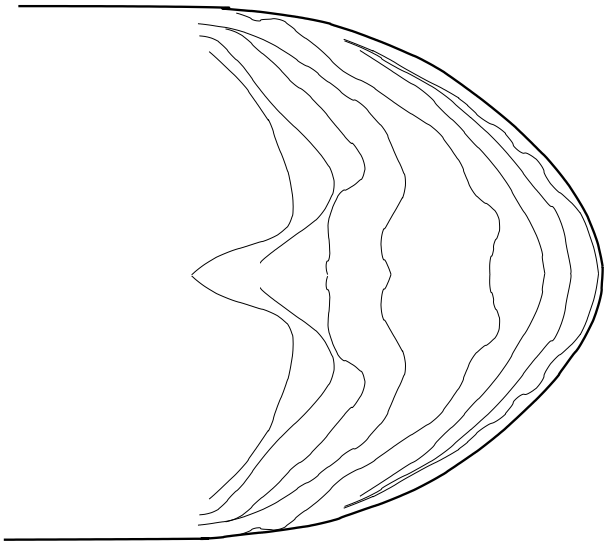

Figure 8.17: *Flow contours for the flow on deck of the FPSO captured during the experiments (from Buchner (1995b))*

down the ship. Thus only here it is expected to give a larger difference between 2-D and 3-D results.

8.3.4 Conclusion

The resulting water height on deck from the green water incident clearly proves that both 2-D and 3-D computations of green water incidents can describe most of the ship-wave interaction which was recorded during the experiments. Even though the computational model only includes the vertical ship motion, the investigation shows that the VOF model captures most of the green water flow physics, including the flow on deck. This gives an interesting perspective for the future of VOF modelling with respect to green water loads. The possibility of determining optimal bow shape configurations based on resulting water height on deck may be an option in the near future, even with the present simplified interaction model. An enhancement of the computational model to include the full interaction problem with both heave and pitch motion can help refine the computational investigation.

In the design against green water events, the water height on deck is only a preliminary result. The desired result is the impact pressure on deck or deck mounted structures which occur as a result of the shipped water. The present investigation did not include an investigation of the resulting pressure on deck. This will be the next step in the validation of the computational model. However, the present model has one drawback which can limit its ability to predict pressure loads on the deck. In Buchner (1995a) the various contributions to the resulting pressure on deck were specified, and an important contributing factor was the vertical acceleration of the FPSO. Although it was shown that this contribution was slightly out of phase with the two other main contributions, i.e. static water pressure and

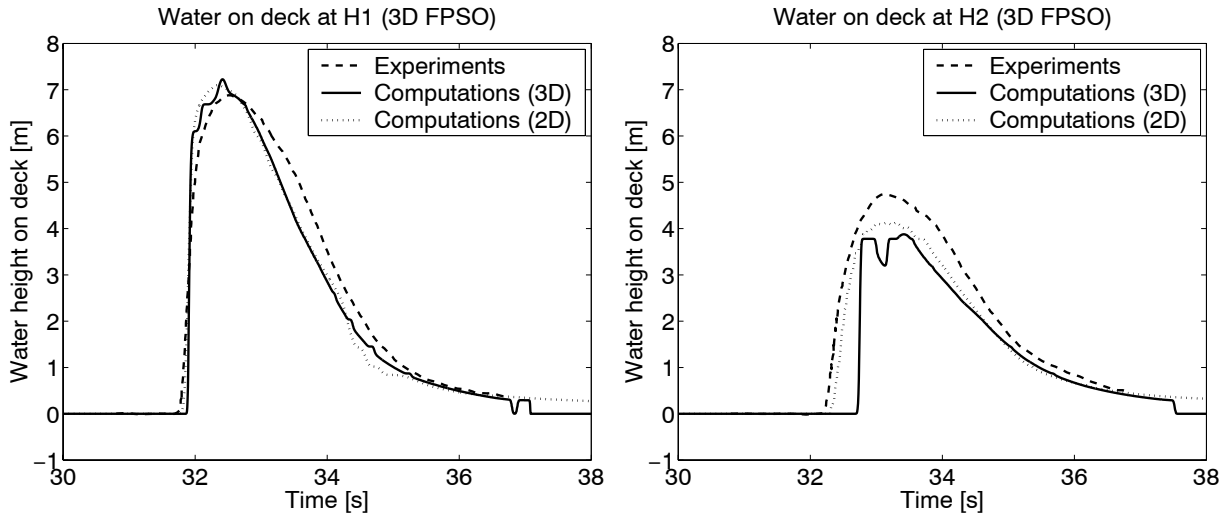

Figure 8.18: *Comparison between experimental (Buchner, 1995a) and computed water height on deck at probes H1 (left) and H2 (right). The computed results are obtained by use of the 3-D FPSO grid with the fine resolution, see Table 8.4. Results from the 2-D computation are included for comparison (dashed line).*

rate of change of water height on deck, the vertical acceleration of the FPSO cannot be considered negligible. The present computational model does not include this contribution, since the vertical motion is seen from a vessel fixed coordinate system. Further validation is required to investigate this effect, and possibly is can be modelled semi-empirically. The present model computes the time history of both heave and pitch motion, which can be used to add a contribution to the deck pressure, resulting from the vertical ship acceleration. This requires that the phase is computed correctly, so that the superposition of pressures is correct and further validation of the relative ship motion model can help determine whether this is achievable. For the impact pressure on deck mounted structures it was shown in Chapter 7 that the impact pressure on such structures can be very well predicted by the present model. In the case of these vertically oriented structures, the vertical acceleration of the FPSO will only have a very small effect on the impact load, which should make it possible to predict this impact by the present model. The topic of pressure loads on the deck and deck mounted structures is the next step in the validation of the VOF model with regard to green water problems.

Chapter 9

Conclusions and Recommendations for Future Work

In the present thesis several topics related to green water investigations are analysed and discussed. This chapter presents a summation of some of the most important findings and also gives recommendations to future work within the field.

9.1 Conclusions to Present Work

A pure convection test is used as a benchmark test of selected VOF transport schemes, by determining which scheme retains the original volume fraction distribution best, after the field is convected obliquely through a domain. Of the four schemes tested, i.e. Hyper-C, UltimateQuickest, HRIC and CICSAM, the latter scheme shows the best performance. This scheme is selected as the preferred scheme throughout the present work.

The dam break and cylinder impact cases are used as initial test examples for validation of the numerical model, since the cases involve elements which are important when modelling green water, i.e. complex free surface flows and impact loads. Furthermore, the dam break problem has previously been used as a model for the water flow on deck resulting from green water incidents, which makes it interesting in the present context. In both test cases the results obtained with the numerical model show good agreement with experimental data.

The grid resolution study in the dam break case shows that although results obtained with three different grids give similiar results, the grid convergence is not fully monotonic. However, the difference in results obtained by use of the different grids is only visible after the flow returns from the impact with the opposite wall, where the water is very disturbed. This makes that part of the experiment difficult to reproduce numerically. This is further documented by both sensitivity studies and comparisons with other numerical methods. In

the experimental study (Zhou *et al.*, 1999) it was reported that repetition of the experiments did not give exactly the same results, but the magnitude of the change between the individual repetitions was not reported. In general, the comparison between computational and experimental results for both water height and impact pressure is satisfactory, though a closer investigation of the sensitivity of the experimental uncertainties would be valuable.

In the cylinder impact case verification of the computed results shows that the different grid resolutions gives a change in the computed water flow behaviour. Only with the finest resolution is it possible to recreate the flow separation features shown in the experiments. However, this change in fluid behaviour does not influence the vertical force on the cylinder, which is very similar for all grids. In the initial stage of the impact where the vertical force is dominated by inertia force, the agreement between computations and experiments is very satisfactory, but the later stages of the impact the difference between computations and experiments is more prominent.

The tank sloshing cases shows that the flow dynamics in a partially filled tank, exposed to horizontal sinusoidal excitations are very well predicted numerically. Both free surface contours and pressure levels inside the tank are well reproduced numerically, compared to experimental data. The only significant inaccuracy in the computational model is the inability to retain all the fluid which is present in the tank initially. However, this problem is only noticable after several periods and overall the accuracy in the numerical results is satisfactory.

The wave crest impact on deck investigation shows that the computational model can predict impact loads very accurately, eventhough it involves very complex interactions between the structures and the free surface. This investigation is carried out by use of inviscid flow calculations, as from an engineering perspective the inclusion of viscous or turbulent terms will not affect the present results, since the problem is not domainted by either viscous or turbulent contributions. The general agreement for the impact forces on a single horizontal plate between computations and experiments is very satisfactory. And in the two plate cases where a water jet shoots over the first plate and impacts the second plate, the secondary impact on the downstream plate is also well predicted.

The green water investigations include both simplified cases and a full green water problem. The simplified investigation include a wave run-up case and a 2-D green water case, where the wave run-up on a wall investigation can be regarded as an initial step in a green water incident. For this case the visualisation of the free surface contours shows that the computaions closely reproduce the free surface contours at the edge and on top of the wall when a wave encounters the wall, compared to surface contours captured during the experiments. However, the results show some uncertainty regarding the influence of resonant waves inside the flume, which influence the magnitude of the wave run-up. A better control of the incoming wave kinematics is required in order to be able evaluate the accuracy of the numerically predicted results compared to the experiments.

The first green water problem is a simplified 2-D case, without relative ship motions. Eventhough during the experiments it is not possible to fully eliminate 3-D effects, the test setup

is constructed to minimise these, using a prismatic structure spanning the whole width of the wave flume. To simplify the wave-structure interaction, the structure, which is an expanded contour line of an FPSO, is fixed in time. From a comparison with the generated wave kinematics measured during the experiments it is shown that the incoming waves in the computations closely reproduce these. Visualisations of the wave impact at the FPSO bow, from both experiments and computations show that the progressing water flow in the experiments is very well captured numerically, and that even the small cavity which appear at the forward edge of the FPSO deck in the initial part of the green water shipping is seen in the computations. The resulting water height on deck of the FPSO is also well reproduced, shown by a comparison of water height measured at two probes located in the front part of the FPSO deck. The investigation also shows that impact loads on deck mounted structures can be predicted accurately. A vertical wall, simulating a breakwater type structure, is placed on the front of the FPSO deck, and by the use of pressure probes located on the structure, it is shown that the computational method can closely reproduce the impact loads on the structure resulting from the green water impact. In conclusion the simplified green water investigation shows very promising results, and at least for this type of simplified modelling, the results are very encouraging with regard to the application of the numerical model in green water problems.

Finally, a full green water problem including ship motions is investigated numerically. The experimental data used as reference (Buchner, 1996) were obtained in a model wave tank, using a scaled model of an FPSO, exposed to regular incoming waves. This problem is numerically investigated in both 2-D and 3-D for the purpose of analyzing the 3-D effects related to the green water incident. In the computations, the green water problem is simplified by excluding ship motions in the computational domain. Instead, a relative ship motion model is applied, where the vertical motion of the FPSO at the bow is modelled by use of simplified closed-form expressions for the transfer functions for heave and pitch. These are transformed to the computaional domain by varying the mean water level during the green water event, thereby coupling ship motions and incoming wave. The water height on deck resulting from the green water incident shows very good agreement between computations and experiments. Furthermore, the computations show that 2-D and 3-D modelling gives very similar results and that the flow at the fore part of the deck is not signicantly affected by 3-D contributions. The present investigation is only conducted with long crested 2-D incoming waves, whereas real life applications will experience 3-D seastates, with directionally spread incoming waves, and in that case threedimensionality may be significant. However, current methods for determining green water loads (Buchner (1995b), Ogawa *et al.* (1998), Buchner (2002)) only use long crested 2-D incoming waves, so if the present method, both in 2-D and 3-D proves valid in general, it can become an important tool in green water investigations. And since the 2-D investigation only requires very little information about the FPSO vessel, this methodology can be applied even in a conceptual design phase.

9.2 Recommendations for Future Work

The present approach to green water modelling still contain elements which need to be further verified through additional numerical simulations, and also needs to be validated against more comprehensive experimental studies. The following list describes some of the relevant topics for future studies:

- **3-D studies of green water**
  The required resolution in the 3-D simulations needs to be further verified. This can also help future investigation with requirements of grid resolution and computational domain size for numerical simulations of other green water load problems. The present green water investigation shows that, at least to some extend, the green water problem is two-dimensional. Whether this can be extended to other hull shapes and different incoming wave kinematics requires further investigations.

- **Validity of the relative ship motion model**
  A closer investigation of the relative ship motion model will help determine the applicability range of the model. In particular, an investigation of the performance of the model when very steep nonlinear waves are applied, compared to strip theory or model experiments, should be performed. The investigation should also be extented to include other ship hull geometries, and the influence of shiplength - wavelength ratio.

- **Definition of incoming wave kinematics**
  A better description of the incoming wave kinematics is desirable, since the present simulations are based nominal values obtained from the experiments. Time series of the wave elevation from the model wave tank during the experiments, either with or without the FPSO structure present in the wave tank, can help future investigation to describe incoming wave kinematics. This will help in evaluations of uncertanties, when comparing numerical and experimental results.

- **Inclusion of deck pressure and impact loads on structures**
  The present study of the full green water incident only determine the water height on deck, resulting from green water shipping. A full analysis must also include studies of pressure loads both on deck plating and on deck mounted structures. The present method of ship motion modelling, where the mean water level is adjusted and the problem is modelled in a vessel fixed coordinate system, does not include the contribution to deck pressure loads caused by vertical vessel acceleration. This could possibly be modelled from the transfer functions, which are used to model the relative ship motion.

- **Parametric studies of green water incidents**
  If the present method for green water modelling shows general applicability, a parametric study for evaluation the ideal bow geometries would be of great value. Through this, guidelines for optimal FPSO bow geometries with respect to green water loads could be proposed.

- **Full numerical simulation of green water problems**
  It is possible to numerically model the full green water problem, similar to the method used by Repetto (2001). The full ship-wave interaction problem is modelled, including the response of the FPSO from the incoming waves. However, such full numerical modelling requires very substantial computational effort, probably beyond what is generally presently available.

References

Arai, M., Cheung, L. Y. and Inoue, Y. (1995). Hydrodynamic impact loads on horizontal members of offshore structures. In *Proceedings of the International Conference on Offshore Mechanics and Arctic Engineering - OMAE*, vol. 1.

Baarholm, R. J. (2001). *Theoretical and Experimental Studies of Wave Impact underneath Decks of Offshore Platforms*. Ph.D. thesis, Norwegian University of Science and Technology.

Bea, R. G., Iversen, R. and Xu, T. (2001). Wave-in-Deck Forces on Offshore Platforms. *Journal of Offshore Mechanics and Artic Engineering*, vol. 123 (3).

Buchner, B. (1994). On the effect of green water impacts on ship safety (A pilot study). In *NAV '94 International Conference on Ship and Marine Research*. Rome, Italy.

Buchner, B. (1995a). The impact of green water on FPSO design. In *Offshore Technology Conference 95 (OTC'95)*. Houston, USA. OTC paper 7698.

Buchner, B. (1995b). On the impact of green water loading on ship and offshore unit design. In *The Sixth International Symposium on Practical Design of Ships and Mobile Units (PRADS'95)*.

Buchner, B. (1996). The Influence of Bow Shape of FPSOs on Drift Forces and Green Water. In *Offshore Technology Conference*, pages 389–400. Houston, Texas, USA.

Buchner, B. (2002). *Green Water on Ship-type Offshore Structures*. Ph.D. thesis, Delft University of Technology.

Buchner, B. and Voogt, A. (2000). The Effect of Bow Flare Angle on FPSO Green Water Loading. In *Proceedings of ETCE/OMAE2000 Joint Conference*, pages 1–8. New Orleans, USA.

Colagrossi, A., Landrini, M. and Tulin, M. P. (2001). A Lagrangian Meshless Method for Free-surface Flows. In *4th Numerical Towing Tank Symposium*, edited by V. Bertram. Hamburg.

Colicchio, G., Colagrossi, A., Greco, M. and Landrini, M. (2001). Free-Surface Flow After a Dam Break: A Comparative Study. In *4th Numerical Towing Tank Symposium*, edited by V. Bertram. Hamburg.

Cozijn, J. L. (1996). Numerical simulation of Green Water. Tech. rep., MARIN Wageningen / Delft University of Technology, the Netherlands.

Ersdal, G. and Kvitrud, A. (2000). Green Water on Norwegian Production Ships. In *Proceedings of the Tenth (2000) International Offshore and Polar Engineering Conference*, pages 211–218. Seattle, USA.

Faltinsen, O., Kjærland, O., Nøttveit, A. and Vinje, T. (1977). Water impact loads and dynamic response of horizontal circular cylinders in offshore structures. In *Offshore Technology Conference*, pages 119–126.

Fekken, G., Veldman, A. E. P. and Buchner, B. (1999). Simulation of Green Water loadings using the Navier-Stokes equations. In *7th International Conference on Numerical Ship Hydrodynamics*. Nantes.

Fenton, J. D. (1988). The numerical solution of steady water wave problems. *Computers and Geosciences*, vol. 14 (3): pages 357–368.

Ferziger, J. H. and Perić, M. (1997). *Computational Methods for Fluid Dynamics*. Springer.

Fukuda, J., Ikegami, K. and Mori, T. (1973). Predicting the Long Term Trends of Loads on Deck due to Shipping Water. *Journal of the West Japan Society of Naval Architects*, vol. 45.

Gaskell, P. H. and Lau, A. K. C. (1988). Curvature-compensated convective transport: SMART, a new boundedness preserving transport algirithm. *Int. Journal of Numerical Methods for Fluid Dynamics*, vol. 8: pages 617–641.

Greco, M. (2001). *A two-Dimensionl study of Green-Water Loading*. Ph.D. thesis, Norwegian University of Science and Technology, Trondheim, Norway.

Hamoudi, B. and Varyani, K. S. (1998). Significant load and Green Water on deck of Offshore Units/Vessels. *Ocean Engineering*, vol. 25 (8): pages 715–731.

Harlow, F. H. and Welch, J. E. (1965). Numerical calculations of time-dependent viscous incompressible flow of fluid with free surface. *Phys. Fluids*, vol. 8 (12): pages 2182–2189.

Hellan, O., Hoff, J. R. and Stansberg, C. T. (2001). A practical design tool for wave impact on bow and deck structures. In *Practical Design of Ships and Other Floating Structures (PRADS 2001)*, edited by Y.-S. Wu, W.-C. Cui and G.-J. Zhou, pages 611–619. Shanghai, China.

Hinatsu, M., editor (2001). *Proceedings of SRI-TUHH mini-Workshop on Numerical Simulation of Two-Phase Flows*. National Maritime Research Institute, Tokyo, Japan.

Hinatsu, M., Tsukada, Y., Fukusawa, R. and Tanaka, Y. (2001). Experiments of Two-Phase Flows for the Joint Research. In *Proceedings of SRI-TUHH mini-Workshop on Numerical Simulation of Two-Phase Flows*, edited by M. Hinatsu, pages 12–19. National Maritime Research Institute, Tokyo, Japan.

Hirt, C. W. and Nichols, B. D. (1981). Volume of fluid (VOF) method for the dynamics of free boundaries. *Journal of Computational Physics*, vol. 39: pages 201–225.

Jensen, J. J., Beck, R. F., Du, S., Faltinsen, O. M., Fonseca, N., Rizzuto, E., Stredulinsky, D. and Watanabe, I. (2000). Extreme Hull Girder Loading (Special Task Committee VI.1). In *Proceedings of the 14th International Ship and Offshore Structures Congress*, edited by H. Ohtsubo and Y. Sumi, vol. 2, pages 263–391. Elsevier.

Jensen, J. J., Mansour, A. E. and Olsen, A. S. (2003). Estimation of Ship Motion Using Closed-Form Expressions. *Ocean Engineering*. Submitted.

Kaplan, P., Murray, J. and Wu, W. (1995). Theoretical analysis of wave impact forces on platform deck structures. In *Proceedings of the International Conference on Offshore Mechanics and Arctic Engineering - OMAE*, pages 189–198.

Kawamura, T. (1998). *Numerical Simulation of 3D Turbulent Free-Surface Flows*. Ph.D. thesis, University of Tokyo.

Leonard, B. P. (1991). The ULTIMATE conservative difference scheme applied to unsteady one-dimentional advection. *Computer Methods in Applied Mechanics and Enginering*, vol. 88: pages 17–74.

Lloyd, A. R. M. J., Salsich, J. O. and Zseleczky, J. J. (1985). The effect of bow shape on deck wetness in head seas. *Transactions, Royal Institution of Naval Architects*.

Maruo, H. and Song, W. (1994). Nonlinear analysis of bow wave breaking and deck wetness of a high speed ship by the parabolic approximation. In *Proceedings of the 20th Symposium on Naval Hydrodynamics*. National Academic Press.

Mayer, S., Garapon, A. and Sørensen, L. S. (1998). A fractional step method for unsteady free-surface flow with applications to non-linear wave dynamics. *International Journal for Numerical Methods in Fluids*, vol. 28 (2): pages 293–315.

Mizoguchi, S. (1989). Design of Freeboard Height with the Numerical Simulatation on the Shipping Water. *Practical Design of Ships and Mobile Units (PRADS)*.

Muzaferija, S., Perić, M., Sames, P. and Schellin, T. (1998). A Two-Fluid Navier-Stokes Solver to Simulate Water Entry. In *Twenty-Second Symposium on Naval Hydrodynamics*, pages 638–651. Washington, D.C. Preprints, Tuesday/Wednesday Sessions.

Nielsen, K. B. and Mayer, S. (2001). Numerical Simulation of Tank Sloshing. In *Proceedings of SRI-TUHH mini-Workshop on Numerical Simulation of Two-Phase Flows*, edited by M. Hinatsu, pages 58–61. National Maritime Research Institute, Tokyo, Japan.

Noh, W. F. and Woodward, P. R. (1976). SLIC (simple line interface method). In *Lecture Notes in Physics*, edited by A. I. van de Vooren and P. J. Zandenberg, page 330. Springer-Verlag, Berlin/New York.

Ochi, M. K. (1964). Extreme behavior of a ship in rough seas. *Annual meeting of the Society of Naval Architects and Marine Engineers*, pages 143–202.

O'Dea, J. F. and Walden, D. A. (1984). The effect of bow shape and nonlinearities on the prediction of large amplitude motions and deck wetness. In *Proceedings of the 15th Symposium on Naval Hydrodynamics*, pages 163–176. National Academic Press.

Ogawa, Y., Taguchi, H. and Ishida, S. (1998). A Prediction Method for the Shipping Water Heights and its Load on Deck. *Practical Design of Ships and Mobile Units (PRADS)*.

Osher, S. and Sethian, J. A. (1988). Fronts propagating with curvature-dependent speed: algorithms based on Hamiltonian-Jacobi formulations. *Journal of Computational Physics*, vol. 79: pages 12–49.

Repetto, R. A. (2001). *Computation of turbulent free-surface flows around ships and floating bodies*. Ph.D. thesis, Technical University of Hamburg-Harburg.

Rienecker, M. M. and Fenton, J. D. (1981). A Fourier approximation for steady water waves. *J. Fluid. Mech*, vol. 104: pages 119–137.

Rudman, M. (1997). Volume-Tracking Methods for Interfacial Flow Calculations. *Int. Journal for Numerical Methods in Fluid Dynamics*, vol. 24: pages 671–691.

Salvesen, N., Tuck, E. O. and Faltinsen, O. (1970). Ship Motions and Sea Loads. In *Trans SNAME*, vol. 28, pages 250–287.

Sørensen, L. S., Mayer, S., Garapon, A. and Kawamura, T. (1997). A curvilinear multiblock solver for the unsteady incompressible Navier-Stokes equations. Tech. rep., International Research Center for Computational Hydrodynamics, Denmark.

Stansberg, C. T. and Karlsen, S. I. (2001). Green sea and water impact on FPSO in steep random waves. In *Practical Design of Ships and Other Floating Structures (PRADS 2001)*, edited by Y.-S. Wu, W.-C. Cui and G.-J. Zhou, pages 593–601. Shanghai, China.

Sterndorff, M. J. (2002). Large-scale model tests with wave loadings on offshore platform deck elements. In *Proceedings of the International Conference on Offshore Mechanics and Arctic Engineering - OMAE*. ASME.

Stoker, J. J. (1957). Water Waves. In *Pure and Applied Mathematics*, edited by R. Courant, L. Bers and J. J. Stoker. Interscience, New York.

Tan, S. G. (1969). Observations made on board dutch merchant ships. *International Shipbuilding Progress*, vol. 16 (181): pages 259–276.

Ubbink, O. (1997). *Numerical prediction of two fluid systems with sharp interfaces*. Ph.D. thesis, University of London.

Versteeg, H. K. and Malalasekera, W. (1995). *An introduction to computational fluid dynamics: The finite volume method*. Longman.

Wan, D. C. and Wu, G. X. (1999). The numerical simulation of the green water effect. In *Proceedings 14th International Workshop on Water Waves and Floating Bodies*, edited by R. F. Beck and W. W. Schultz, pages 163–176. National Academic Press.

Zang, Y., Street, R. L. and Koseff, J. R. (1994). A non-staggered grid, fractional step method for the time incompressible Navier-Stokes equations in curvilinear coordinates. *Journal of Computational Physics*, vol. 114: pages 18–33.

Zhou, Z. Q., de Kat, J. O. and Buchner, B. (1999). A Nonlienar 3-D Approach to Simulate Green Water Dynamics on Deck. In *7th International Conference on Numerical Ship Hydrodynamics*. Nantes.

Appendix A

Generation of Nonlinear Waves in the Computational Domain

For many applications in the present work the ability to generate waves in the computational domain is of great importance. If incoming or initial experimental wave kinematics is not correctly reproduced in the computations, it cannot be expected that the numerical results will show agreement with experimental results. This appendix will give a brief introduction to higher order wave theory, and illustrate the correspondance between numerically generated wave kinematics and the analytical wave kinematics.

A.1 Stream Function Theory

A solution to the steady water wave problem by use of a Fourier expansion was first presented by Rienecker and Fenton (1981). This method in based on the solution to the Laplace equation for irrotational flow, with boundary conditions given as an inpermable bottom condition, and also a kinematic and a dynamic free surface boundary condition imposing zero flux through the free surface and constant pressure at the free surface, respectively. The solution is labeled the stream function, and the derivatives are the velocity components in the x and y directions, respectively. The stream function is given by the following Fourier series

$$\phi(x,y) = B_0 y + \sum_{j=1}^{N} B_j \frac{\sinh jky}{\cosh jkD} \cos jkx, \tag{A.1}$$

where $B_{1\cdots N}$ are constants for a given wave, k is the wave number and D is an arbitrary reference level in the water. For a solution method and a computer algorithm to solve the equations necessary to determine the Fourier compenents see Fenton (1988). Next, the application of the stream function theory solution to wave generation in the computational domain is described.

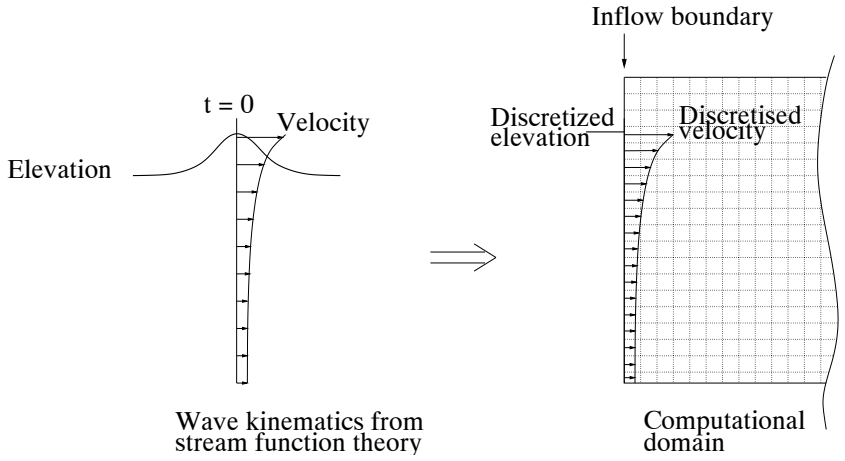

Figure A.1: *Principal sketch showing wave generation in the computational domain.*

A.2 Overview of Wave Generation in the Computational Domain

When all the Fourier components determining the wave kinematics have been computed, the time history of the wave elevation and velocity can be established. From this, the discretised values of elevation and velocity used for generating waves at the boundary of the computational domain can be imposed by extracting the values at the discrete locations. This is illustrated in Fig. A.1. Further, a 'driving' layer can be imposed inside the computational domain, where the stream function solution is added in the cells near the wave generation boundary. This solution is added to the right hand side of the momentum equation as a forcing term, ensuring a solution in the computations identical to the stream function solution.

A.3 Test of Numerical Wave Generation

When generating waves from an initially calm free surface the imposed velocities needs to be ramped from zero to the full values for a specified duration, in order to avoid generating too many disturbances and resonant waves in the flume. This is done by applying the following ramping function

$$R(t) = \frac{t}{t_{\text{ram}}} - \frac{\sin(2\pi \frac{t}{t_{\text{ram}}})}{2\pi} \tag{A.2}$$

where t_{ram} is the ramping period.

Table A.1: *Wave paramenters used for wave generation test*

Wave height	1.28 m
Wave period	5 s
Depth	30 m
Wave length	39.44 m
Wave steepness	0.0325
Length of flume	200 m

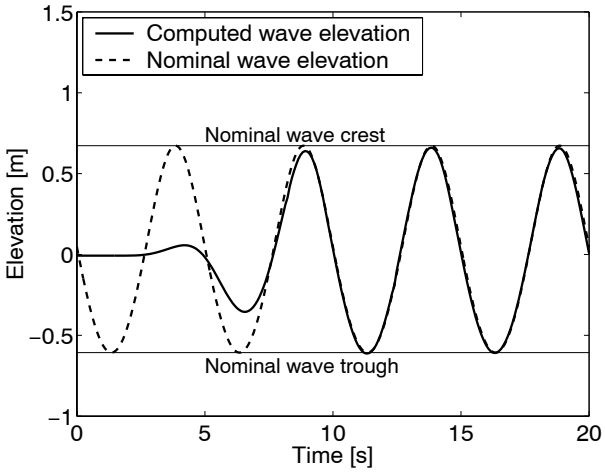

Figure A.2: *Test of wave generation in the computaional domain. Time history of wave elevation at $x = 30$ m. 512×64 grid cells, domain length = 200 m. Nomainal wave profile computed from stream function theory (Fenton, 1988) is also indicated. Ramp time equals 5 s (one period).*

To test the wave generation in the computational domain, a simple, rectangular grid with size of 200×35 m, resolved by 512×64 grid cells, is used. The waves are generated with the wave parameters shown in Table A.3[1] and a ramp time equal to one period is applied. A 'driving' layer is also used to improve wave generation. The resulting wave elevation is shown in Fig. A.2, where the nominal crest and trough values are indicated. The elevation is measured at $x = 30$ m, and the driving layer ends at $x = 10$ m. The figure shows close correspondance between computed and nominal wave elevation.

[1]The wave steepness of 0.0325 indicates that Airy (linear) waves are not valid. The steepness boundary for application of Airy waves is approximately 0.006, in deep water.

Appendix B

Alternative Wave Generation

In the 2-D green water experiments by Greco (2001) the waves in the experimental wave flume were generated by use of a flap type wave generator. These experiments are reproduced in Chapter 7, where the wave generation in the computations uses the method described in Appendix A. However, as a test, the actual wave generator motion used by Greco (2001) are here applied to try to reproduce the experimental wavegenerator, by transforming the wave generator signal info a flux boundary condition in the computational domain.

In Greco (2001) the flap motion was recorded during the experiment and this signal is shown in Fig. B.1. The flap was hinged 0.1 m above the bottom of the flume and by numerical differentiation the flap velocity can be computed computed from the flap translation. In the following, wave generation in the computational domain, by application of the flux boundary condition from the experimental flap motion signal, will be labeled 'alternative wave generation'. In is not expected that the alternative wave generation gives exactly the

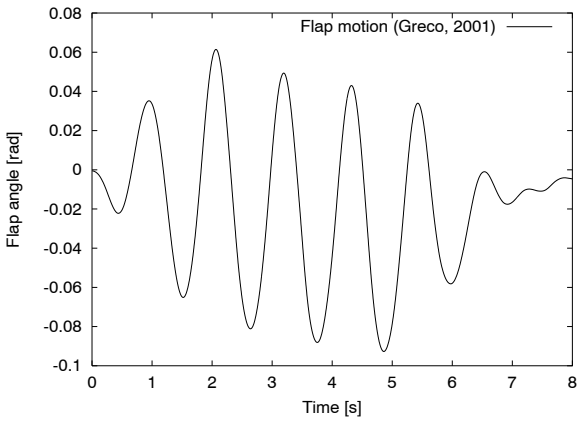

Figure B.1: *Flap motion signal used during 2-D green water experiments by Greco (2001). Resulting wave kinematics: $H = 0.16$ m, $T = 1.1$ s, $\lambda = 2$ m*

same waves as in the experiments, since the full flap motion is not reproduced, but the motion is only 'projected' onto the mean position of the flap. The computations employ the fine grid from Table 7.3.

Details of the location of wave probes are shown in Figs. 7.9 and 7.10. Two probes are located in the wave flume between the wave generator and the FPSO (WP1-WP2), and three probes are located on the FPSO deck (WL1-WL3). In Fig. B.2 the generated wave elevation at WP1 and WP2 are compared between the experiments and computed elevation, where the wave generation in the computations are conducted by the alternative wave generation. The figure shows that the wave crests in the computations are higher than in the experiments, especially at probe WP1, but otherwise the elevations corresponds well. Compared to the computations with the standard wave generation (Fig. 7.16) the agreement in Fig. B.2 in not as satisfactory.

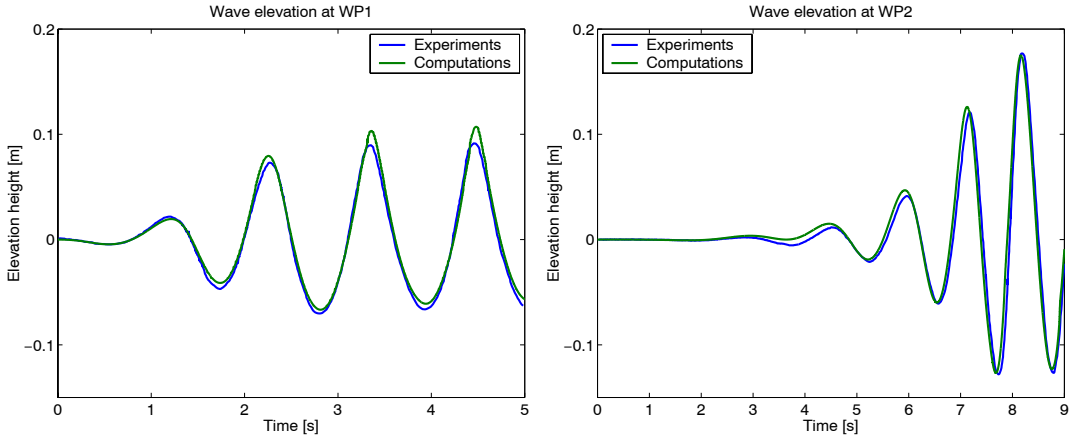

Figure B.2: *Comparison of experimental and computed wave elevation at probes WP1 (left) and WP2 (right). The computed waves are generated by transforming the flap motion recorded during experiments to a flux boundary condition in the coputational domain (alternative wave generation). $H = 0.16$ m, $T = 1.1$ s, $\lambda = 2$ m.*

The resulting water height on deck, measured at the probes WL1-WL3 are in Fig. B.3 compared between experiments and computations. The computed water height for the first wave encounter at probe WL1 is slightly higher in the computations, but the general agreement for all probes is good. The agreement between computed and experimental results is not as exact as with the standard wave generation (Fig. 7.17), but is still considered satisfactory.

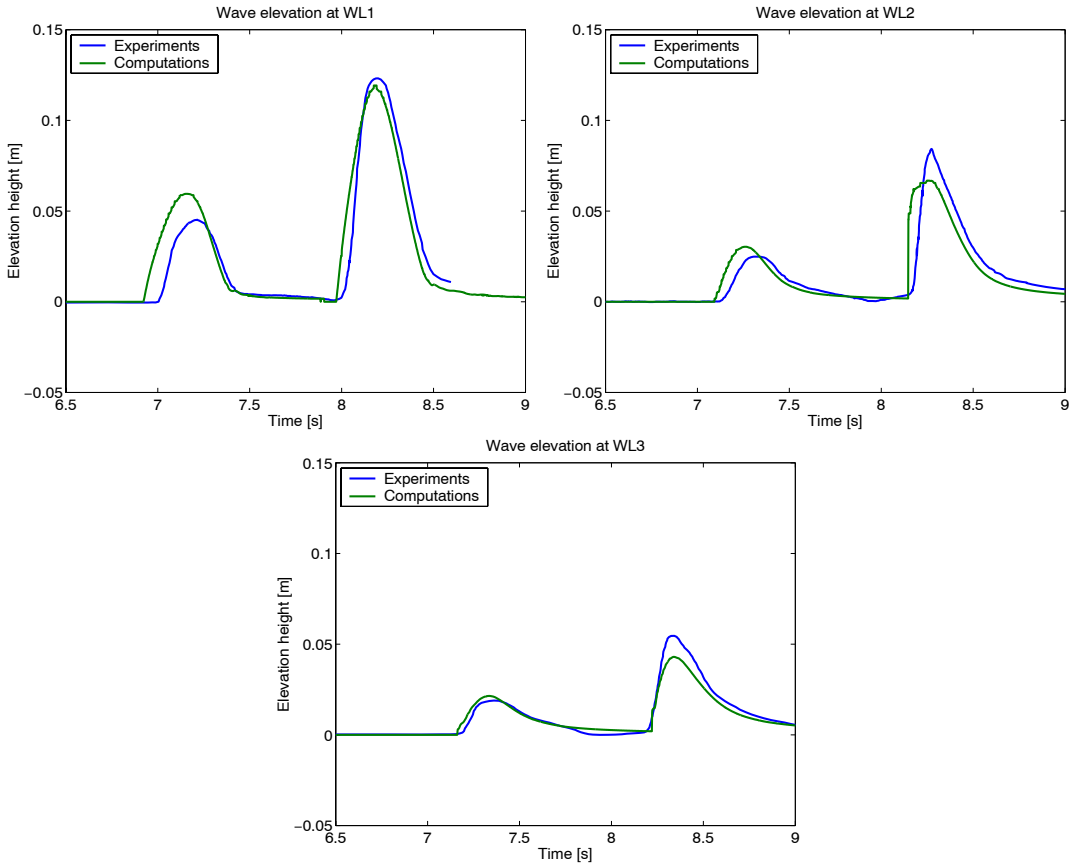

Figure B.3: *Comparison of experimental and computed wave height on deck of the FPSO at probes WL1 (top left), WL2 (top right) and WL3 (bottom). The computed waves are generated by use of the alternative wave generation.*

PhD Theses
Department of Naval Architecture and Offshore Engineering
Technical University of Denmark · Kgs. Lyngby

1961 Strøm-Tejsen, J.
Damage Stability Calculations on the Computer DASK.

1963 Silovic, V.
A Five Hole Spherical Pilot Tube for three Dimensional Wake Measurements.

1964 Chomchuenchit, V.
Determination of the Weight Distribution of Ship Models.

1965 Chislett, M.S.
A Planar Motion Mechanism.

1965 Nicordhanon, P.
A Phase Changer in the HyA Planar Motion Mechanism and Calculation of Phase Angle.

1966 Jensen, B.
Anvendelse af statistiske metoder til kontrol af forskellige eksisterende tilnærmelsesformler og udarbejdelse af nye til bestemmelse af skibes tonnage og stabilitet.

1968 Aage, C.
Eksperimentel og beregningsmæssig bestemmelse af vindkræfter på skibe.

1972 Prytz, K.
Datamatorienterede studier af planende bådes fremdrivningsforhold.

1977 Hee, J.M.
Store sideportes indflydelse på langskibs styrke.

1977 Madsen, N.F.
Vibrations in Ships.

1978 Andersen, P.
Bølgeinducerede bevægelser og belastninger for skib på lægt vand.

1978 Römeling, J.U.
Buling af afstivede pladepaneler.

1978 Sørensen, H.H.
Sammenkobling af rotations-symmetriske og generelle tre-dimensionale konstruktioner i elementmetode-beregninger.

1980 Fabian, O.
Elastic-Plastic Collapse of Long Tubes under Combined Bending and Pressure Load.

1980 Petersen, M.J.
Ship Collisions.

1981 Gong, J.
A Rational Approach to Automatic Design of Ship Sections.

1982 Nielsen, K.
Bølgeenergimaskiner.

1984 Nielsen, N.J.R.
Structural Optimization of Ship Structures.

1984 Liebst, J.
Torsion of Container Ships.

1985 Gjersøe-Fog, N.
Mathematical Definition of Ship Hull Surfaces using B-splines.

1985 Jensen, P.S.
Stationære skibsbølger.

1986 Nedergaard, H.
Collapse of Offshore Platforms.

1986 Yan, J.-Q.
3-D Analysis of Pipelines during Laying.

1987 Holt-Madsen, A.
A Quadratic Theory for the Fatigue Life Estimation of Offshore Structures.

1989 Andersen, S.V.
Numerical Treatment of the Design-Analysis Problem of Ship Propellers using Vortex Lattice Methods.

1989 Rasmussen, J.
Structural Design of Sandwich Structures.

1990 Baatrup, J.
Structural Analysis of Marine Structures.

1990 Wedel-Heinen, J.
Vibration Analysis of Imperfect Elements in Marine Structures.

1991 Almlund, J.
Life Cycle Model for Offshore Installations for Use in Prospect Evaluation.

1991 Back-Pedersen, A.
Analysis of Slender Marine Structures.

1992 Bendiksen, E.
Hull Girder Collapse.

1992 Petersen, J.B.
Non-Linear Strip Theories for Ship Response in Waves.

1992 Schalck, S.
Ship Design Using B-spline Patches.

1993 Kierkegaard, H.
Ship Collisions with Icebergs.

1994 Pedersen, B.
A Free-Surface Analysis of a Two-Dimensional Moving Surface-Piercing Body.

1994 Hansen, P.F.
Reliability Analysis of a Midship Section.

1994 Michelsen, J.
A Free-Form Geometric Modelling Approach with Ship Design Applications.

1995 Hansen, A.M.
Reliability Methods for the Longitudinal Strength of Ships.

1995 Branner, K.
Capacity and Lifetime of Foam Core Sandwich Structures.

1995 Schack, C.
Skrogudvikling af hurtiggående færger med henblik på sødygtighed og lav modstand.

1997 Simonsen, B.C.
Mechanics of Ship Grounding.

1997 Olesen, N.A.
Turbulent Flow past Ship Hulls.

1997 Riber, H.J.
Response Analysis of Dynamically Loaded Composite Panels.

1998 Andersen, M.R.
Fatigue Crack Initiation and Growth in Ship Structures.

1998 Nielsen, L.P.
Structural Capacity of the Hull Girder.

1999 Zhang, S.
The Mechanics of Ship Collisions.

1999 Birk-Sørensen, M.
Simulation of Welding Distortions of Ship Sections.

1999 Jensen, K.
Analysis and Documentation of Ancient Ships.

2000 Wang, Z.
Hydroelastic Analysis of High-Speed Ships.

2000 Petersen, T.
Wave Load Prediction—a Design Tool.

2000 Banke, L.
Flexible Pipe End Fitting.

2000 Simonsen, C.D.
Rudder, Propeller and Hull Interaction by RANS.

2000 Clausen, H.B.
Plate Forming by Line Heating.

2000 Krishnaswamy, P.
Flow Modelling for Partially Cavitating Hydrofoils.

2000 Andersen, L.F.
Residual Stresses and Deformations in Steel Structures.

2000 Friis-Hansen, A.
Bayesian Networks as a Decision Support Tool in Marine Applications.

PhD Theses
Maritime Engineering · Department of Mechanical Engineering
Technical University of Denmark · Kgs. Lyngby

2001 Lützen, M.
Ship Collision Damage.

2001 Olsen, A.S.
Optimisation of Propellers Using the Vortex-Lattice Method.

2002 Rüdinger, F.
Modelling and Estimation of Damping in Non-linear Random Vibration.

2002 Bredmose, H.
Deterministic Modelling of Water Waves in the Frequency Domain.

2003 Urban, J.
Crushing and Fracture of Lightweight Structures.

2003 Lazarov, B.S.
Slepian Simulations of Plastic Displacement of Randomly Excited Hysteretic Structures.

2003 Ravn, E.S.
Probabilistic Damage Stability of Ro-Ro Ships.

2003 Törnqvist, R.
Design of Crashworthy Ship Structures.

2003 Nielsen, K.B.
Numerical Prediction of Green Water Loads on Ships.

Maritime Engineering

Department of Mechanical Engineering

Technical University of Denmark

Studentertorvet, Building 101E
DK-2800 Kgs. Lyngby
Denmark
Phone + 45 4525 1360
Fax + 45 4588 4325
info.mt@mek.dtu.dk
www.mek.dtu.dk

ISBN 87-89502-76-0